CANTILEVER-BASED MEASUREMENTS ON NANOMAGNETS AND SUPERCONDUCTORS

A DISSERTATION
SUBMITTED TO THE DEPARTMENT OF APPLIED PHYSICS
AND THE COMMITTEE ON GRADUATE STUDIES
OF STANFORD UNIVERSITY
IN PARTIAL FULFILLMENT OF THE REQUIREMENTS
FOR THE DEGREE OF
DOCTOR OF PHILOSOPHY

Eric Straver
August 2004

I certify that I have read this dissertation and that, in my opinion, it is fully adequate in scope and quality as a dissertation for the degree of Doctor of Philosophy.

Kathryn A. Moler, Principal Adviser

I certify that I have read this dissertation and that, in my opinion, it is fully adequate in scope and quality as a dissertation for the degree of Doctor of Philosophy.

Malcolm R. Beasley

I certify that I have read this dissertation and that, in my opinion, it is fully adequate in scope and quality as a dissertation for the degree of Doctor of Philosophy.

Daniel Rugar

Approved for the University Committee on Graduate Studies.

This page intentionally left blank.

Abstract

Nanomagnetism and superconductivity are two current areas of interesting research, both for fundamental and technological reasons. In this work, I have used microfabricated cantilevers for cantilever magnetometry measurements of cobalt nanoparticles, and also for magnetic force microscopy studies of vortices in niobium and YBCO.

Since the invention of the atomic force microscope in 1986, cantilevers have become a powerful and popular sensor for studying a wide variety of materials and properties. Cantilever-based magnetic imaging (magnetic force microscopy) was first demonstrated in 1987, and today is a common characterization technique for materials at room temperature. Low temperature imaging systems with a focus on magnetism remain rare however. For this work, I have constructed a low temperature cantilever measurement system, capable of making sensitive cantilever magnetometry measurements, and used in particular for magnetic force microscopy. The instrument uses a fiber optic interferometer as the deflection sensor, and operates using the frequency modulation method. Force gradients as low as 10^{-7} N/m can be measured by detecting the frequency shift of a cantilever.

Nanomagnets are of great interest because of their potential applications in such areas as ultra-high density information storage media, spin electronics, and magnetic sensors. Chemically synthesized monodisperse cobalt nanocrystals with diameters on the order of 10 nm offer a potentially excellent material for such applications. I have characterized their magnetic properties by measuring the low temperature hysteresis loops of small numbers (~1000's) of Co nanocrystals using the technique of cantilever magnetometry, with a moment sensitivity of 10^6 μ_B.

Magnetic force microscopy (MFM) is a powerful technique for manipulating vortices and for characterizing vortex pinning. The microscope I have constructed is capable of imaging vortices with high spatial resolution, and also of directly manipulating them and characterizing the pinning strength. I present magnetic force gradient images of vortices in Nb and YBCO thin films at various temperatures, magnetic fields, and scan heights. I have also demonstrated the ability to directly manipulate individual vortices with the

MFM cantilever. By pulling the vortices with an attractive magnetic force, I have positioned them to construct the initials “SU”, for Stanford University. This is the first demonstration of such control over vortex position using any technique, and has the potential to enable a number of future experiments on the behavior of vortices. For example, I have examined vortex pinning in Nb and YBCO, and have studied the distribution of pinning strengths. The pinning of vortices allows transport currents to flow without dissipation, and thus plays an important role in superconductors for applications.

Acknowledgements

I have many people that I would like to thank for their help in completing this work. First, I would like to thank my adviser, Prof. Kathryn Moler. Kam has been a great person to work with, having many ideas, a lot of enthusiasm, and a great perspective on things. She gave me a lot of independence and had a lot of trust in me, and I learned a lot with this freedom. She also put a lot of time into reading this thesis and made many good suggestions for improvement, which I appreciate. I've enjoyed being a part of her lab.

I would also like to thank the other members of my reading committee, Prof. Mac Beasley and Dr. Dan Rugar, for their interest in my work and for all of their help and feedback. I would particularly like to thank Dan for all of the help he has given me in learning about cantilever measurements and in building my microscope. I spent about six months as a visitor in Dan's lab at the end of my third year at Stanford, and learned an incredible amount from him in that time. And, as if that wasn't enough, at the end of my stay at IBM he shared his microscope design with me (on which I based mine), and continued to provide very helpful advice and answers throughout the following years. This work would not have been possible without Dan's help.

The administrative staff in both Applied Physics and GLAM has also been very helpful over the years, and I would like to thank them. In particular, Judy Clark, Paula Perron, Droni Chiu, Carol Han, Cyndi Mata, and Mark Gibson all did a lot for me. I would also like to thank the machine shop staff, in particular Karlheinz Merkle and John Kirk. The machining for my microscope was done entirely in the Varian machine shop, so I relied heavily on them. Karlheinz was always very helpful with design issues and got me out of trouble on many occasions (e.g. when the coarse approach screw seized a few days before a March Meeting for which I didn't yet have data). John was virtually my personal machinist for a few months when we started building the microscope. I really enjoyed working with him, and had a lot of fun talking about the latest news in the world of cycling whenever I stopped by the shop too.

I was also very fortunate to have really great labmates in the Moler lab, I'm very thankful for their help and friendship. Janice Guikema, Brian Gardner, Per Björnsson and I all joined the lab in our first year, it was a great group of people to be friends and colleagues with. I would particularly like to thank Per for all of his selfless assistance with the many computer issues I had, and for his help in printing and handing in this thesis for me after I had moved back to Canada. I would also like to thank Hendrik Blühm, Clifford Hicks, Nick Koshnick, Zhifeng Deng, Mark Topinka, Rafael Dinner, and all of the summer and rotation students and the visitors I've worked with for their help and friendship. Also, I would like to thank Jenny Hoffman for her help and our many interesting discussions. We did not overlap in the lab for very long, but I enjoyed working with her during that time. Jenny has taken over the MFM from me, I hope that it serves her well.

I would also like to acknowledge some of the other great colleagues I interacted with. I would like to thank Kevin Yasumura and John Chiaverini for their help in my early years at Stanford, they got me started with cantilever measurements and helped a lot with the magnetometry measurements I did for my first project. I have also enjoyed collaborating with Erhan Yenilmez and Sylvia Smullin on cantilever work of various sorts. I would also like to thank the members of the DGG, KGB, Marcus, and Kenny labs, we were fortunate to have great neighbors in the McCullough basement.

I had the good fortune to have terrific friends at Stanford, they all helped make my years there a lot of fun. I've mentioned many of them already, and I would also like to mention here Myles Steiner, Moe Badi, Josh Folk, Silvia Lüscher, and Sara Cronenwett. I had a lot of fun spending time with everyone, I have many great memories from our many camping trips, bike rides, and other adventures. I sincerely hope our adventures don't stop here.

I also would like to thank my family for all of their love and support during my time at Stanford, and of course for their support and guidance in getting me there with the skills and values to succeed. My wife's family has also been great to me, they have always shown a lot of interest in my work and I really appreciate their support.

Finally, I would like to thank my wonderful wife, Trista. We met just over four years ago now on a fateful Stanford Canadian Club camping trip in Yosemite, and as they say, the rest is history. She has experienced the grad school rollercoaster with me, celebrating the highs with me and helping me through the lows. Her love and support and incredible belief in me helped me get to this point, and I'm very grateful to have her in my life.

This work was supported by an AFOSR Presidential Early Career Award, the National Science Foundation (grant DMR-0103548), and a Packard Fellowship. I would also like to thank the National Science and Engineering Research Council of Canada for helping to support me financially for two of my years at Stanford.

This page intentionally left blank.

Contents

List of Tables

List of Figures

List of Variables

A	rms cantilever vibration amplitude
A	scan area
A_o	amplitude at resonance
α	angle between magnetic moment and anisotropy axis
$B, \vec{B}$	magnetic field
B_a	anisotropy field
$B_{applied}$	applied magnetic field
B_{vortex}	magnetic field from a vortex
BW	bandwidth
$c_i, i = V_x, V_{x^2}, V_y, V_{y^2}, 1$	coefficients describing sample surface location
C_{magnet}	magnet calibration coefficient in liquid nitrogen
$cal_i, i = x, y, z$	scan calibration coefficient
d	fiber-cantilever separation
δ	phase shift between force and cantilever response
δf	frequency noise
δf_{det}	frequency detector noise
δf_{th}	thermal cantilever frequency noise
δf_{int}	frequency noise due to the interferometer
δV_{int}	interferometer noise
δV_{li}	laser intensity noise
δV_{lp}	laser phase noise

δV_J	Johnson noise
δV_{sh}	shot noise
ΔA	amplitude change
Δd	change in fiber-cantilever separation
$\Delta\lambda$	laser wavelength change
$\Delta\omega$, Δf	cantilever resonant frequency shift
ΔP	change in power
$\Delta\psi$	cantilever vibration angle (for magnetometry)
ΔV	interferometer voltage change
E	energy
E_a	anisotropy energy
E_c	cantilever phase energy
E_{ds}	deflection sensor phase noise energy
E_i	incident light energy
E_m	magnetic energy
η	photodetector efficiency
F	force
$F_{ex}\left[t\right]$	excitation force
F_{meas}	the measured component of the force in MFM
F'	force gradient, perpendicular to the cantilever surface
F'_{meas}	the measured component of the force gradient
$F'_{\min}$	minimum detectable force gradient
F_r	radial force
$F_{ts}\left[z\right]$	tip-sample force
γ	damping coefficient

I_{total}	total current through the magnet and persistent current switch during operation in liquid nitrogen
k	cantilever spring constant
k_B	Boltzmann's constant, 1.38 x 10^{-23} J/K
k_{eff}	effective spring constant
$K_i, i = 0,1,2,...$	anisotropy constants
k_m	change in spring constant due to magnetic interactions
κ_n	wave number for n^{th} vibration mode
L	tip length
l	cantilever length
$l_{eff} = l/1.38$	effective cantilever length
λ	penetration depth of a superconductor
λ	laser wavelength
m	cantilever mass
$m, \vec{m}$	magnetic moment
$m_{\min}$	minimum detectable magnetic moment
M_s	saturation magnetization
$\vec{M}^{tip}$	magnetization of the MFM tip
M_z	magnetic moment per unit length (monopole tip)
$\hat{n}$	unit vector normal to cantilever surface
$n_{\Delta f}$	frequency noise density
$n_{\Delta x}$	deflection sensor noise density
n_{fiber}	optical fiber index of refraction
n_i	noise density

$n_{i_{initial}}$	initial number of vortices in the ith measurement
$n_{i_{moved}}$	number of depinned vortices in the ith measurement
$n_{initial}$	initial number of vortices from all scans
n_{moved}	total number of vortices that depinned
n_{vacuum}	vacuum index of refraction
N_{vortex}	number of vortices
ω, f	excitation frequency
ω_o, f_o	cantilever resonant frequency
ω_o', f_o'	cantilever resonant frequency in the presence of a force gradient
ω_m	the frequency at which the slope of $dA/d\omega$ is a maximum
ω_{mod}, f_{mod}	modulation frequency
P	optical power
P_{depin}	depinning probability
P_i	incident optical power
P_o	average power
P_{min}	minimum reflected power
P_{max}	maximum reflected power
Φ_o	flux quantum, 20.7 Gμm^2
ψ	magnetic field polar angle, , as described by Equation (2.17) for magnetometry setup
Q	quality factor
R	resistance of inteferometer photodetector resistor

R_{magnet}	fraction of total current in the magnet during operation in liquid nitrogen
$\vec{r}$	cantilever tip position
r_c	cantilever reflection coefficient
R_c	power reflection coefficient for the cantilever
r_f	fiber reflection coefficient
R_f	power reflection coefficient for the optical fiber
ρ	mass density
$\sigma_{P_{depin}}$	uncertainty in the depinning probability
t	cantilever thickness
t	time
T	temperature
t_f	fiber transmission coefficient
ϕ	magnetic moment polar angle, as described by Equation (2.17) for magnetometry setup
ϕ_o	easy axis polar angle, as described by Equation (2.17) for magnetometry setup
ϕ_{eq}	equilibrium magnetic moment polar angle
θ	optical path difference in the interferometer
θ	magnetic moment azimuthal angle, as described by Equation (2.17) for magnetometry setup
θ_o	easy axis azimuthal angle, as described by Equation (2.17) for magnetometry setup
θ_{eq}	equilibrium magnetic moment azimuthal angle
v	visibility
V	interferometer voltage

V	volume
V_o	average interferometer voltage
V_{tip}	volume of the magnetic tip of an MFM cantilever
V_x	piezotube x voltage
V_y	piezotube y voltage
V_z	piezotube z voltage
w	cantilever width
x	cantilever x position
y	cantilever y position
Y	Young's modulus
z	cantilever deflection
z_o	equilibrium cantilever deflection
ζ	magnetic field azimuthal angle, as described by Equation (2.17) for magnetometry setup

Chapter 1 : Introduction

Since the invention of the atomic force microscope in 1986 (Binnig et al. 1986), cantilevers have become a powerful and popular sensor for studying a wide variety of materials and properties. Cantilever-based magnetic imaging (magnetic force microscopy) was first demonstrated in 1987 (Martin and Wickramasinghe 1987), and today is a common characterization technique for materials at room temperature. Low temperature imaging systems with a focus on magnetism remain rare however. Such imaging systems are powerful tools for characterizing materials. The Moler Lab at Stanford University has thus far focused on low temperature magnetic imaging, using Hall Probes and Squids to image superconductors (Guikema 2004). For this thesis, I have constructed a low temperature cantilever measurement system, capable of making sensitive cantilever magnetometry measurements, and used in particular for magnetic force microscopy. I have used it to manipulate vortices in Nb and to study vortex pinning in a Nb and a YBCO thin film. Additionally, I have studied cobalt nanomagnets using the technique of cantilever magnetometry.

The structure of this thesis is as follows. Broadly speaking, this thesis covers three topics. Namely, I discuss cantilever measurements and instrumentation, cantilever magnetometry measurements of cobalt nanomagnets, and magnetic force microscope measurements of vortices in superconductors. Chapter 2 introduces the basic principles of cantilever measurements with a particular focus on the frequency modulation detection method. It also covers the principles behind the two cantilever-based techniques used in this thesis, cantilever magnetometry and magnetic force microscopy, and outlines the noise sources which affect the sensitivity of the two techniques. In Chapter 3, I discuss the design and operation of the low temperature magnetic force microscope I constructed as part of this work, including the sensitivity of the instrument in the context of frequency modulation measurements of force gradients. Chapter 4 is a step back to the first project I worked on at Stanford, as I discuss the cantilever magnetometry measurements I carried out on cobalt nanomagnets. This work began with the intention of characterizing the nanomagnets for future use as the magnetic tips of magnetic force microscope cantilevers. Although the project was unsuccessful in creating new MFM tips, the nanomagnet measurements provide a good demonstration of the potential power of the magnetometry technique.

Chapter 5 through Chapter 7 covers the work I have done using the MFM I constructed to study vortices in superconductors. In Chapter 5, I discuss my initial results imaging vortices in a Nb thin film. I present a variety of images of vortices at different magnetic fields, temperatures, and scan heights, and also present some modeling and fitting of vortex images. In Chapter 6, I discuss the manipulation of individual vortices in a Nb film, which is the first ever demonstration of such control over vortex position. Based on this manipulation capability, I also have developed a procedure to characterize depinning of vortices, and present results of measurements I carried out on the Nb film using this procedure. In Chapter 7, I present images of vortices in a YBCO thin film, including a discussion of some difficulties of running the microscope using liquid nitrogen as opposed to liquid helium. I also present some preliminary measurements of vortex depinning in the film, and conclude with some comments about how those measurements might be completed and improved upon.

Finally, the Appendix of this thesis contains a user manual for the MFM I constructed. It is not meant to be a completely thorough, commercial-ready manual, but I think that there are some useful tricks that can be learned from it. I have included it here to ensure that future users will have an easy place to find some information which will hopefully help them get started with running my microscope.

Chapter 2 : Magnetic Measurements using Cantilevers

Cantilever are powerful sensors used for a variety of measurements. Samples can be mounted directly on the cantilever for characterization using a technique such as cantilever magnetometry, or the cantilever can be positioned above a sample as in magnetic force microscopy. Both DC and AC measurement techniques are used. This chapter outlines the basic principles behind cantilever measurements, and behind two specific techniques, cantilever magnetometry and magnetic force microscopy.

2.1 Basic Principles of Cantilever Measurements

2.1.1 Force Measurements

Force is the most basic quantity that a cantilever can directly measure. The cantilever acts like a spring and responds to a force F according to Hooke's law:

$$x = \frac{F}{k} \tag{2.1}$$

where k is the spring constant of the cantilever, and x is the deflection of the end of the lever. By measuring the cantilever deflection one can measure the force on the cantilever, which can then be related to properties of the sample under study. This is a broadly applicable measurement technique, and is used to measure atomic, electrostatic, or in the case of this thesis, magnetic forces.

Force measurements are made in a frequency range of DC to a low pass cutoff frequency dictated by the measurement setup. In this range, the sensitivity of a measurement is limited by deflection sensor noise. Low temperature magnetic force microscopes use either cantilevers with a fiber optic interferometer as the deflection sensor, or piezoresistive cantilevers where the deflection sensor is integrated into the lever itself. Piezoresistive cantilevers are not common, and are available with a limited range of spring constants between 1 and 10 N/m. The sensitivity of a piezoresistive cantilever has been measured to be 0.1 Å in a 10 Hz to 1 kHz bandwidth (Tortonese 1993), corresponding to a force sensitivity of 0.3 pN/Hz$^{1/2}$ for a 1 N/m cantilever.

Commercially available cantilevers have spring constants ranging between 0.01 to 200 N/m. With a typical value for the white noise level of a fiber optic interferometer of 0.005 Å/Hz$^{1/2}$ (Albrecht et al. 1992), the force sensitivity can be as low as 0.005 pN/Hz$^{1/2}$. However, near DC there is likely to be additional 1/f noise (particularly in the case of piezoresistive detection) and 60 Hz line noise, and it is necessary to integrate the noise spectrum over the measurement frequency range to determine the actual force sensitivity.

2.1.2 Force Gradient Measurements

Cantilevers can also be used to measure force gradients. A cantilever driven by a sinusoidal force $F_{ex}[t]$ follows the equation of motion for a damped harmonic oscillator:

$$m\frac{d^2z}{dt^2}+\gamma\frac{dz}{dt}+k(z-z_o)=F_{ex}[t]+F_{ts}[z] \tag{2.2}$$

where m is the mass of the cantilever, γ is the damping coefficient, and z_o is the cantilever position in the absence of a force. $F_{ts}[z]$ is the force between the cantilever and the sample under study at a cantilever deflection z. The force must be integrated over the total cantilever volume, but the force is likely to vary a lot over that volume. In general the force on a small region at the cantilever tip dominates the signal. A Taylor expansion of the force gives:

$$m\frac{d^2z}{dt^2}+\gamma\frac{dz}{dt}+k(z-z_o)=F_{ex}[t]+F_{ts}[z=z_o]+\left.\frac{dF_{ts}}{dz}\right|_{z=z_o}(z-z_o) \tag{2.3}$$

An effective spring constant k_{eff} can be defined:

$$\begin{gathered}m\frac{d^2z}{dt^2}+\gamma\frac{dz}{dt}+\left(k-\left.\frac{dF_{ts}}{dz}\right|_{z=z_o}\right)(z-z_o)=F_{ex}[t]+F_{ts}[z=z_o]\\ m\frac{d^2z}{dt^2}+\gamma\frac{dz}{dt}+k_{eff}(z-z_o)=F_{ex}[t]+F_{ts}[z=z_o]\end{gathered} \tag{2.4}$$

where $k_{eff} \equiv k - dF_{ts}/dz$. The cantilever resonant frequency in the presence of a force gradient is given by ω_o':

$$\omega_o' = \sqrt{\frac{k_{eff}}{m}} \tag{2.5}$$

The right hand side of Equation (2.5) can be Taylor expanded for $dF_{ts}/dz \ll k$. The cantilever frequency shift $\Delta\omega = \omega_o' - \omega_o$ is then:

$$\frac{\Delta\omega}{\omega_o} = \frac{-1}{2k}\frac{dF_{ts}}{dz} \tag{2.6}$$

where ω_o is the natural resonant frequency of the cantilever. The force gradient can be then measured using either slope detection (Martin et al. 1987) or frequency modulation detection (Albrecht et al. 1991), as described below.

2.1.3 Slope Detection

The slope detection technique measures force gradients by measuring changes in the cantilever's amplitude and/or phase. The cantilever is driven at a frequency slightly off resonance, and as changes in the force gradient shift the resonant frequency, the cantilever amplitude and phase change. The cantilever amplitude A and phase δ are given by:

$$A = \frac{A_o\left(\omega_o'/\omega\right)}{\sqrt{1 + Q^2\left(\omega/\omega_o' - \omega_o'/\omega\right)^2}} \tag{2.7}$$

$$\tan\delta = \frac{1}{Q}\frac{1}{\omega_o'/\omega - \omega/\omega_o'} \tag{2.8}$$

where A_o is the vibration amplitude when the cantilever is driven at its resonant frequency, Q is the cantilever quality factor, and ω is the frequency of the driving force. The amplitude and phase are illustrated in Figure 2-1.

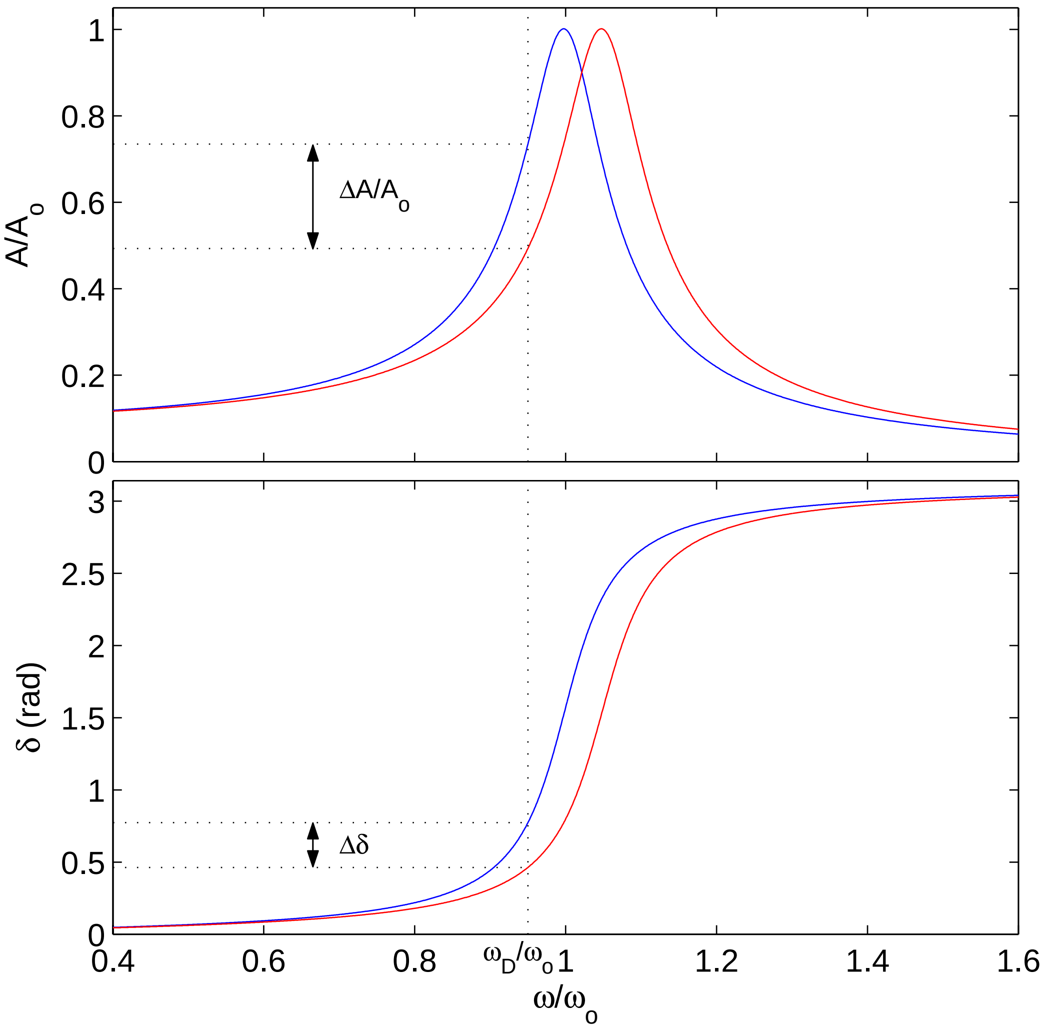

Figure 2-1: The cantilever amplitude A and phase δ as a function of the excitation frequency ω. The blue curve illustrates the response in the absence of a force gradient, and the red curve illustrates the response in the presence of a force gradient which has shifted the resonant peak. In the Slope Detection method, the cantilever is driven at a frequency ω_D which is slightly off resonance. Force gradients are measured by measuring either the amplitude change ΔA or the phase change $\Delta\delta$ as the cantilever resonant frequency shifts due to the gradient.

For amplitude measurements, the most sensitive operating point is at the point of maximum slope $dA/d\omega$, which occurs at $\omega = \omega_o'\left(1 \pm 1/\sqrt{8}Q\right)$. The force gradient is given by (Martin et al. 1987):

$$F' = \frac{3\sqrt{3}k}{2Q}\frac{\Delta A}{A_o} \tag{2.9}$$

In the case of cantilever thermal noise limited amplitude measurements, the minimum detectable force gradient F'_{min} is given by (Martin et al. 1987):

$$F'_{\mathrm{min}} = \frac{1}{A}\sqrt{\frac{27kk_BTBW}{\omega_o Q}} \tag{2.10}$$

where k_B is Boltzmann's constant, T is the cantilever temperature, and BW is the measurement bandwidth. Slope detection is the method used in commercial room temperature non-vacuum magnetic force microscopes, such as that made by Veeco Instruments.

2.1.4 Frequency Modulation

The frequency modulation (FM) technique uses positive feedback to oscillate the cantilever at its resonant frequency, by phase shifting the cantilever vibration signal by 90º and driving the cantilever with the resultant waveform. Figure 2-2 illustrates the cantilever response as a function of the excitation frequency. At resonance, there is a 90º phase shift between the cantilever drive and response, such that if the phase shift is maintained at 90º, the cantilever will be excited at its resonant frequency.

The effects of changes in Q are also eliminated by vibrating the cantilever at exactly 90º phase shift. As shown in Figure 2-3, if the phase shift is maintained at 1 rad, a change in Q results in a frequency change which is indistinguishable from a frequency shift due to a force gradient. At 90º phase shift, changes in Q have no effect on the feedback frequency. Thus the resonant frequency can be measured directly and related to the force gradient by Equation (2.6). Changes in Q result from changes in the energy dissipation in the tip-sample interaction. These changes are in fact measured using a

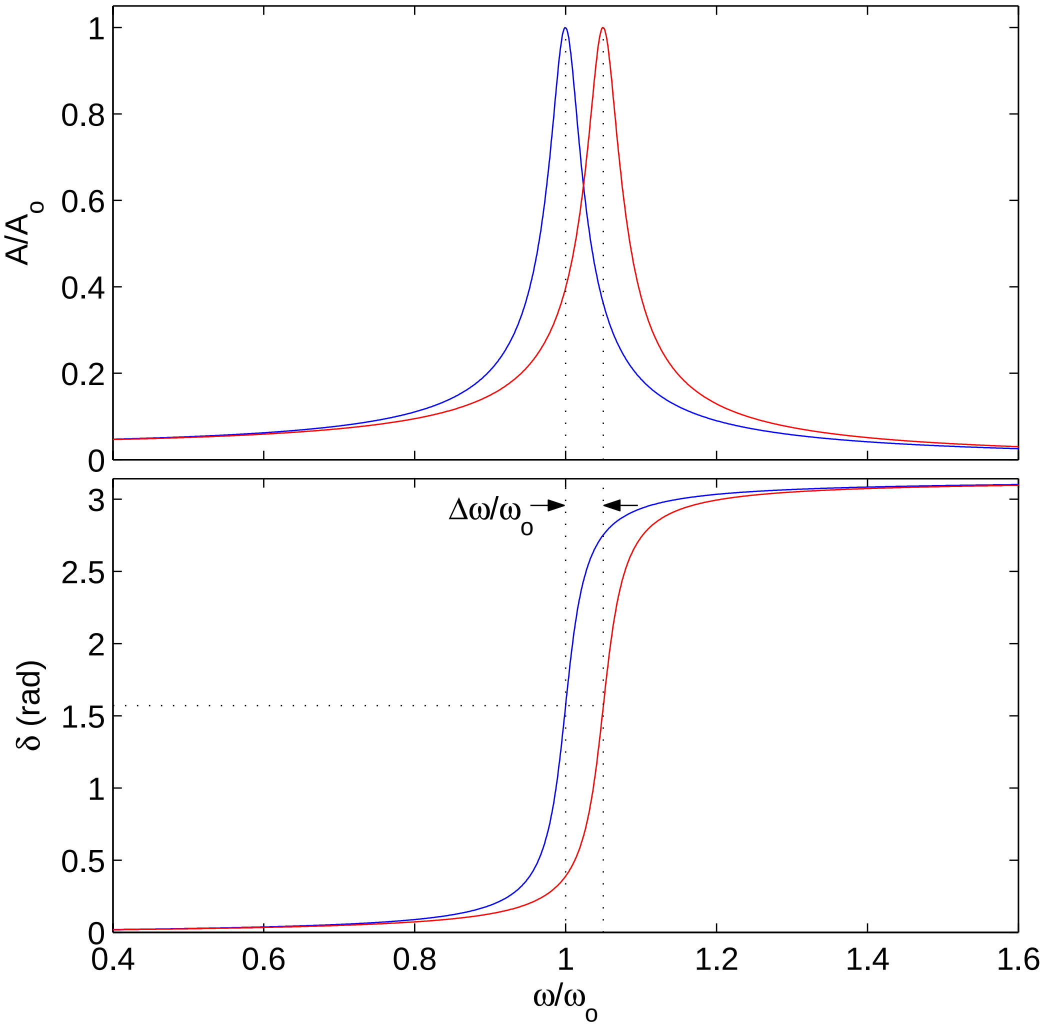

Figure 2-2: The cantilever amplitude A and phase δ as a function of the excitation frequency ω. In the Frequency Modulation Detection method, the phase difference δ between the excitation and the cantilever response is maintained at 90º, such that the cantilever always oscillates at its resonant frequency. Here, the blue curve illustrates the response in the absence of a force gradient, and the red curve illustrates the response in the presence of a force gradient which has shifted the resonant peak. Force gradients are measured by directly measuring the shift in the resonant frequency.

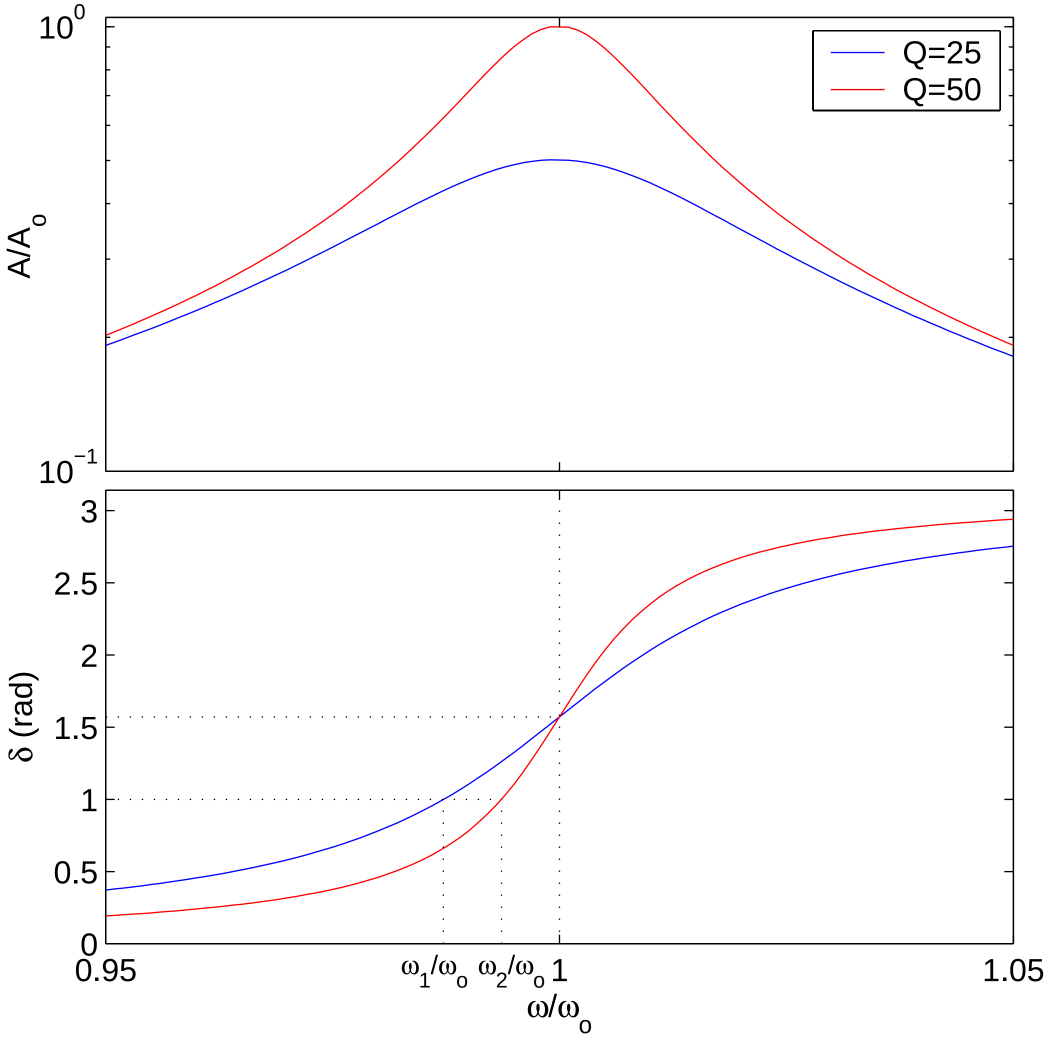

Figure 2-3: The cantilever amplitude A and phase δ as a function of the excitation frequency ω for two different values of Q, in the absence of a force gradient. Changes in the dissipation can lead to errors in the force gradient measurement in the slope detection method. If the cantilever is driven at a frequency ω_1, a change in Q results in a change in A as shown by the difference between the red and blue curves. This is also a problem in the frequency modulation detection method if the phase is not properly set. Above, if the phase is maintained at 1 rad, a change in Q results in a frequency shift from ω_1 to ω_2. The problem is eliminated if the phase is properly set to 90°, because this phase occurs at the resonant frequency for all values of Q.

technique known as dissipation force microscopy. This technique has been explored for applications such as semiconductor dopant mapping (Stowe et al. 1999), by measuring the electrical losses due to induced charge motion, and for studies of magnetic domain walls, by measuring the magnetoelastic and eddy current losses associated with wall jumps (Liu 1997).

The minimum detectable force gradient for thermally limited measurements is (Albrecht et al. 1991):

$$F'_{\min} = \frac{1}{A}\sqrt{\frac{4kk_BTBW}{\omega_o Q}} \tag{2.11}$$

For cantilevers with high quality factors however, noise from the deflection sensor will likely dominate the measurement. In this case, the frequency noise density $n_{\Delta f}$ is given by (Albrecht et al. 1991):

$$\begin{aligned} n_{\Delta f}^2 &= \left(\frac{2E_{ds}}{E_c}\right) f_{\text{mod}}^2 \\ &= \frac{n_{\Delta x}^2}{A^2} f_{\text{mod}}^2 \end{aligned} \tag{2.12}$$

where $E_{ds} = \frac{1}{2}kn_{\Delta x}^2$ is the deflection sensor phase noise energy density, $n_{\Delta x}$ is the cantilever deflection sensor noise density, $E_c = kA^2$ is the cantilever phase energy, and f_{mod} is the modulation frequency. This noise density yields a minimum detectable force gradient of:

$$F'_{\min} = \frac{2k}{\sqrt{3}\omega_o}\frac{n_{\Delta x}}{A}BW^{3/2} \tag{2.13}$$

For measurements using high Q cantilevers, such as measurements conducted in vacuum, FM detection is superior to the slope detection method. This is due to the fact that with slope detection, a high Q restricts the measurement bandwidth (Albrecht et al. 1991). A relatively long time is needed for the cantilever amplitude to settle to its steady-state value, and only small shifts from the resonant peak can be measured. In the case of

FM detection, Q and BW are independent. Q may be increased to improve the sensitivity of the measurement without restricting the measurement bandwidth. FM detection is the method used for all of the measurements presented in this thesis.

2.2 Cantilever Magnetometry

Magnetic properties of a sample can be characterized using the technique of cantilever magnetometry. In this technique, the sample is mounted directly on a cantilever, and the assembly is placed in a magnetic field. In a DC measurement, the cantilever deflection is measured to determine the torque that the magnetic field exerts on the magnetic sample (Lupien et al. 1999). In an alternating gradient magnetometer (AGM) measurement (Todorovic and Schultz 1998), an AC field is applied and the resultant cantilever vibration amplitude is measured. Magnetometry measurements can also be made by measuring the resonant frequency of a vibrating structure. A torsional pendulum has been used in this way (Zijlstra 1961; Gradmann et al. 1976; Elmers and Gradmann 1990). Here, I consider only the case of a cantilever vibrating in a static magnetic field (Harris 2000; Stipe et al. 2001). The frequency shift is given by Equation (2.6). The effective spring constant $k_{eff} = k + k_m$, where k_m is the change to the spring constant due to magnetic interactions:

$$k_m = \frac{d^2 E_m}{dz^2} \tag{2.14}$$

where E_m is the magnetic energy given by:

$$E_m = E_a - \vec{m} \cdot \vec{B} \tag{2.15}$$

$\vec{m}$ is the magnetic moment of the sample under study, $\vec{B}$ is the magnetic field, and E_a is the anisotropy energy. For a sample with uniaxial anisotropy, the anisotropy energy is (Cullity 1972):

$$E_a = V\left[K_o + K_1 \sin^2(\alpha) + K_2 \sin^4(\alpha) + \ldots\right] \tag{2.16}$$

where V is the sample volume, K_i are anisotropy coefficients, and α is the angle between the magnetic moment and the anisotropy axis. Attaching a coordinate system to the tip of the cantilever as illustrated in Figure 2-4, the three relevant vectors are given by:

$$\begin{aligned}\vec{\mathrm{B}} &= \mathrm{B}\left(\sin\varsigma\cos\psi,\cos\varsigma\cos\psi,\sin\psi\right)\\ \vec{m} &= m\left(\sin\theta\cos\phi,\cos\theta\cos\phi,\sin\phi\right)\\ \hat{c} &= \left(\sin\theta_o\cos\phi_o,\cos\theta_o\cos\phi_o,\sin\phi_o\right)\end{aligned} \tag{2.17}$$

ζ, θ_o and ϕ_o are constants for each particular measurement setup. In order to determine k_m, E_m must first be minimized to find the equilibrium values of θ and ϕ (θ_{eq} and ϕ_{eq}) for a given ψ. Then:

$$k_m = \frac{\partial^2 E_m}{\partial\psi^2}\left(\frac{d\psi}{dz}\right)^2 + \frac{\partial E_m}{\partial\psi}\frac{d^2\psi}{dz^2}\bigg|_{\theta=\theta_{eq};\phi=\phi_{eq}} \tag{2.18}$$

In order to make the problem solvable analytically, the case of $\vec{B}$ and $\hat{c}$ aligned along the length of the cantilever ($\phi_o=\theta_o=\varsigma=0$; ψ, θ and $\phi \ll 1$), with a single domain magnetic particle at the cantilever tip, is considered here. For this situation ψ is equivalent to the cantilever deflection angle, which can be determined from vibrating beam theory. The shape of a vibrating beam is given by (Sarid 1991):

$$\begin{gathered}z(y,t) = z(y)\cos(\omega t)\\ z(y) = \frac{A}{2}\left[\left(\cos\kappa_n y - \cosh\kappa_n y\right) - \frac{\cos\kappa_n l + \cosh\kappa_n l}{\sin\kappa_n l + \sinh\kappa_n l}\left(\sin\kappa_n y - \sinh\kappa_n y\right)\right]\end{gathered} \tag{2.19}$$

where z and y are the displacement and position along the length of the cantilever respectively, l is the length of the cantilever, and κ_n is the wave number for the n$^{\text{th}}$ vibration mode. For the fundamental mode, $\kappa = 1.875/l$, such that:

$$\psi = \frac{d^2 z}{dy^2}\bigg|_{y=l} = \frac{-1.38z(l)}{l} \tag{2.20}$$

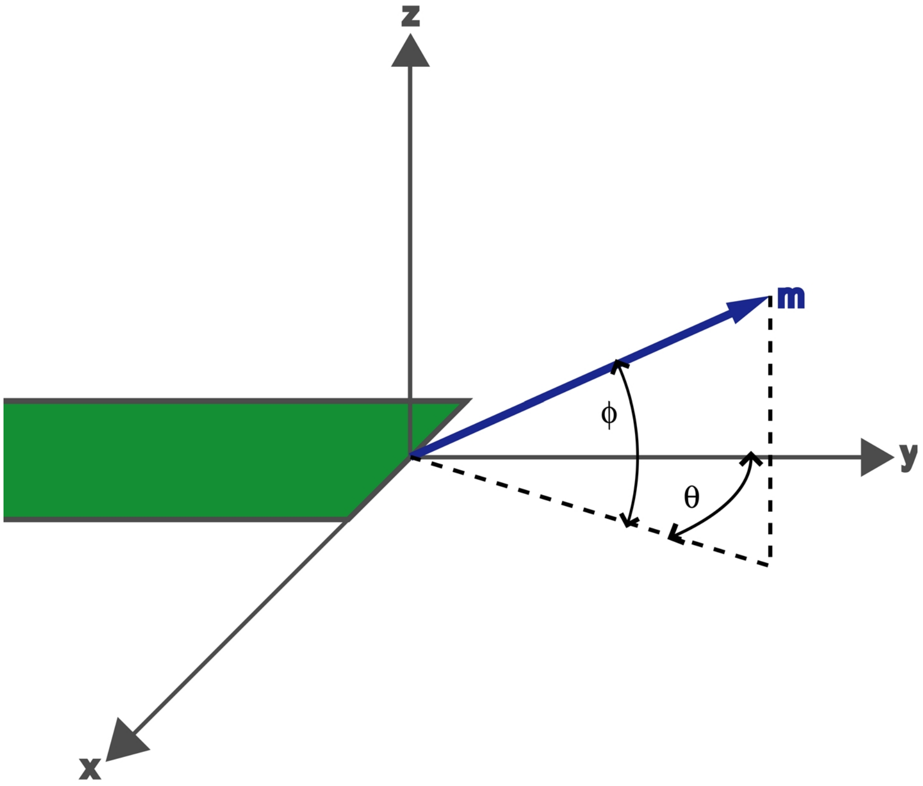

Figure 2-4: The coordinate system attached to the end of the cantilever (shown in green) to describe the magnetometry setup. ϕ is the angle between the magnetic moment and the x-y plane, and θ is the angle between the y-axis and the projection of $\vec{m}$ in the x-y plane. The magnetic field and easy axis vectors are described similarly as in Equation (2.17), but are not shown here for figure clarity.

Defining an effective cantilever length $l_{eff} = l/1.38$ and differentiating:

$$\begin{aligned} \frac{d\psi}{dz} &= \frac{-1}{l_{eff}} \\ \frac{d^2\psi}{dz^2} &= 0 \end{aligned} \tag{2.21}$$

The change to the effective spring constant is then:

$$k_m = \frac{mB}{l_{eff}^2} \frac{1}{1 + B/B_a} \tag{2.22}$$

where $B_a \equiv 2K_1/M_s$ is the anisotropy field, and M_s is the saturation magnetization. Using Equations (2.5) and (2.22), and considering the limit of $B/B_a \ll 1$, the frequency shift is:

$$\Delta\omega = \omega_o \frac{mB}{2kl_{eff}^2} \tag{2.23}$$

For measurements limited by cantilever thermal noise, the minimum measurable magnetic moment is determined comparing this with Equation (2.11):

$$m_{\min} = \frac{2}{BA} \sqrt{k_B TBW} \sqrt{\frac{kl_{eff}^4}{\omega_o Q}} \tag{2.24}$$

Note here that B is the magnetic field, and BW is the bandwidth. For determining which cantilevers are optimal for these measurements, it is instructive to change this equation to reflect cantilever parameters which can be controlled during the fabrication process.

$$m_{\min} = \frac{1}{1.38^2 BA} \sqrt{k_B TBW} \sqrt{\frac{wt^2 l^3}{Q}} \left(Y\rho\right)^{1/4} \tag{2.25}$$

w is the cantilever width, t is the cantilever thickness, l is the actual cantilever length, and Y and ρ are the Young's modulus and mass density of the cantilever. The ideal cantilevers for sensitive magnetic moment measurements are thin, narrow, and short, with high quality factors.

2.2.1 Modeling

For field and easy axis orientations other than the simplest arrangement described by Equation (2.22), the magnetometry measurement must be modeled numerically (Harris 2000). The procedure for the numerical analysis is as follows. To start, select an orientation for the magnetic field and easy axis, i.e. choose values for the constant terms ζ, ϕ_o, and θ_o in Equation (2.17). Next, minimize the energy to determine the direction of $\vec{m}$ (find ϕ and θ) for each of three values of ψ, where $\Delta\psi$ is small. Calculate the energy for each situation, and numerically differentiate the energies to determine two torque values. Finally, determine the magnetic spring constant by numerically differentiating the torque.

The numerical model was initially evaluated for the simple situation described by Equation (2.22). The results are shown in Figure 2-5. The numerical model obtains the same result as the analytical model, and is also capable of modeling hysteresis in an ideal single-domain magnetic particle.

In a real measurement, it should be possible to obtain good alignment between the cantilever and the magnetic field, however it is likely that the orientation of the sample easy axis will not be particularly controllable. It is instructive then to study the dependence of the magnetometry results on the orientation of the easy axis. The numerical model was used to study the magnetometry signal for different values of the angles ϕ_o, and θ_o, with the field aligned along the length of the cantilever, $\vec{B} = (0, \cos\psi, \sin\psi)$. The results are shown for various ϕ_o in Figure 2-6, and for several values of θ_o in Figure 2-7. Knowledge of this dependence could also be a powerful tool if one can control the angle between the easy axis (via the cantilever, assuming the easy axis direction is fixed with respect to the cantilever) and field, as would be the case in a measurement setup with a rotation stage, or with a 3-axis superconducting magnet.

2.3 Magnetic Force Microscopy

Magnetic force microscopy (Martin and Wickramasinghe 1987) is an imaging technique based on atomic force microscopy (Binnig et al. 1986), in which magnetic forces or force gradients are measured to image the magnetic structure of a sample. A

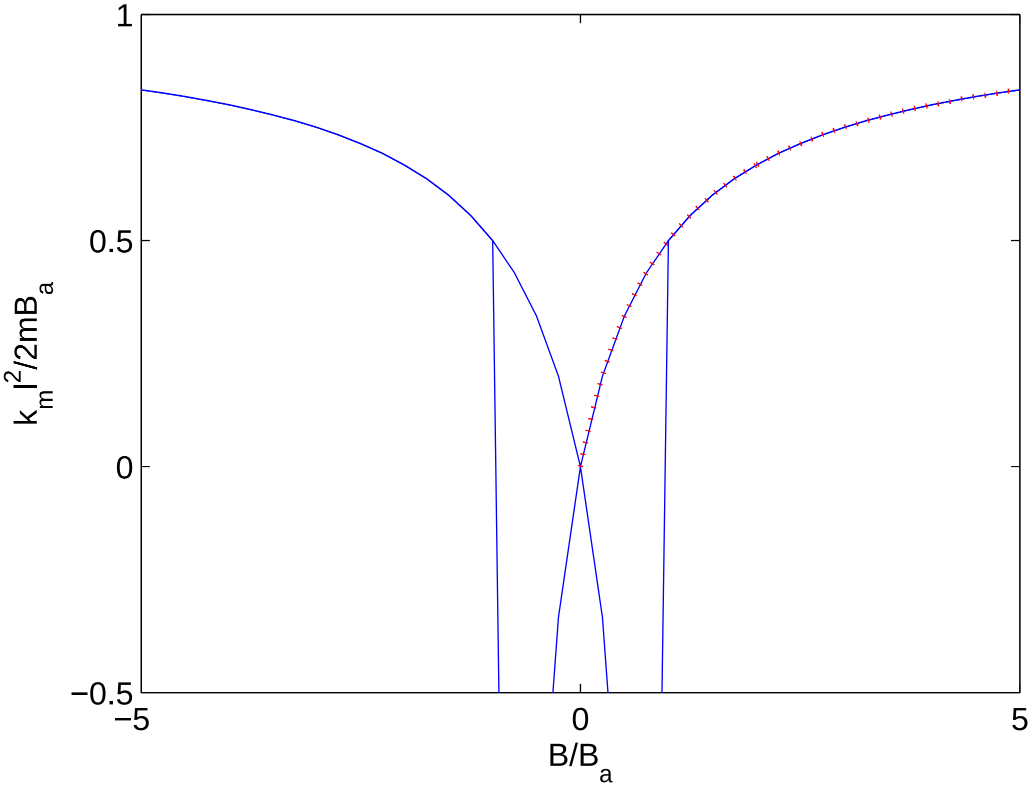

Figure 2-5: The change to the effective spring constant k_m as a function of applied magnetic field B for a cantilever magnetometry measurement of a single domain uniaxial magnet. A numerical model obtains the same result as the analytic model for the case of the magnetic field and easy axis perpendicular to the cantilever bending axis. The results from the numerical model are illustrated by the blue curve, and the analytic model described by Equation (2.22) is shown by the red dotted curve. The numerical analysis can model hysteresis in a single domain magnetic particle.

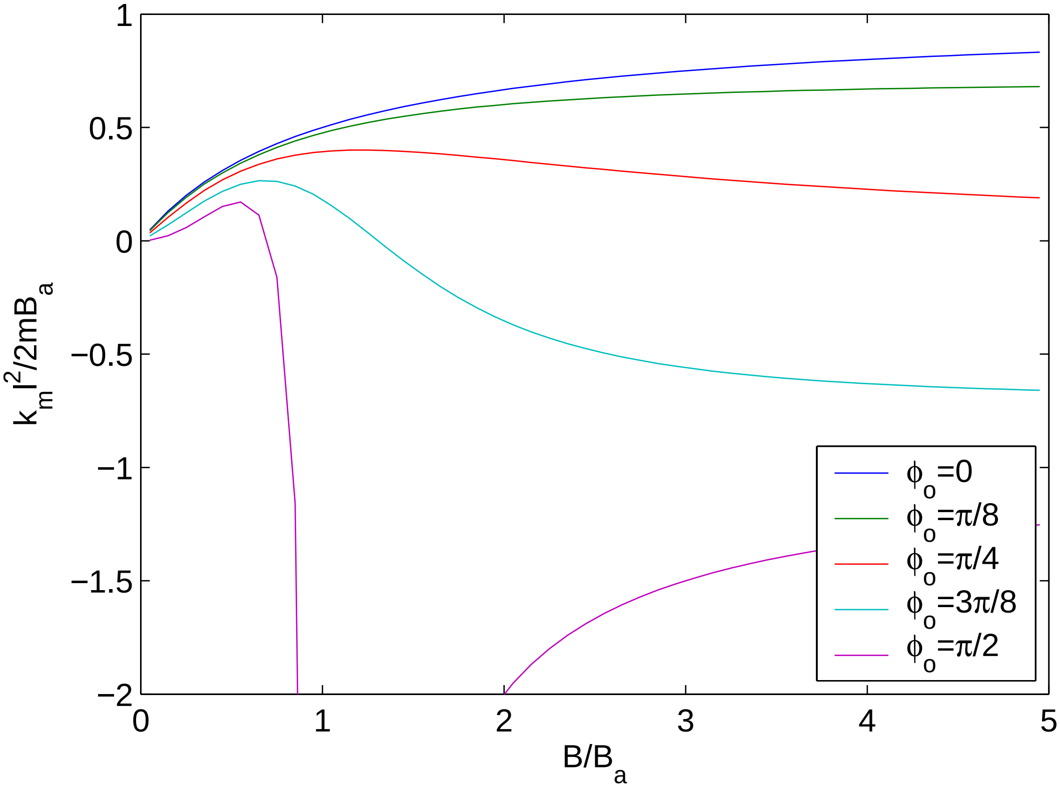

Figure 2-6: The change to the effective spring constant k_m as a function of applied magnetic field B for a cantilever magnetometry measurement of a single domain uniaxial magnet. The cantilever magnetometry signal is modeled here for different values of ϕ_o, the angle between the easy axis and x-y plane, with the field pointing in the $\hat{y}$ direction.

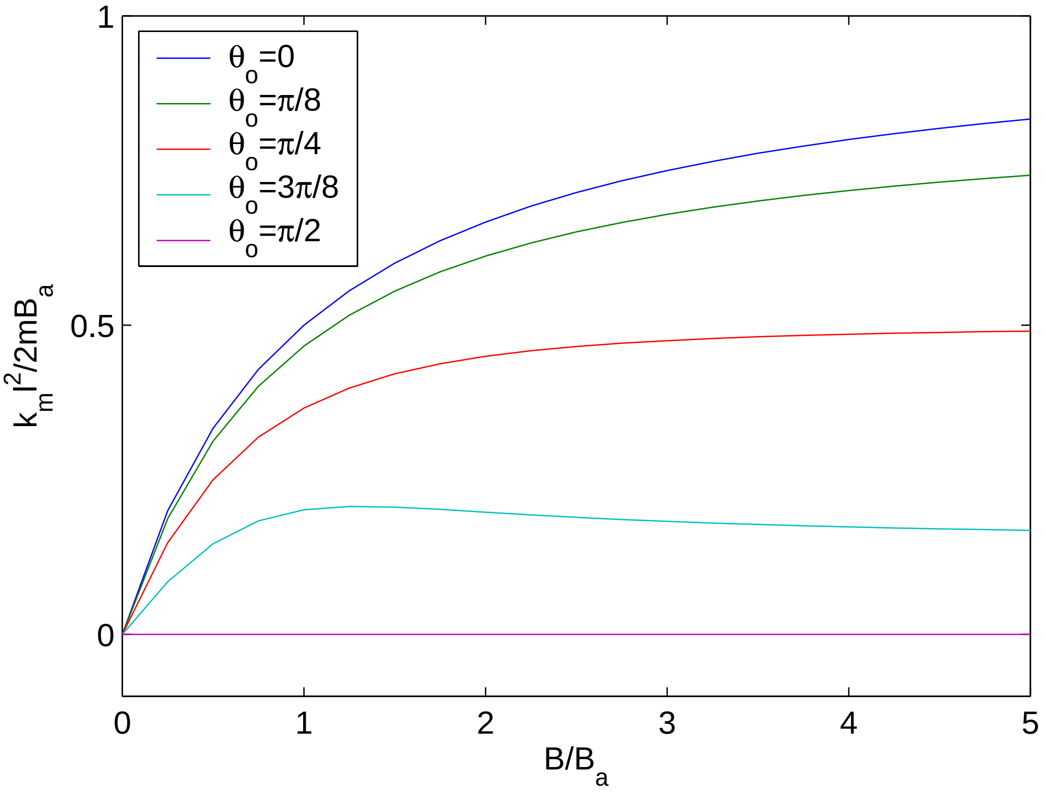

Figure 2-7: The change to the effective spring constant k_m as a function of applied magnetic field B for a cantilever magnetometry measurement of a single domain uniaxial magnet. The cantilever magnetometry signal is modeled here for different values of θ_o, the easy axis angle in the x-y plane. The field is pointing in the $\hat{y}$ direction.

cantilever with a magnetic tip is used to measure the magnetic field from a magnetic sample via the force F_{ts}, given by the gradient of the magnetic energy :

$$\vec{F}_{ts} = \nabla\left(\vec{m}\cdot\vec{B}\right) \tag{2.26}$$

where generally $\vec{m}$ is taken to be the magnetic moment of the cantilever tip and $\vec{B}$ the stray field from the sample (taking $\vec{m}$ as the magnetic moment of the sample and $\vec{B}$ as the stray field from the tip is equally valid, but more complicated). The component actually measured is the component normal to the surface of the cantilever, $F_{meas} = \hat{n}\cdot\vec{F}$, where $\hat{n}$ is a unit vector perpendicular to the cantilever surface. Expanding F_{meas} into its components and integrating the tip magnetization over the tip volume (Grütter et al. 1995):

$$F_{meas} = \int_{tip}\sum_{i=x,y,z}\sum_{j=x,y,z} n_j M_i^{tip}\left(\vec{r}'\right)\frac{\partial B_i\left(\vec{r}+\vec{r}'\right)}{\partial r_j}dV'_{tip} \tag{2.27}$$

where $\vec{M}^{tip}$ is the tip magnetization, $\vec{r}$ is the position of the tip, and the integral is over the volume of the cantilever tip V_{tip}. MFM images can also be obtained by measuring the force gradient:

$$F'_{meas} = \int_{tip}\sum_{i=x,y,z}\sum_{j=x,y,z}\sum_{k=x,y,z} n_j n_k M_i^{tip}\left(\vec{r}'\right)\frac{\partial^2 B_i\left(\vec{r}+\vec{r}'\right)}{\partial r_j\partial r_k}dV'_{tip} \tag{2.28}$$

This can be simplified by considering the case of the cantilever parallel to the sample surface ($\hat{n}=\hat{z}$), and a point dipole tip with moment $\vec{m}$:

$$\begin{aligned} F_{meas} &= F_z = m_x\frac{\partial B_x}{\partial z} + m_y\frac{\partial B_y}{\partial z} + m_z\frac{\partial B_z}{\partial z} \\ F'_{meas} &= \frac{dF_z}{dz} = m_x\frac{\partial^2 B_x}{\partial z^2} + m_y\frac{\partial^2 B_y}{\partial z^2} + m_z\frac{\partial^2 B_z}{\partial z^2} \end{aligned} \tag{2.29}$$

A point dipole can be used to approximate the total moment of a tip as a moment $\vec{m} = \int_{tip}\vec{M}_{tip}dV'_{tip}$ concentrated at one point, and is applicable for small tips (tips with length scales comparable to the length scale of the force or force gradient). A long tip can be described as a monopole. Consider a thin cylindrical tip of length L with a magnetic moment per unit length M . For $L \gg z$, where $z = 0$ is the surface of the superconductor, the force is given by:

$$\begin{aligned} F_z &= \int_{z+L}^{z} M_z \frac{dB_z}{dz'} dz' \\ &= M_z B_z(z) - M_z B_z(z+L) \\ &\cong M_z B_z(z) \end{aligned} \tag{2.30}$$

The contribution from the end of the tip far from the sample is insignificant. Similarly, the force gradient is:

$$\begin{aligned} \frac{dF_z}{dz} &= \int_{z+L}^{z} M_z \frac{d^2 B_z}{dz'^2} dz' \\ &= M_z \frac{dB_z}{dz}(z) - M_z \frac{dB_z}{dz}(z+L) \\ &\cong M_z \frac{dB_z}{dz}(z) \end{aligned} \tag{2.31}$$

2.3.1 Modeling

It is instructive to model the MFM signal for several simple situations. In this section, four scenarios will be examined: a standard horizontal cantilever with a tip moment perpendicular to the sample, a horizontal cantilever with a moment parallel to the sample, and a vertical cantilever with both moment orientations.

One simple model for a sample is a magnetic monopole. Of course, magnetic monopoles do not exist, but any arbitrary magnetization distribution can be described as a sum or integral over a collection of monopoles. In addition, at large length scales ($|\vec{r}| \gg \lambda$, where λ is the penetration depth of the superconductor, $\vec{r} = (x, y, z)$ is the position of the cantilever tip, $z = 0$ is the sample surface, and $x = y = 0$ is the position of the vortex in the x-y plane) a superconducting vortex can be well approximated as a monopole situated a penetration depth below the surface of the superconductor (Pearl 1966):

$$\begin{aligned}\vec{B}_{vortex}\left(\vec{r}\right) &\approx \frac{\Phi_o}{2\pi}\frac{\hat{r}}{r^2}\\ &= \frac{\Phi_o}{2\pi}\frac{x\hat{x}+y\hat{y}+\left(z+\lambda\right)\hat{z}}{\left(x^2+y^2+\left(z+\lambda\right)^2\right)^{3/2}}\end{aligned} \tag{2.32}$$

where $\Phi_o = 20.7 G\mu m^2$ is the superconducting flux quantum. Consider first the situation of a cantilever oriented parallel to the surface ($\hat{n} = \hat{z}$), with a tip moment perpendicular to the surface ($\vec{m} = m\hat{z}$). Inserting Equation (2.32) into Equation (2.29) and simplifying:

$$\begin{aligned}\frac{dF_z}{dz} &= m_z\frac{d^2B_z}{dz^2}\\ &= \frac{3m_z\Phi_o}{2\pi}\frac{\left(z+\lambda\right)\left(-3x^2-3y^2+2\left(z+\lambda\right)^2\right)}{\left(x^2+y^2+\left(z+\lambda\right)^2\right)^{7/2}}\end{aligned} \tag{2.33}$$

This expression includes only the force from the vortex but does not include the force from the Meissner screening currents which screen the magnetic field from the tip from the interior of the superconductor. Similar analysis can be carried out the case of the tip moment oriented parallel to the sample surface, i.e. $\vec{m} = m\hat{x}$, such that $dF_z/dz = m_x \cdot d^2B_x/dz^2$. The case of a cantilever oriented perpendicular to the sample surface ($\hat{n} = \hat{x}$, such that F_x and dF_x/dx can be measured) can also be evaluated, with $dF_x/dx = m_z \cdot d^2B_z/dx^2$ for $\vec{m} = m\hat{z}$, and $dF_x/dx = m_x \cdot d^2B_x/dx^2$ for $\vec{m} = m\hat{x}$. The results are illustrated in Figure 2-8. The spatial variation of the force gradient is measured as a frequency shift (FM detection), amplitude change, or phase change (slope detection) as the cantilever is scanned above the sample surface.

Additionally, the signal can be modeled for the case of a monopole tip:

$$\begin{aligned}\frac{dF_z}{dz} &= M_z\frac{dB_z}{dz}\\ &= \frac{M_z\Phi_o}{2\pi}\frac{\left(-x^2-y^2+2\left(z+\lambda\right)^2\right)}{\left(x^2+y^2+\left(z+\lambda\right)^2\right)^{5/2}}\end{aligned} \tag{2.34}$$

This is illustrated in Figure 2-9. Although it is not measured, the cantilever does exert a radial force F$_r$ on the vortex. For $\hat{n} = \hat{z}$ and $\vec{m} = m\hat{z}$:

$$\begin{aligned} F_r &= m_z \frac{dB_z}{dr} \\ &= \frac{-3m_z\Phi_o}{2\pi}\frac{r^2}{\left(r^2 + \left(z+\lambda\right)^2\right)^{5/2}} \end{aligned} \tag{2.35}$$

where $r = \sqrt{x^2 + y^2}$. The radial force reaches a maximum value at $r = z/\sqrt{2}$. For a dipole tip, the ratio of the maximum radial force to the maximum measured force gradient is:

$$\frac{F_{r_{\max}}}{\left.\frac{dF_z}{dz}\right|_{\max}} = \frac{z}{3\sqrt{3}} \tag{2.36}$$

It is more common in MFM to measure the force gradient than the force, because the signal to noise ratio is higher than it is for force measurements. Consider the force and force gradient between a point dipole tip with $\vec{m} = 10^5 \mu_B \hat{z}$, and a monopole as described by Equation (2.32). At a separation of $\left(z+\lambda\right) = 200nm$, the force on the dipole tip is 76 fN, compared to a noise level of 0.1 pN in a 100 Hz bandwidth as described in Section 2.1.1. The force gradient is 1.1 µN/m, compared to a sensitivity of 0.7 µN/m, as determined using Equation (2.13) and the parameters $k = 3\,N/m$, $f_o = 75kHz$, $A = 10nm$, $n_{\Delta x} = 0.01\,Å/Hz^{1/2}$, and $BW = 100Hz$. The relative signal to noise ratios then are 0.7 and 1.6. Force gradient measurements can also yield improved spatial resolution over force measurements. This is shown in Figure 2-10, which illustrates the z component of the magnetic field and the first two derivatives from a monopole as a function of scan position. The FWHM decreases as the order of the derivative is increased.

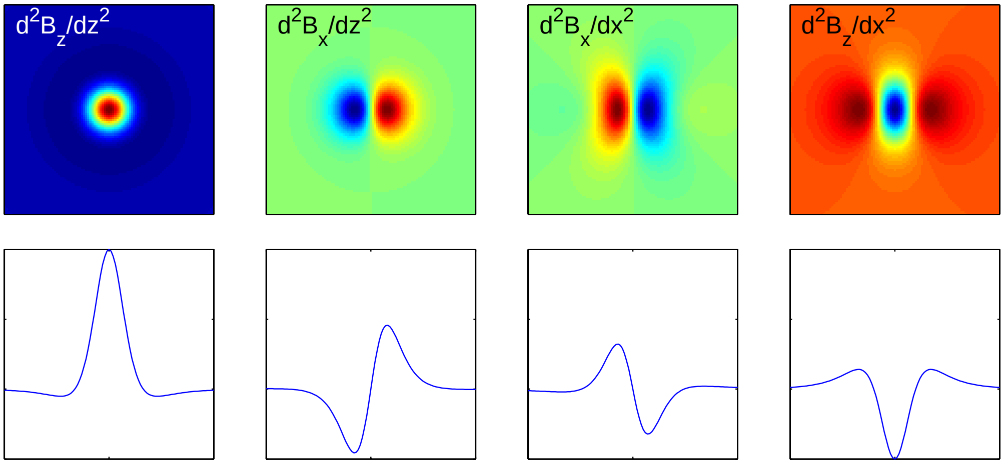

Figure 2-8: Simulated MFM frequency modulation measurements of a vortex showing the shape of the response for different tip moment and cantilever orientations. The vortex can be modeled as a monopole situated a distance λ below the sample surface. Here the magnetic MFM tip is modeled as a point dipole. The line plots show the relative size of the respective signals.

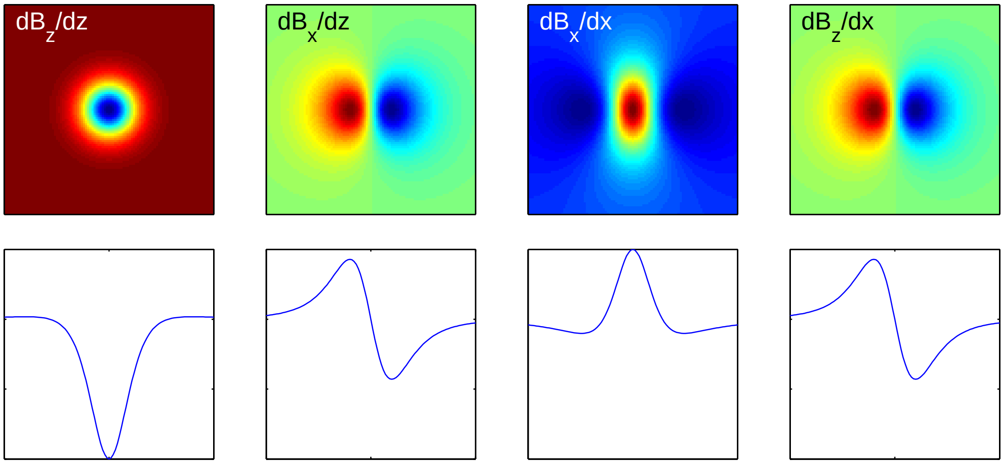

Figure 2-9: Simulated MFM frequency modulation measurements of a vortex showing the shape of the response for different tip moment and cantilever orientations. The vortex can be modeled as a monopole situated a distance λ below the sample surface. Here the magnetic MFM tip is modeled as a monopole. The line plots show the relative size of the respective signals.

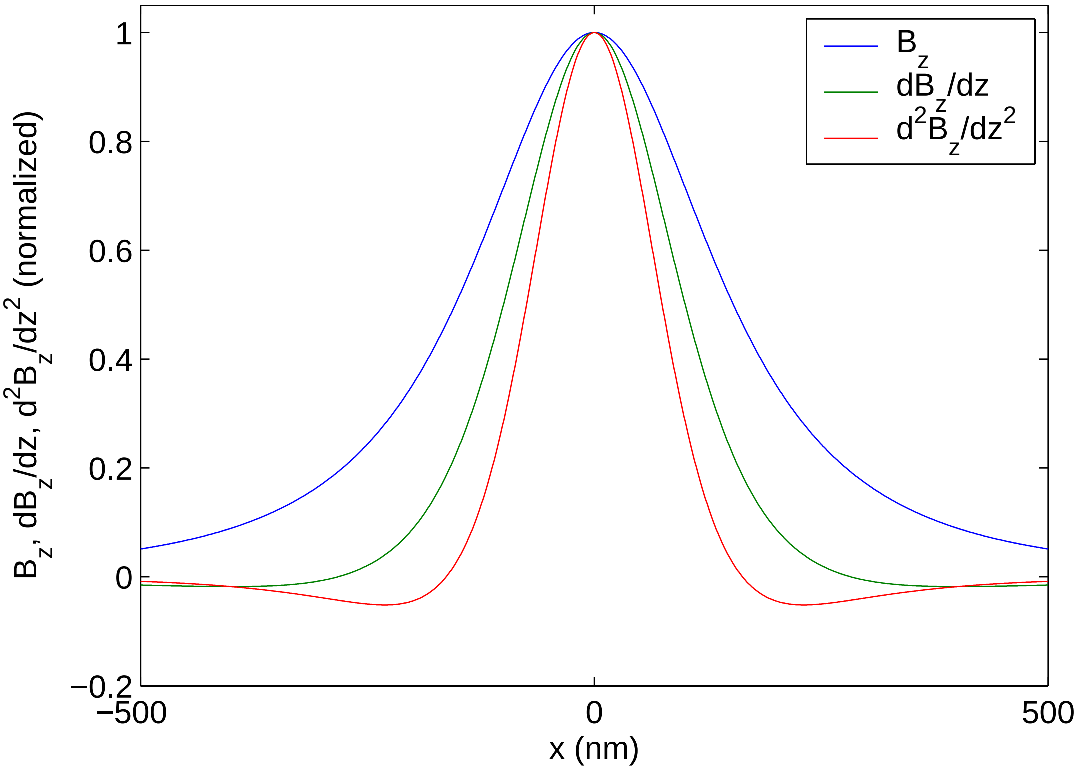

Figure 2-10: The z component of the magnetic field and first two derivatives from a vortex modeled as a monopole situated a distance λ below the sample surface. Here $z = \lambda = 100nm$. The FWHM decreases with increasing order of the derivative. Thus, higher spatial resolution can be obtained by operating using an AC method, which measures B'' (dipole tip) or B' (monopole tip), compared to using a DC method which measures B' (dipole tip) or B (monopole tip). Similarly, a dipole tip can obtain better spatial resolution than a monopole tip.

This page intentionally left blank.

Chapter 3 : Instrumentation

A low temperature magnetic force microscope was constructed for this thesis, based on Dan Rugar's MRFM (magnetic resonance force microscope) design. As with all low temperature scanning microscopes, our MFM is a fairly complicated instrument. It incorporates a high vacuum probe, cryogenics, vibration isolation, a fiber optic sensor, microfabricated cantilevers, a variety of commercial and homemade electronics, and control software. The functional completed instrument is a powerful tool for characterizing materials through high resolution magnetic imaging. This chapter outlines the design of the instrument, and presents some initial demonstrations of its capabilities.

3.1 Instrument Design

The physical structure of the microscope is that of a long metal tube under vacuum, inside of which is the microscope head. The vacuum tube is inserted into a liquid helium dewar with a superconducting magnet for experiments at low temperatures and high magnetic fields. The dewar is supported on an optical table that is mounted on air legs, with the dewar descending below floor level into a concrete pit. The insert can be raised and lowered in and out of the dewar using an electric chain hoist mounted on a uni-strut assembly above the optical table. The hoist can also slide away from the table to allow the microscope insert to be lowered onto a shelf for ease of making adjustments to the microscope. The mechanical structure of the microscope is illustrated in Figure 3-1, and details are outlined in this section.

3.1.1 Vacuum

The vacuum assembly (illustrated in Figure 3-2) essentially consists of the microscope insert and a pair of pumps, a turbopump for pumping the insert down to high vacuum levels, and a scroll pump for rough-pumping the system and for backing the turbopump. The insert is a long metal tube consisting of four separate sections. The four sections are joined using indium wire seals, which was chosen because of its suitability for use at low temperatures (as opposed to vacuum seals using polymer rings, like kwik-flange seals),

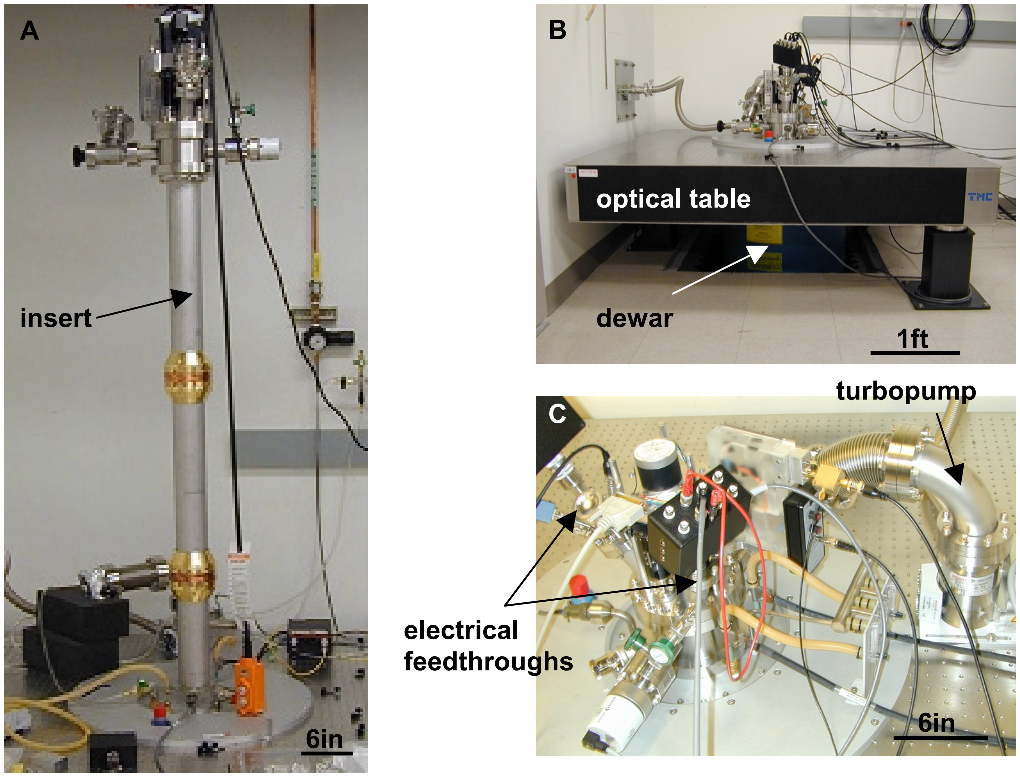

Figure 3-1: The mechanical structure of the microscope. The microscope consists of (A) a high vacuum insert which is inserted in (B) a liquid helium dewar mounted on an optical table. (C) The vacuum space is pumped out using a turbopump. A variety of feedthroughs connect the interferometer, coarse approach mechanism, and electronics between the vacuum space and the laboratory.

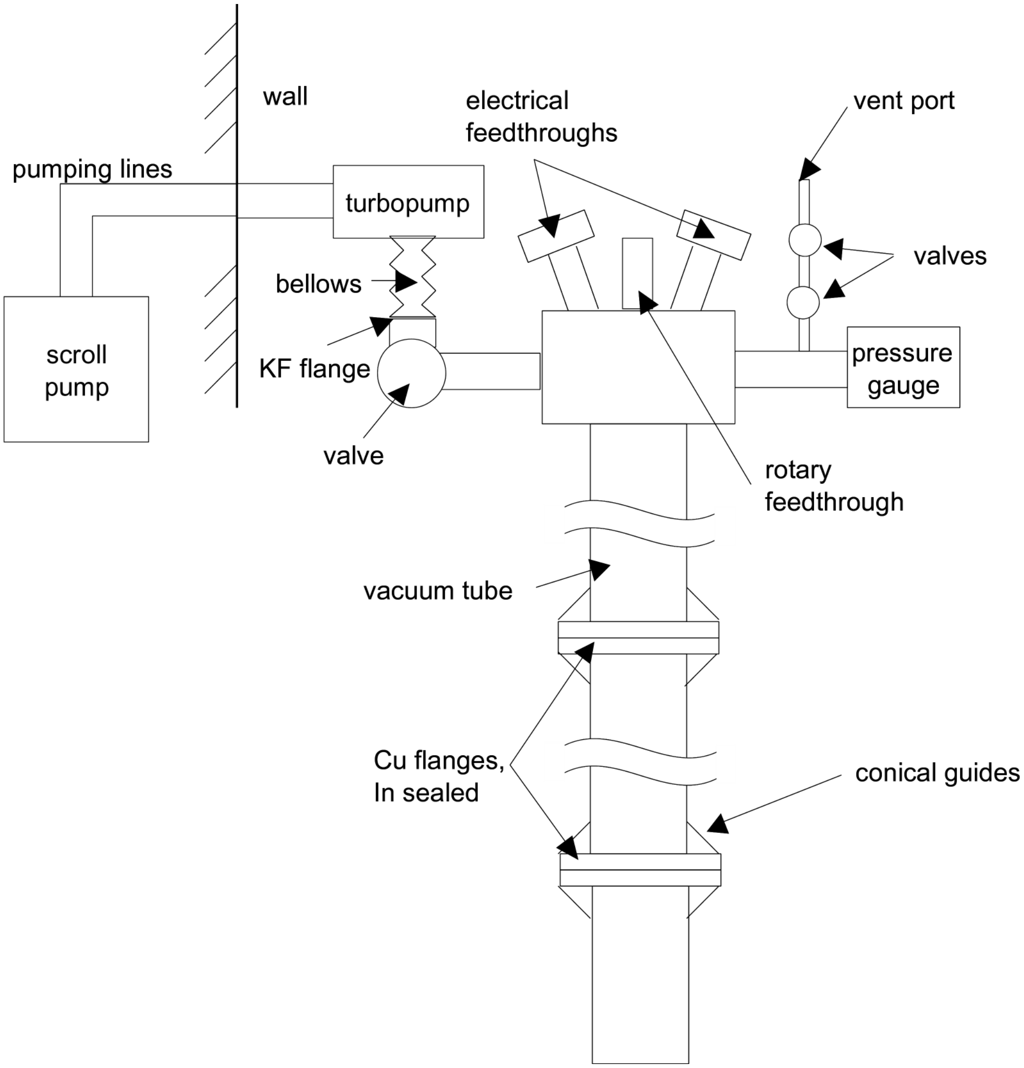

Figure 3-2: The vacuum system of the magnetic force microscope (not to scale). Indium seals are used to join copper flanges to seal the vacuum tube. A turbopump and scroll pump are used to create the vacuum, and a cold cathode gauge is used to measure the pressure. Various feedthroughs at the top of the microscope allow for the introduction of wires, an optical fiber, and various mechanical connections inside the vacuum.

and because of the flexibility in design, particularly with regards to size (as opposed to using conflat seals, which are only available in certain diameters). The vacuum tube is 5 feet long and 3.5 inches in diameter. The relatively large diameter (for a cryogenic insert) yields a rigid insert which helps to reduce the effect of vibrations, and also gives a large space for the microscope head, allowing great flexibility in the head design. The thin wall thickness minimizes the heat leak into the helium bath. Gold-plated copper cones are mounted on either side of the indium seal flanges to guide the insert through the dewar neck baffles, and to provide additional thermal mass and thermal contact to the cryogens.

At the top of the insert are a variety of feedthroughs necessary for running the microscope. The vacuum seals for the feedthroughs are all made using conflat flanges, as the size constraints are not the same issue outside of the dewar. The feedthroughs include electrical connections, mechanical feedthroughs, and one arm of the fiber optic coupler used in the interferometer (see Section 3.3 for details). A bellows-seal right angle valve leads to the pumps.

A Pfeiffer TMU 071 turbopump is mounted on top of the optical table and very close to the microscope insert to maximize conductance and thus pumping efficiency. It is connected to the insert valve via a flexible bellows and a KF50 flange. The KF style flange is used here because the flange is regularly connected and disconnected in order to insert or remove the microscope from the dewar. The flexible bellows, with a diameter of 4.5 inches and a length of 6 inches, provides some isolation of turbopump vibrations from the microscope, while maintaining good conductance. The Pfeiffer turbopump was chosen because of its exceptionally high compression ratio, which allows for quick pumping of even helium gas down to low pressures. A Varian SH-100 scroll pump, housed inside a pump room adjacent to the MFM setup, is used to back the turbopump. Two sections of thin-wall flexible metal hose are used to connect the scroll pump to the roughing port of the turbopump. The sections are connected via a vacuum nipple which is solidly mounted in the wall between the pump room and the MFM to reduce the coupling of scroll pump vibrations to the rest of the system.

The vacuum pressure is measured by a Pfeiffer Full-Range Gauge, which combines a Pirani gauge for high pressures (above 10^{-2} Torr) and a cold cathode gauge for low pressures (down to 10^{-9} Torr). The vacuum system is rounded out by a double-valve setup for introducing gases into the system, both for introducing helium exchange gas into the system for faster cooling, and for venting the system (this can also be done using an automatic valve on the turbopump). The double valve setup provides some control over the volume of gas introduced into the vacuum space. The system is always vented using nitrogen gas, in order to prevent water vapor from accumulating on surfaces inside the vacuum space, which is difficult/time consuming to pump out for the next experiment. Additionally, when the microscope is open for only a short period of time, nitrogen gas is flowed through the system using the double valves. This results in a pumpdown time which is typically an order of magnitude faster compared to when the microscope has been open to air.

When setting up an experiment, a leak detector is never used, in part because the leak detector in the Moler lab uses an oil-based roughing pump, which could potentially introduce oil molecules into the vacuum space, but primarily because it has not been necessary and thus has not been worth spending time on. Problems may be detected by tracking the pressure versus time from the start of the pumpdown, and comparing the curve to previous pumpdowns. Typical pumpdown curves are illustrated in Figure 3-3.

During an experiment, once the insert is at cryogenic temperatures, the pumps can be turned off to eliminate vibrations. This can be done by closing the valve to the vacuum space, shutting down the pumps and venting the pumps and pump lines with nitrogen. The pressure inside the insert typically goes down when the valve is closed, because cryopumping of gases by the cold walls of the vacuum tube is more effective than the turbopump, and also because the room temperature pump lines are no longer connected to the main vacuum space. When restarting the pumps, the lines should be pumped for some time (about a half hour is probably sufficient) before opening the valve to the vacuum space, so that the pressure in the lines is near the level inside the microscope.

3.1.2 Cryogenics

The microscope insert goes into a vapor shielded liquid helium dewar with a 5 T superconducting magnet. The vapor shielded dewar, manufactured by Precision Cryogenics, has an extra long neck (28 inches, compared to a more standard length of 18

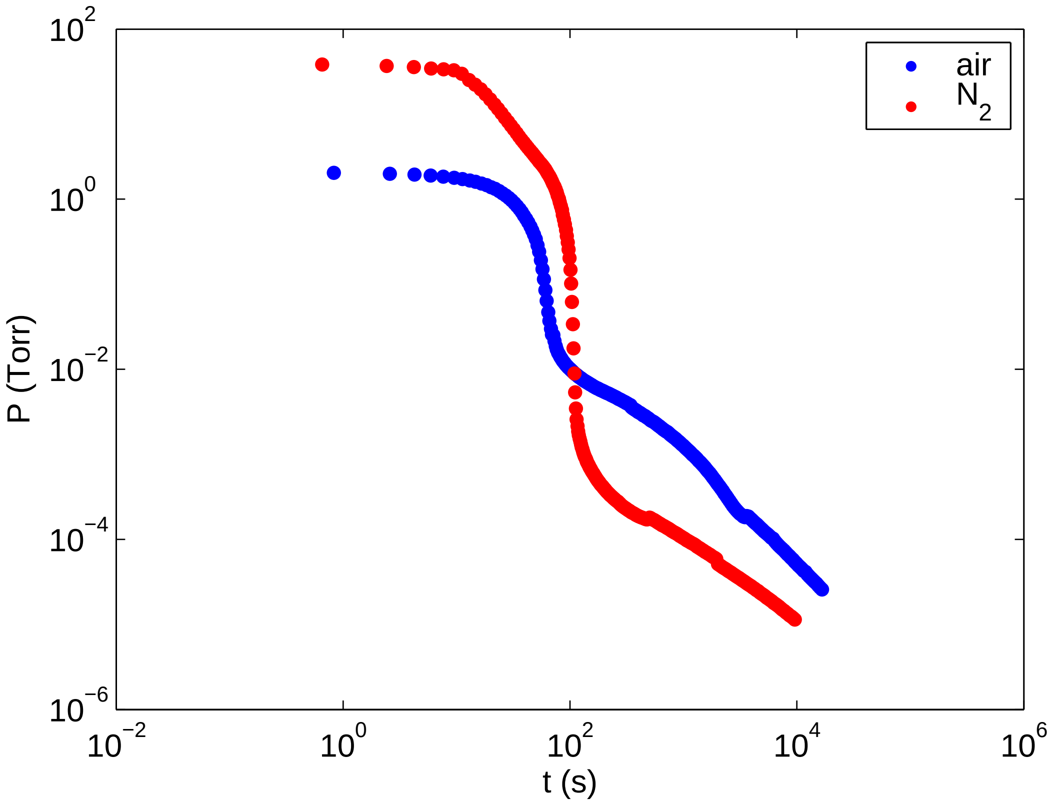

Figure 3-3: Typical pumpdown curves for the magnetic force microscope. The pumpdown is typically one order of magnitude faster when the system has been vented from high vacuum with nitrogen gas, and flushed with a continuous flow of nitrogen gas when open to air before pumping down again.

inches) to reduce the helium boiloff rate. Vapor shielding was chosen because it generates less vibration than shielding with a liquid nitrogen jacket. The dewar has a belly volume of 70 L, which lasts about 5 to 7 days depending on magnet usage. The 5 T magnet, manufactured by American Magnetics, has a 4 inch bore size, leaving good clearance for insertion of the microscope insert. The microscope head rests at the center of the magnet during an experiment. Helium boiloff is further reduced through the use of "break-away" magnet leads. When the magnet is not in use, or when a persistent current is set up in the magnet, the heavy copper leads may be disconnected above the helium bath in order to reduce the thermal conduction and the resultant helium boiloff.

The inside of the insert is cooled by conduction through the indium seal flanges, and by radiative cooling from the cold inner walls of the insert. Baffles inside the vacuum space reduce the heat leak due to room temperature radiation, and thin walled stainless steel tubes are used for the vacuum tube and microscope head support structure to minimize the heat leak due to conduction. The indium seal flanges are made of copper. Copper braid connects the baffles to the flanges for cooling. A copper block is mounted on the microscope head to serve as the thermal bath and to help regulate the temperature of the cantilever and sample. Copper braids connect the block to the flanges, and the cantilever mounting assembly and sample holder to the copper block. A 25 W heater is also mounted in a hole in the center of the block for temperature control, and a LakeShore Cryogenics Cernox sensor is mounted to the outside of the block using an indium foil gasket and a copper clamp. The temperature control setup is pictured in Figure 3-4 and Figure 3-5. The temperature of the microscope reaches down to 78 K with liquid nitrogen, and about 5.2 K with liquid helium. Improved cooling could likely be obtained by adding more copper braids to increase the cooling power.

To cool the microscope, the insert is lowered into the warm dewar, and pumped down to about 10^{-5} Torr. The bath is then filled with liquid nitrogen to cool the dewar. The microscope can be operated at this stage, or the nitrogen can be removed by pressurizing the dewar with nitrogen gas and blowing it out through a tube extending to the bottom of the dewar. After removing the liquid nitrogen, the dewar can be cooled further with liquid helium. Typical temperature curves during cooling are shown in Figure 3-6. Helium

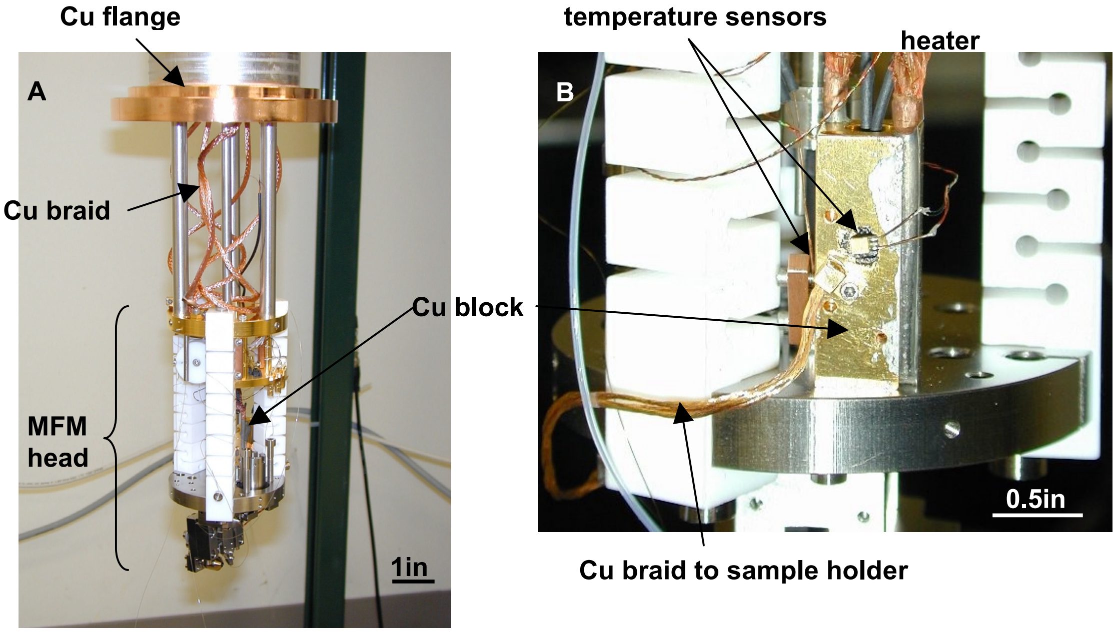

Figure 3-4: The temperature control system of the microscope. (A) Copper braids make a thermal connection between the microscope head and the copper flange which directly contacts the liquid helium bath. (B) A heater and two temperature sensors are mounted in/on a gold plated copper block on the microscope head (one temperature sensor failed during a cooldown, the second was subsequently added at the same location as a backup). Additional copper braid connects the cantilever mount and the sample holder to the copper block.

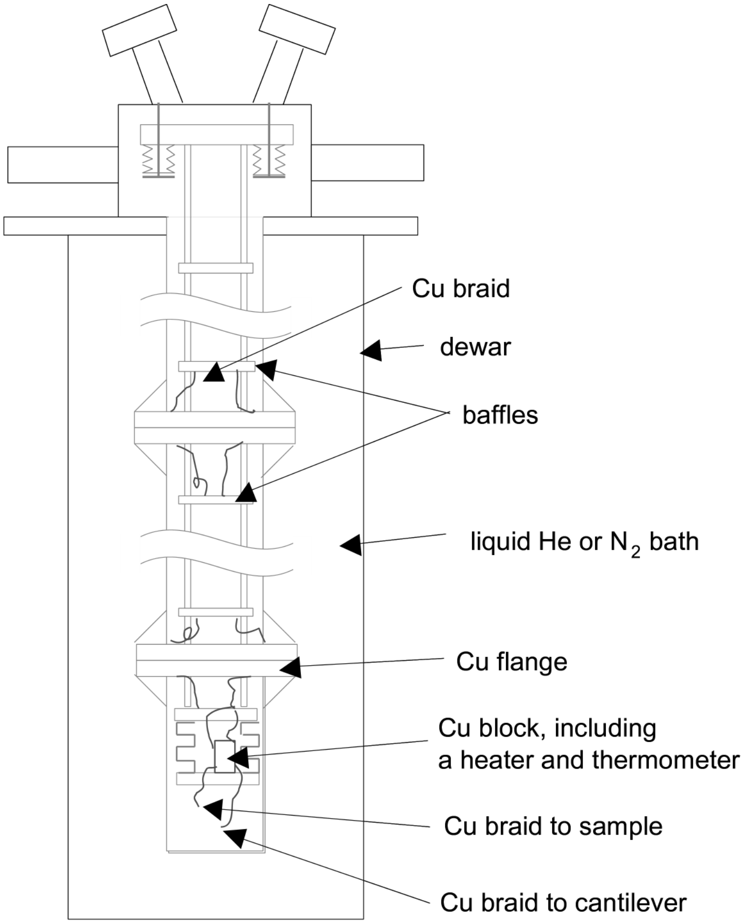

Figure 3-5: An illustration of the temperature control setup in the microscope. Copper braids connect the baffles and a Cu block to the Cu flanges, which are in contact with the cryogen bath. A heater and temperature sensor are also mounted inside the Cu block to allow for temperature control. Additional copper braid connects the sample holder and cantilever to this Cu block.

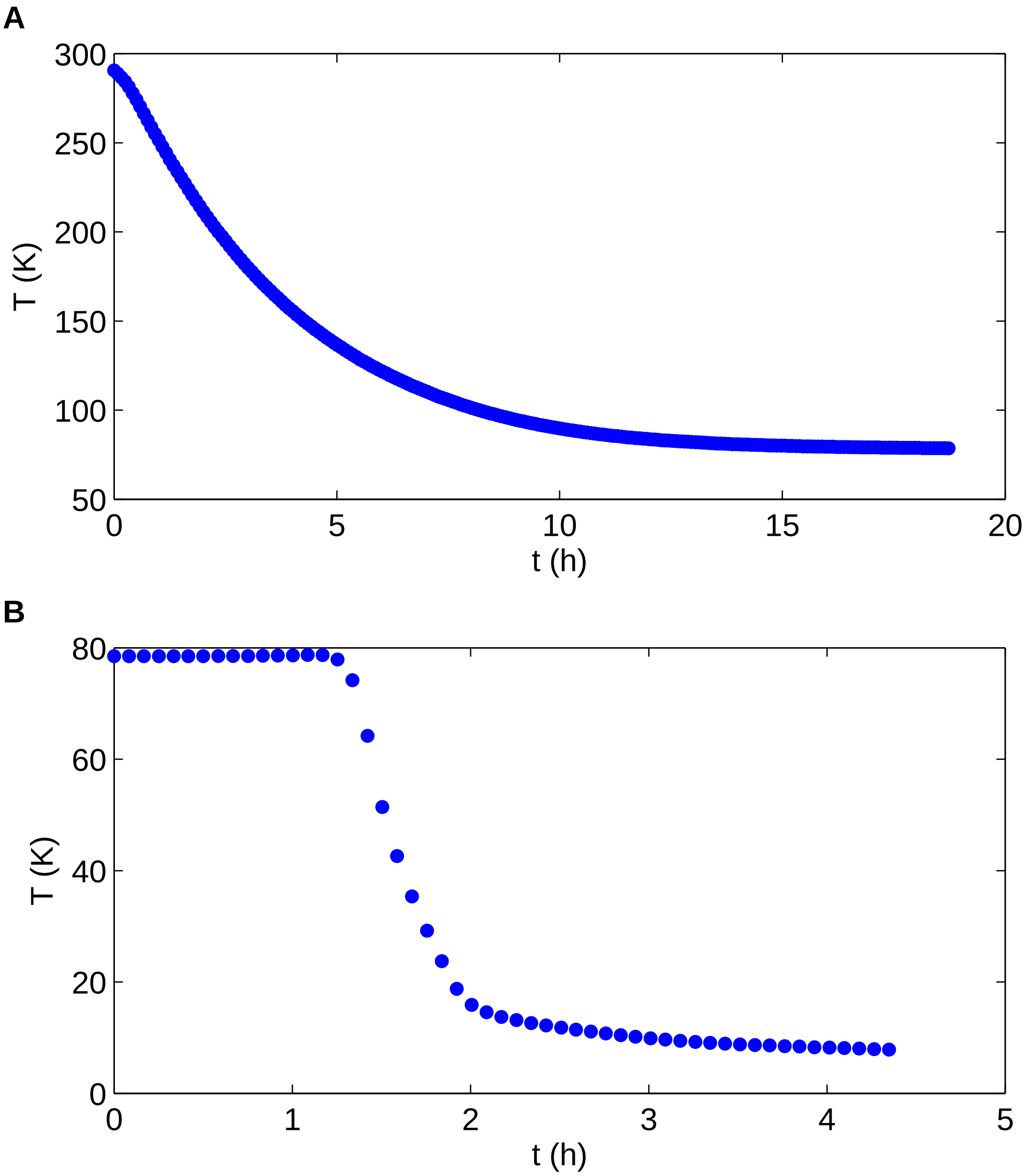

Figure 3-6: Cooldown curves for the MFM. (A) Precooling with liquid nitrogen. (B) Blowing out the nitrogen and cooling with liquid helium. Helium exchange gas can be used to promote faster cooling, but was not used here.

exchange gas can be added to increase the rate of cooling, but this has generally not been done to date.

After completing an experiment, any remaining cryogens can be removed from the dewar. The system can then be left in the dewar to warm up. Alternatively, for a faster turnaround, the insert can be removed from the dewar to warm up at room temperature. To do this, the dewar is allowed to warm up to 80 K or higher. While flowing nitrogen gas through the dewar at a high rate to prevent water from entering, the insert (still under vacuum, to prevent a warmup that is too rapid) is removed from the dewar, and the neck is sealed with an aluminum plate. The insert is then allowed to warm up to about 270 K or higher before venting with nitrogen gas. Typical warmup curves are shown in Figure 3-7. Warming the system up too rapidly can lead to damage in the piezos, although the temperature increases sufficiently slowly with both methods described here.

3.1.3 Vibration Isolation

There are three separate mechanisms for isolating the microscope head from external vibrations, as illustrated in Figure 3-8. The first two mechanisms are pictured in Figure 3-9. To start, the dewar is mounted in the center of a TMC optical table, which is floated on three air legs to minimize the effect of floor vibrations. The tripod arrangement is used because the location of the floor pit in the corner of the room would prevent access to a leg in the far corner of the table, which could be a problem if work needed to be done to repair an air leak for example. Thus, there is only one leg in the middle of that side of the table. Further vibration isolation is inside the vacuum space of the microscope. The microscope hangs from a trio of flexible bellows, which are under compression. At the bottom of the system, there are three springs machined from teflon (visible in Figure 3-4 and Figure 3-10) which provide the final level of isolation for the head itself. The teflon should damp any vibrations which arise in the system.

These three levels of vibration isolation should all help to reduce the effect of external vibrations on the microscope. However, their effectiveness has never been characterized. Although external vibrations have never been observed to be a problem during imaging, it would likely be useful to systematically characterize the vibrations in the system,

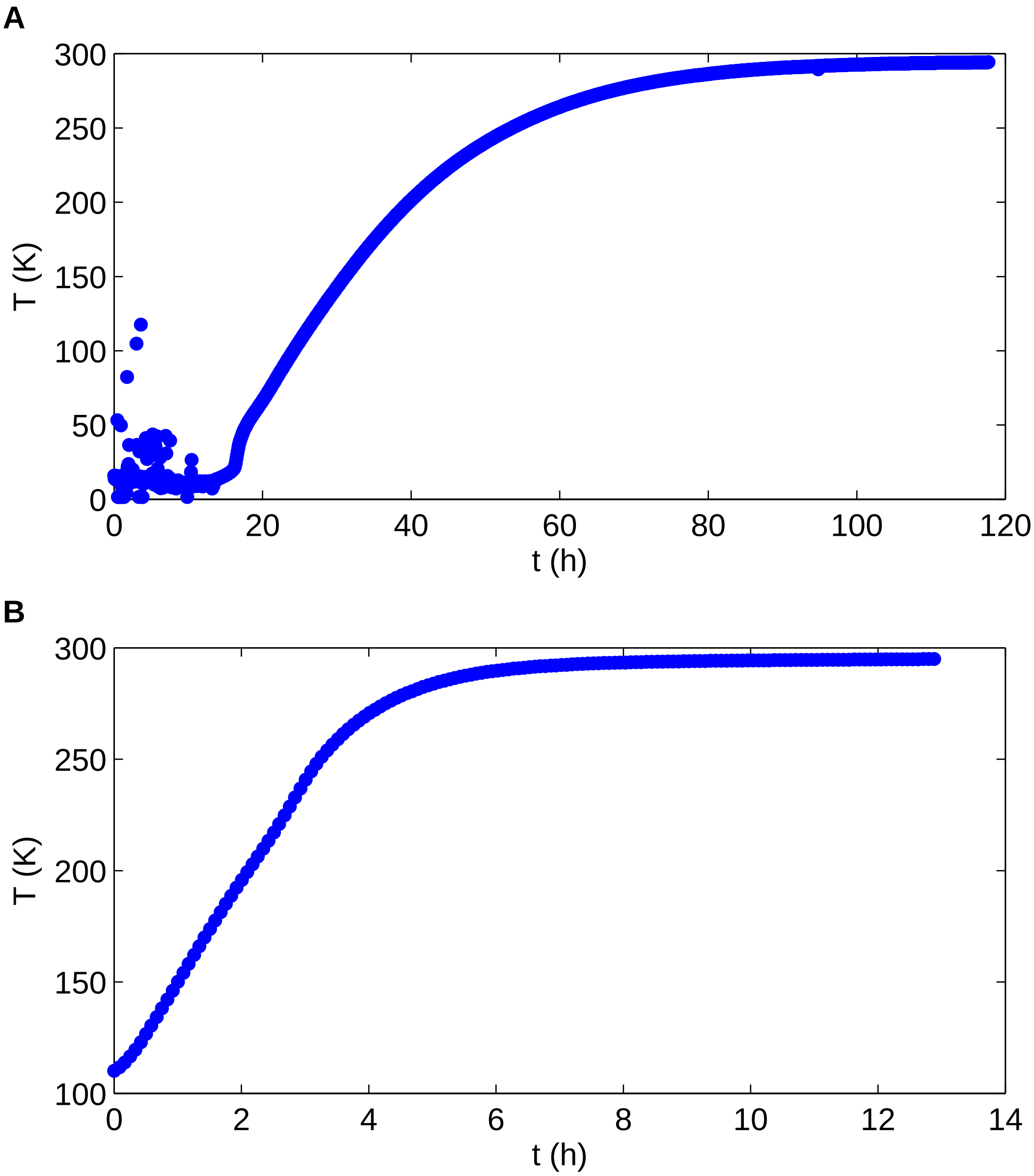

Figure 3-7: Temperature versus time when warming up the MFM. (A) It takes roughly 3 days for the insert to warm to room temperature when it is left in the empty dewar. (B) The insert can be removed from the dewar for a faster warmup.

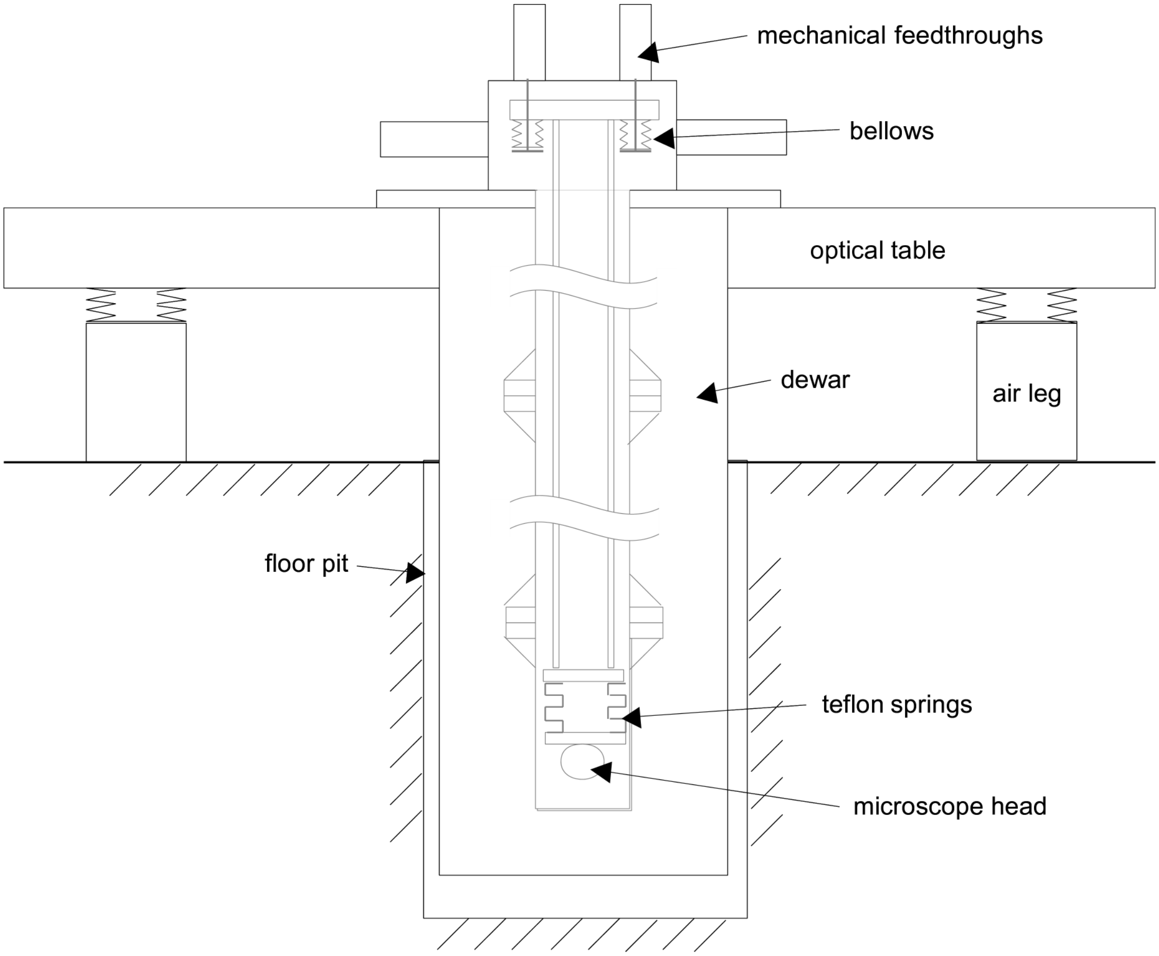

Figure 3-8: An illustration of the vibration isolation setup in the microscope. Initial vibration isolation is provided by a set of three air legs on which the optical table and dewar are supported. Additional isolation is provided by three bellows and three teflon springs inside the microscope. Only two members of each set of isolators are shown in the diagram for clarity of the drawing.

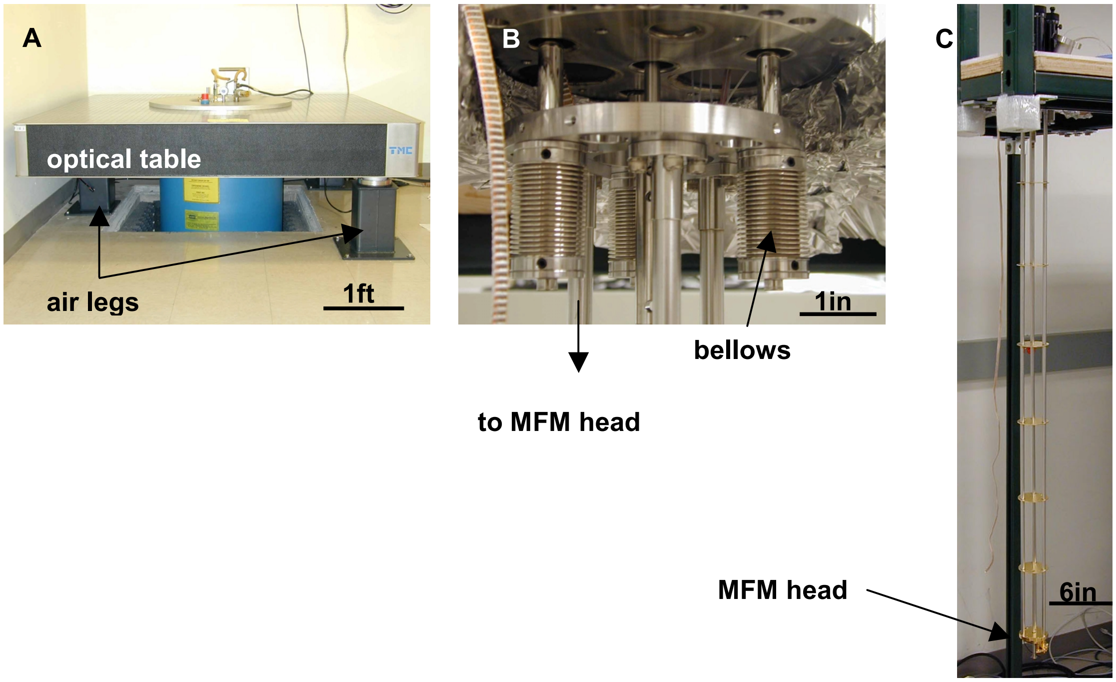

Figure 3-9: There are several mechanisms for vibration isolation incorporation into the MFM system. (A) The vapor shielded helium dewar is supported by an optical table, which can be floated on top of three air legs to reduce the effect of floor vibrations on the microscope. (B) Inside the vacuum space, the microscope head hangs from three thin walled rods, which are supported by a set of three flexible bellows. The bellows provide a second level of vibration isolation. At the microscope head itself, three teflon springs provide a third level of vibration isolation.

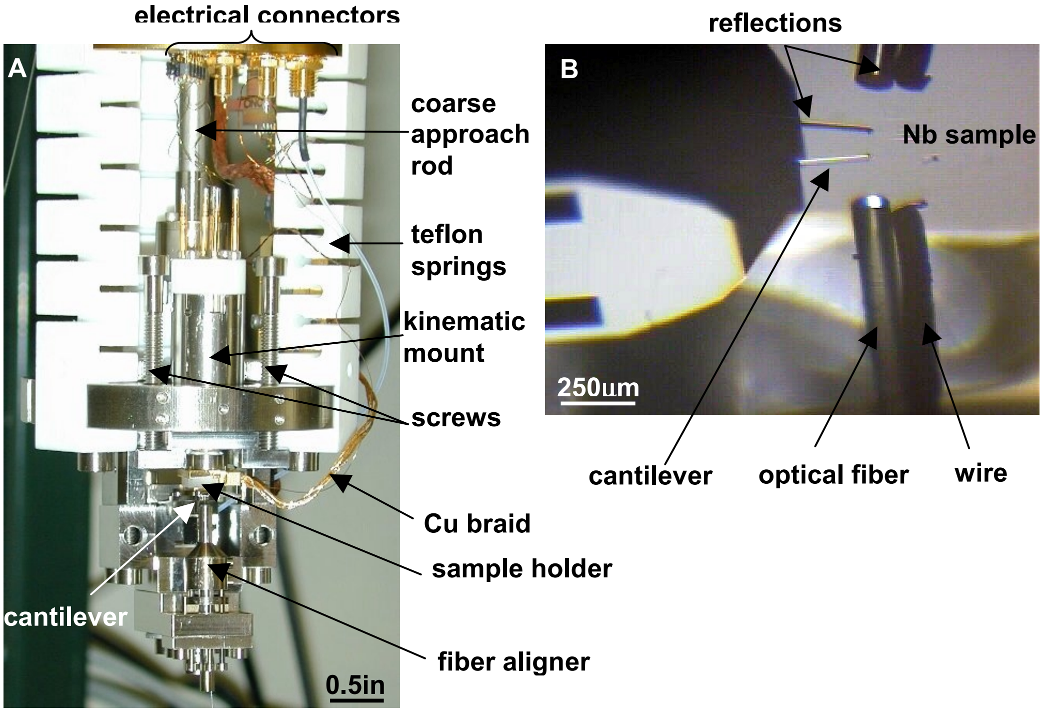

Figure 3-10: The microscope head. (A) The piezotube is mounted on a kinematic mount supported by three screws, one of which can be turned at low temperatures using a stepper motor and rotary vacuum feedthrough to enable coarse approach of the sample and cantilever. The cantilever is mounted below the piezotube. A mechanical apparatus is used to align the optical fiber with the cantilever, and a piezostack is used to fine-tune the fiber-cantilever separation. (B) An optical microscope image of a cantilever near the surface of a sample. The reflections of the cantilever and optical fiber are visible in the sample surface. Also visible in this picture is a wire, which at one point in time was used to capacitively drive the cantilever. This wire is no longer in place however, and the cantilever is driven by a voltage applied to the sample.

particularly as the resolution is improved, and if any atomic force microscopy is attempted.

3.1.4 Design of the Microscope Head

The microscope head is pictured in Figure 3-10. A 3 inch diameter x 3/8 inch thick titanium disk serves as the base for the head. The cantilever is mounted on an assembly which also holds the optical fiber of the interferometer. Coarse alignment of the fiber to the cantilever is done by positioning the assembly components appropriately before fastening them together. Fine x-y adjustment is accomplished by bending a titanium fiber holder using a set of four 0-80 screws which push the holder in the desired direction. Fine adjustment of the fiber-cantilever separation is accomplished using a high voltage piezo stack. The piezotube is mounted on a kinematic mount just above the cantilever-fiber assembly. This is described in the following section.

Electrical connections between the vacuum feedthroughs and the microscope head are made using three sets of wires. The first set is a ribbon cable made by Oxford Instruments containing 3 twisted pairs of 42 AWG copper wire and 9 twisted pairs of 42 AWG constantin wire. This ribbon cable, specifically designed for use in low temperature systems, is very well suited for its purpose. It provides a large number of wires in an organized manner, and the weave holding the twisted pairs together also protects the wires from damage. 4 pairs of constantin wires are used for the temperature sensors (one pair for current and one pair for voltage for each sensor) and one pair of copper wires for the heater. The remaining wires are available for future connections. The ribbon cable is terminated with a 25 pin mini D-sub connector. Wires from the temperature sensors and heater are soldered to a mating connector. I have found this connector to be too compact to facilitate easy connection of the wires, and although I am very satisfied with the ribbon cable, I would likely choose a different connection method if I were to redesign the system.

A second set of wires is used for the high voltages applied to the scan piezotube. 5 twisted pairs of 5 mil manganin wire are terminated with a Samtec connector, which is subsequently connected to the piezotube electrodes. The wires, made by California Fine

Wire, are insulated with a polyimide coating which can handle the high (450 V) voltages used for scanning.

The final set of wires is a set of three coaxial cables, terminated by SMA and SMB connectors. One is used for the connection to the piezostack for fiber-cantilever positioning, and another is used to apply a voltage to the sample surface, with the third wire available for future use. Twisted pairs were not sensible for these connections since the microscope ground serves as the ground for these voltages and thus there is no sensible wire with which to pair these wires. The coaxial cable is connected to the microscope on one end only and is used here to provide shielding from noise.

3.1.5 Piezotube

A piezoelectric tube is used for high resolution positioning during scanning. The tube, manufactured by Staveley Sensors, has quadrant silver electrodes, and one center electrode. The tube is epoxied into a Macor holder, which is then fastened to a titanium kinematic mount using screws. Wires are silver epoxied to each electrode, and terminated by pin connectors embedded in the Macor piece, such that the wires are never directly handled and are thus protected. A titanium piece is epoxied into the other end of the piezotube. The sample holder is attached to the piezotube by fastening it to the titanium mount using three 0-80 screws.

3.1.6 Coarse Approach

Coarse approach is perhaps the most demanding and difficult aspect of designing a functional low temperature scanning microscope. A variety of devices have been designed for accomplishing the tasks (Besocke 1987; Hug et al. 1993; Pan et al. 1999). For this microscope, I chose to use a screw based mechanism because of its relative simplicity.

The piezotube is mounted on a kinematic mount supported by three screws with rounded ends. Two of the screws have an 8-32 thread and are adjustable only when the microscope is open for manual adjustment with a ball drive or Allen wrench. The third screw is a ¼-80 fine pitch screw, and can be turned using a long rod attached to a rotary feedthrough. This allows for coarse approach when the vacuum system is sealed.

Typically, during the setup of the experiment at room temperature, the sample is brought close to the cantilever using all three screws. It is common to have a small (5 to 10º) angle between the cantilever and sample, to ensure that the tip touches the sample surface before any of the mounting apparatus gets in the way. The fine pitch screw is used to retract the sample slightly, to allow for the microscope head to contract during cooldown without crashing the tip.

Once in vacuum and at the desired measurement temperature, the coarse approach screw is turned in small increments to bring the sample towards the cantilever. After each step, the piezotube is extended and a trace of frequency shift versus z is measured. This signal is used to detect the proximity of the sample and cantilever. Near the surface, there is a large frequency shift, which may be used to determine the surface location. A typical curve is shown in Figure 3-11. For some further discussion of this surface finding procedure, please see Section 3.7.2.

The coarse approach mechanism is quite susceptible to failure, and on several occasions the fine pitch screw has seized, ending an experiment prematurely. The screw and its mate are made of the same material to prevent either undue tightening or loosening at low temperatures as the materials contract, and the small, tight fitting threads can seize relatively easily. Stainless steel and titanium have been used, with both exhibiting problems after long-term use. To minimize the likelihood of a screw seizure, the screw and hole threads are lubricated with MoS_2 dry lubricant. Also, to minimize the consequences of a seizure, the mating part has been designed as a removable, easily replaceable insert which is mounting onto the main body of the microscope head, avoiding the need for major disassembly and machining of the entire assembly for repairs.

The most recent design for the coarse approach screw is a titanium differential screw, combining a 5/16-24 and an 8-32 screw for an effective pitch of 96 threads/inch. This has not yet been tested, but it should be less susceptible to seizure because the larger threads do not fit as tightly as the fine-pitch threads of the previous screw. Vibrations however may be an issue. In the long run, a major redesign of the microscope head is desirable to incorporate a piezo-based coarse motion device such as the design developed by Shouheng Pan (Pan et al. 1999). Piezo-based coarse motion devices are now available

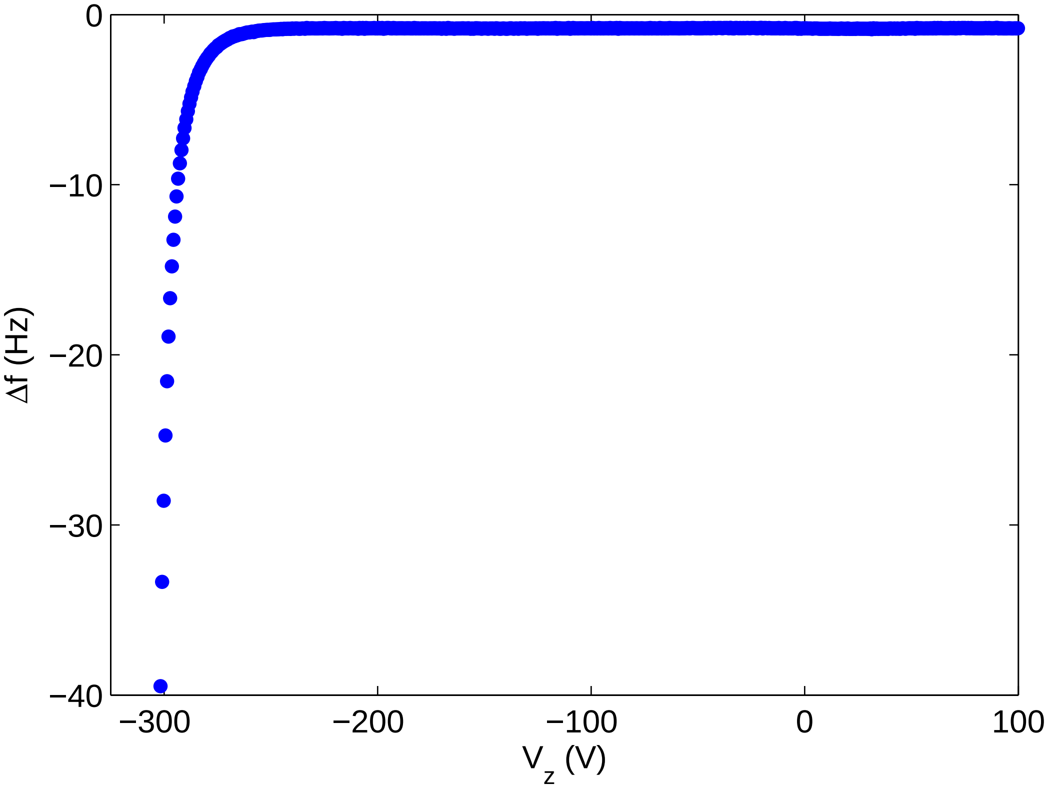

Figure 3-11: I determined the position of the sample surface by measuring the frequency shift as the tip-sample separation was decreased. When the cantilever frequency exceeded a setpoint (about 40 Hz), the cantilever tip was deemed to have reached the surface. Here this event occurred with –301 V applied to the z electrode of the scan piezotube.

commercially from Attocube Systems AG, but they were not available at the time this microscope was constructed.

3.2 Cantilevers

There are many available options for cantilevers for use in a magnetic force microscope. Commercial MFM cantilevers are available. These are made by coating AFM cantilevers with a sputtered magnetic film to make them sensitive to magnetic fields. However, as the films cover the entire cantilever, they tend to dramatically reduce the quality factor. This can potentially reduce the sensitivity, in the case of thermally limited measurements. Also, the magnetic moment tends to be fairly large, which can be useful for generating a large signal when imaging a hard magnetic sample which is not significantly disturbed by the tip field, but it can be problematic when imaging a sensitive sample such as vortices in a superconductor. Commercial MFM cantilevers were used in our MFM initially, but are not currently used.

AFM cantilevers can also be used after evaporating a suitable film onto the tip oneself. Piezoresistive cantilevers have been used in low temperature MFM's. They have the advantage of not requiring alignment of a deflection sensor to the cantilever. However, the sensitivity is not as good for piezoresistive detection as it is for interferometer detection. Also, piezoresistive heating leads to cantilever heating. I used commercial single crystal silicon AFM cantilevers, generally models fabricated by MikroMasch, a company which offers a wide range of cantilevers at competitive prices.

A fiber optic interferometer, described later in Section 3.3, is used as the deflection sensor. Cantilever tips are coated by shadow masking the cantilever using a razor blade, and evaporating a magnetic thin film on the exposed tip. The alignment setup is shown in Figure 3-12. A titanium adhesion layer is evaporated first, followed by a layer of iron or cobalt, and finally a layer of gold to prevent oxidation. The tip is magnetized at the start of an experiment by bringing a NdFeB rare earth magnet close to the tip momentarily.

In selecting an AFM cantilever, there are a number of factors to consider. First, the sensitivity must be considered. The thermally limited minimum detectable force gradient is given by Equation (2.11). Substituting $k = Ywt^3/4l^3$ and $\omega_o = \sqrt{k/0.24m} \cong \sqrt{4k/\rho lwt}$ for the cantilever spring constant and resonant frequency, this becomes:

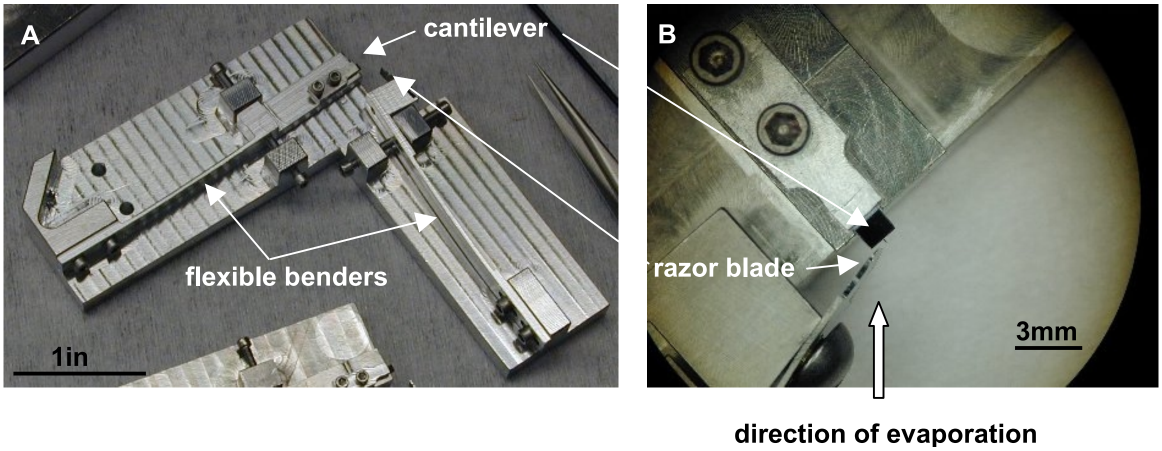

Figure 3-12: The razor blade aligner used to shadow mask the cantilever for coating the tip with a magnetic film.

$$F'_{\min} = \frac{1}{A}\sqrt{\frac{wt^2}{l}\frac{k_B TBW}{Q}}\left(Y\rho\right)^{1/4} \tag{3.1}$$

The sensitivity is optimized by using cantilevers which are narrow, thin, and long, and which have high quality factors. For the case of deflection sensor limited sensitivity, Equation (2.13) gives:

$$F'_{\min} = \frac{1}{2\sqrt{3\pi}}\frac{wt^2}{l}\sqrt{Y\rho}\,\frac{n_{\Delta x}}{A}BW^{3/2} \tag{3.2}$$

As for the case of thermal noise, narrow, thin, and long cantilevers minimize the sensitivity. However, the quality factor does not affect the minimum detectable force gradient, and the sensitivity does not improve at lower temperatures.

For both thermal noise and deflection sensor noise limited measurements then, low spring constants would appear to be desirable for optimizing the signal to noise ratio. However, as the spring constant is reduced, the tip-sample separation at which the cantilever will jump into contact with the sample surface (snap-in) occurs increases. It is necessary to strike a balance between stiffness, in order to image at smaller separations, and softness, in order to maximize the SNR. It should also be noted that the force gradient (i.e. the signal) will be stronger close to the sample, such that a stiffer cantilever will obtain a better SNR because it can operate closer to the sample, such that the signal increase outweighs the decrease in sensitivity. Very close to the sample however (on the scale of 10 nm) the force gradient will be dominated by atomic sources rather than magnetic ones, placing a limit on how close the cantilever can get to the surface while still measuring magnetic effects.

The cantilevers that I have primarily used are MikroMasch NSC18 levers, with an aluminum coating on the backside. The aluminum coating does reduce the quality factor of the cantilevers, but it is sufficiently thin that the performance of the cantilever is adequate. The cantilevers have a spring constant in the range of 3.5 ± 1.5 N/m, and a resonant frequency in the range of 75 ± 15 kHz. I have also tried cantilevers with lower spring constants, but was not successful in obtaining images with them due to high noise levels. At the time the noise problem described later in Section 3.6 was not yet solved, and it is likely that it was responsible for the difficulties I had using low k cantilevers. It is probably worth reexamining the suitability of softer cantilevers for MFM measurements because of their potential to provide an increased signal to noise ratio.

For a specific cantilever used in a measurement, the actual resonant frequency can be measured using a spectrum analyzer or a frequency detector. The spring constant can be then determined from the cantilever dimensions and the measured resonant frequency using the following:

$$\begin{aligned} k &= \frac{Ywt^3}{4l^3} \\ &= 1.88\pi^3 \sqrt{\frac{\rho^3}{Y}} wl^3 f_o^3 \end{aligned} \tag{3.3}$$

For silicon, the density $\rho = 2330\, kg/m^3$, and Young's modulus $Y = 190 GPa$ (Yasumura 2000). Values for the width and length can be obtained from the cantilever datasheet, or they can be measured in an optical or scanning electron microscope.

It is also necessary to consider the type of tip on the cantilever. The tip should be sharp to obtain good resolution, although a very sharp tip is likely to be fragile and could be easily blunted and damaged during an accidental touchdown. The quoted typical radius of curvature for the NSC18 cantilevers is 10 nm, which should be sufficient for many MFM measurements. Electron-beam deposition (EBD) tips (Skidmore and Dahlberg 1997) can also be purchased from MikroMasch. Alternatively, nanotube tips (Deng et al.) are promising for use as MFM tips. In all these cases, the tip must be coated with a magnetic film to be used for MFM.

3.3 Interferometer

I implemented a fiber optic interferometer (Rugar et al. 1989) as the deflection sensor in this microscope. An InGaAsP Fabry-Perot laser diode with a wavelength of 1310 nm, manufactured by PD-LD, serves as the light source for the interferometer. This wavelength is used because it is above the bandgap in silicon such that light absorption, which causes cantilever heating and has also been found to affect the cantilever frequency (Rugar et al. 2001), is minimized. The laser diode is packaged with an FC receptacle for simple connection to the optical fiber. A dual stage optic isolator with FC-APC connectors joins the laser diode to the primary input of a 10/90 coupler. The isolator allows light to enter the coupler from the laser diode, but attenuates light reflected back to the laser by 58 dB, in order to prevent instabilities in the laser caused by optical feedback.

The coupler splits the laser light, transmitting 90% of the light through the primary output, and the remaining 10% through the secondary output. The primary output is terminated with an FC-APC connector, which provides greater than 60dB of return loss and thus minimizes the light reflected back to the coupler. It can serve as a reference signal for the interferometer, and in particular can be monitored to measure the laser power and noise. The secondary output is a bare optical fiber which enters the microscope vacuum space through a custom conflat feedthrough, and terminates at the microscope head. A microcapillary glass ferrule (made by Friedrich & Dimmock, Inc.) holds the end of the fiber in place for alignment to a cantilever. The fiber end is cleaved to give a reflective surface, reflecting some of the incident light. Some of the light transmitted out of the fiber end is reflected from the backside of the cantilever to which it is aligned, and reenters the fiber. Interference occurs between the light reflected from the cantilever and the light reflected from the fiber end, providing the cantilever deflection signal. This reflected light reenters the coupler. 10% of the light from the secondary output plus 90% of the light reflected from the primary output goes to the laser, attenuated by the isolator as mentioned previously. 90% of the light from the secondary output plus 10% of the light from the primary output is transmitted through the secondary input of the coupler. The secondary input is terminated with an FC-APC connector, and is connected to an InGaAs photodetector manufactured by New Focus.

The interferometer signal can be modeled by considering a two-reflection system. The reflected light energy is:

$$E = r_f E_i + r_c t_f^2 E_i e^{j\theta} \tag{3.4}$$

where E_i is the incident light energy, r_f and t_f are the reflection and transmission coefficients from the fiber end, and r_c is the cantilever reflection coefficient. θ is the optical path length difference between the fiber and cantilever reflections, given by:

$$\theta = \frac{4\pi d}{\lambda} \tag{3.5}$$

where λ is the laser wavelength and d is the fiber-cantilever separation. The total reflected power P is then:

$$\begin{aligned} P &= \left| r_f E_o + r_c t_f^2 E_i e^{j\theta} \right|^2 \\ &= E_i^2 \left(r_f^2 + r_c^2 t_f^4 + 2 r_f r_c \cos\theta \right) \\ &= P_i \left[R_f + R_c \left(1 - R_f\right)^2 + 2\sqrt{R_f R_c} \cos\theta \right] \end{aligned} \tag{3.6}$$

where $R_f = r_f^2 = \left(1 - t_f^2\right)$ and $R_c = r_c^2$ are the power reflection coefficients. For an ideal cleave, the fiber reflection is given by:

$$\begin{aligned} R_f &= \left(\frac{n_{fiber} - n_{vacuum}}{n_{fiber} + n_{vacuum}} \right)^2 \\ &\cong 0.04 \end{aligned} \tag{3.7}$$

where n_{fiber} and n_{vacuum} are the indices of refraction of the optical fiber and vacuum respectively, equal to 1.5 and 1. Since $R_f \ll 1$:

$$P \cong P_i \left(R_f + R_c + 2\sqrt{R_f R_c} \cos\theta \right) \tag{3.8}$$

This equation may be further simplified by defining an average power P_o:

$$\begin{aligned} P_o &= \tfrac{1}{2}\left(P_{\max} + P_{\min} \right) \\ &= P_i \left(R_f + R_c \right) \end{aligned} \tag{3.9}$$

where P_{max} and P_{min} are the maximum and minimum reflected powers, and a visibility *v*:

$$\begin{aligned} v &= \frac{P_{\max} - P_{\min}}{P_{\max} + P_{\min}} \\ &= \frac{2\sqrt{R_f R_c}}{R_f + R_c} \end{aligned} \tag{3.10}$$

This results in the following equation for P:

$$P = P_o\left(1 - v\cos\frac{4\pi d}{\lambda}\right) \tag{3.11}$$

The interferometer response to a cantilever motion (i.e. a change in the fiber-cantilever separation d) is given by:

$$\frac{\Delta V}{V_o} = \frac{\Delta P}{P_o} = \frac{4\pi v}{\lambda}\sin\frac{4\pi d}{\lambda}\Delta d - \frac{4\pi v d}{\lambda^2}\sin\frac{4\pi d}{\lambda}\Delta\lambda \tag{3.12}$$

where V_o is the average voltage from the interferometer and ΔV is the voltage change. $\Delta\lambda$ is ideally small, such that the second term can be neglected. The interferometer is most sensitive to cantilever motion Δd when $d = n\lambda/8$, with n odd. The interferometer is operated at this point. To calibrate the interferometer, the signal is measured as a function of fiber-cantilever distance. The maximum and minimum voltages are averaged to determine P_o, which is used as the setpoint for the interferometer. The interferometer calibration is given by:

$$\begin{aligned}\frac{\Delta d}{\Delta V} &= \frac{\lambda}{4\pi v V_o} \\ &= \frac{\lambda}{2\pi\left(V_{\max} - V_{\min}\right)}\end{aligned} \tag{3.13}$$

$V_{\min}$ and $V_{\max}$ are the minimum and maximum interferometer voltages measured as a function of the fiber-cantilever separation. They are measured experimentally by sweeping through a range of d using the piezoelectric stack described in Section 3.1.4.

3.3.1 Noise levels

The noise in the measurement of the cantilever deflection is due to cantilever thermal noise, and interferometer noise. As shown in Figure 3-13, thermal noise is dominant at the resonant frequency, while away from the resonant peak interferometer noise is dominant. Interferometer noise results from laser noise, Johnson noise (δV_J), and shot noise (δV_{sh}) (Sarid 1991), where laser noise occurs as both intensity noise (δV_{li}) and phase noise (δV_{lp}):

$$\delta V_{int} = \sqrt{\langle \delta V_{li}^2 \rangle + \langle \delta V_{lp}^2 \rangle + \langle \delta V_J^2 \rangle + \langle \delta V_{sh}^2 \rangle} \tag{3.14}$$

The fundamental limit for the interferometer noise is given by the shot noise contribution. Shot noise is described by the following equation:

$$\langle \delta V^2 \rangle_{sh}^{1/2} = R\sqrt{2e\eta P_o BW} \tag{3.15}$$

where R is the resistance of the resistor used for current to voltage conversion in the photodetector, e is the electronic charge, and η is the photodiode efficiency. The signal from the interferometer is proportional to the change in power ΔP, giving a signal to noise ratio (SNR) described by:

$$\begin{aligned} SNR &\sim \frac{\Delta P}{\sqrt{P_o}} \\ &= 4\pi V \sqrt{P_o} \frac{\Delta d}{\lambda} \end{aligned} \tag{3.16}$$

The minimum measurable displacement decreases as $P_o^{-1/2}$. The interferometer displacement sensitivity was measured as a function of the power incident on the photodetector. The power was changed by adjusting the connection between the laser and the fiber coupler (by screwing the FC connector into the receptacle to varying degrees), so as to change the power without changing the laser current and thus potentially the laser noise, following which the noise level was measured with a spectrum analyzer. The results from this measurement are shown in Figure 3-14. Roughly, the deflection sensitivity does decrease linearly as a function of $P_o^{-1/2}$, indicating that the interferometer noise is dominated by shot noise.

Knowing that shot noise limits the sensitivity of the interferometer, it would seem that the performance could be improved by simply increasing the laser power. However, there are a few things to consider before doing so. First, increasing the laser power could lead to increased heating in the cantilever and sample (Rugar et al. 2001). Second, when using particularly low k or high Q cantilevers, the laser light can drive or damp (depending on which side of the fringe the interferometer is operating on) the cantilever motion. Finally, the laser power can be increased by increasing the current used to drive it, but at some

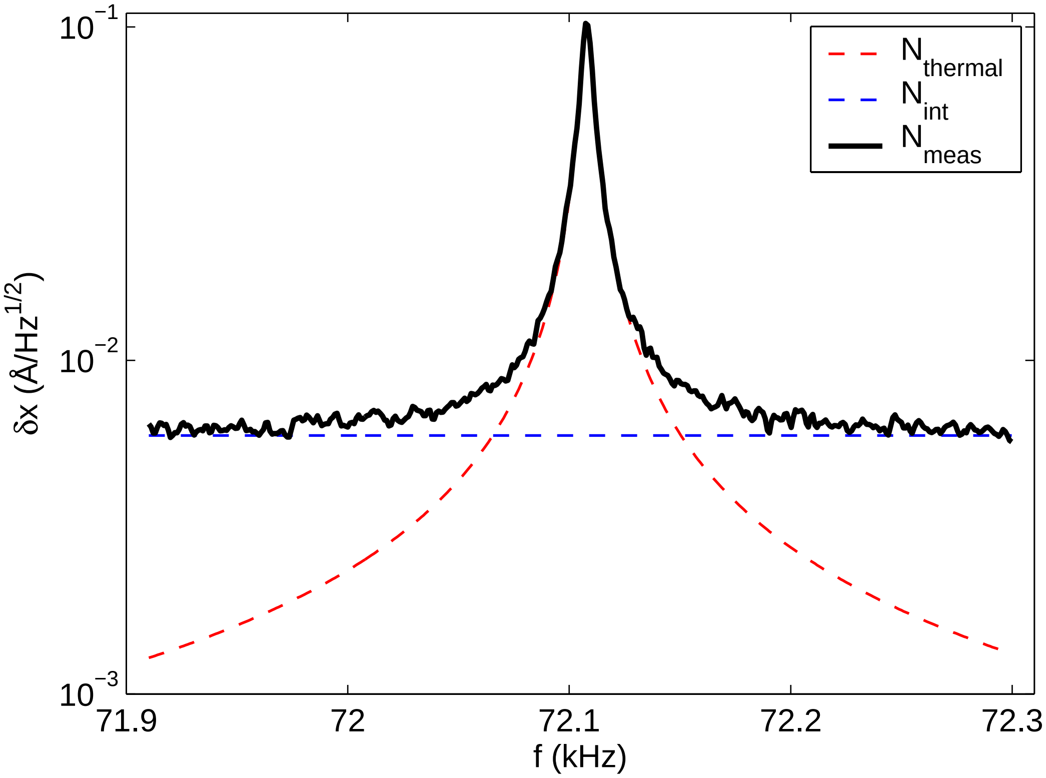

Figure 3-13: The spectrum of the cantilever deflection measurement. The measured deflection noise is due to thermal noise and interferometer noise. Near the cantilever resonant frequency, thermal noise dominates, and away from the resonant peak the white noise background due to the interferometer dominates.

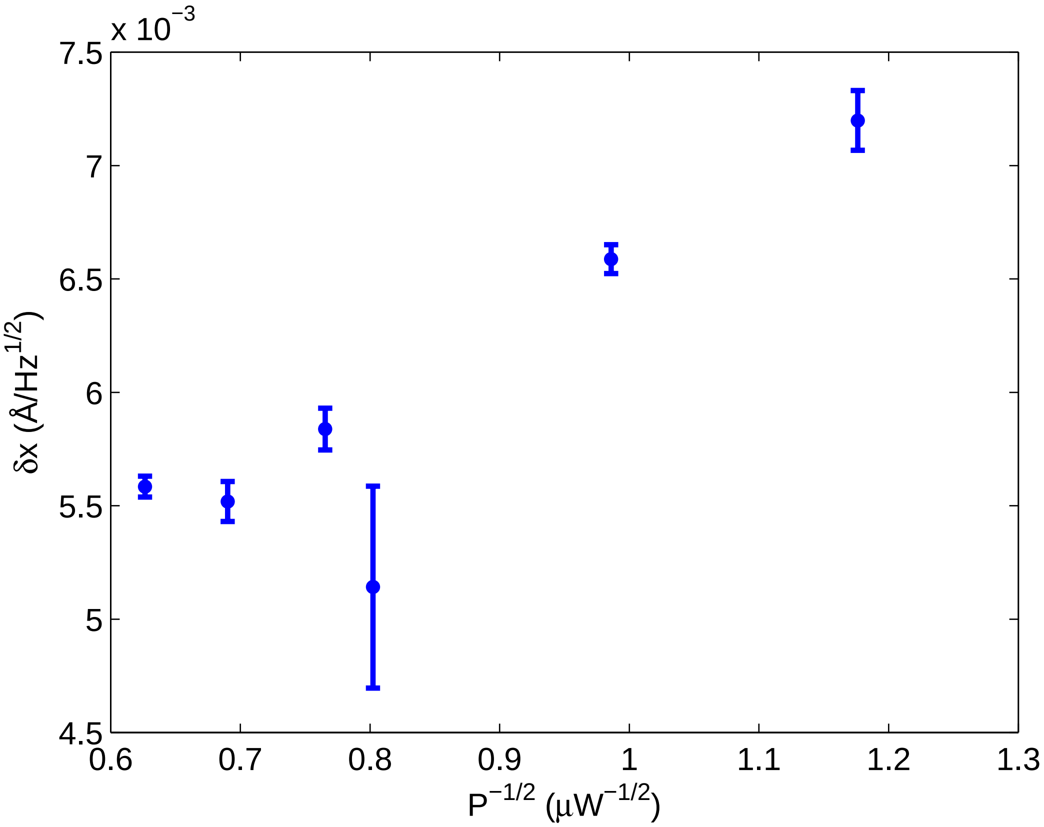

Figure 3-14: The interferometer-noise-limited deflection sensitivity as a function of the square root of the power incident on the photodetector. The deflection sensitivity improves roughly linearly with increasing $\sqrt{P}$, indicating that the interferometer noise is dominated by shot noise.

point this can damage the laser. Despite these cautions, it may very well be feasible to increase the laser power and improve the interferometer performance, as the laser power has never been optimized. In fact, for all of the data presented in this thesis except for the shot noise measurement of Figure 3-14, the interferometer arms were connected incorrectly. 90% of the laser power was sent to the cantilever, and 10% of the interfering reflections went to the photodetector. The laser has since been connected to the proper coupler arm, such that 10% of the light goes to the cantilever and 90% of the reflected light is transmitted to the photodetector. With the proper setup, it would then be possible to increase the laser power by a factor of 9 to match the power incident on the cantilever in the previous, incorrect setup, improving the SNR by a factor of 3. A new higher power laser diode would be needed to implement this.

Another option for improving the performance of the interferometer is to enhance the reflectivity of the optical fiber by adding a reflective coating onto the end (Mulhern et al. 1991; Mamin and Rugar 2001). This would increase the optical power in the interferometer without increasing the power incident on the cantilever. It may be difficult to implement, and if it was implemented an even greater degree of care in handling and aligning the fiber would be necessary, but it is certainly an option that deserves consideration.

One final note on the interferometer noise is that on occasion, a noise source other than shot noise dominates. The extra noise appears randomly, and can raise the noise level by an order of magnitude. Often, the noise level in this state fluctuates at a rate of about 1-2 Hz. I have found that making a slight adjustment to the laser current will eliminate the noise temporarily. Also, the noise will spontaneously disappear after a time on the order of a couple of hours. This extra noise source could be due to laser noise, or possibly to stray reflections in the system. One trick used to reduce the effect of stray reflections is to modulate the laser with an rf source (Albrecht et al. 1992). I have tried this technique, but have not found it to have a significant effect on the noise level. I have observed that the noisy state tends to occur more frequently after the laser has been turned on for some time (a week or more), which may indicate that it is more likely to be due to laser noise. Unfortunately, this noise can be a frustrating problem for which I do not know the solution. My best suggestion at the present time is to investigate a new laser diode for the interferometer.

3.4 FM Controller and Detector

In addition to the interferometer, the critical components of the cantilever measurement system are an FM controller and FM detector made by Nanosurf AG. The combination of the two instruments controls the frequency modulation detection. The cantilever vibration signal from the interferometer is used as the input signal. The FM detector measures the cantilever frequency using a phase lock loop (Dürig et al. 1997) by maintaining a 90º phase shift between the input and a reference. The reference frequency is provided by a voltage controlled oscillator (VCO), and is adjusted in a feedback loop to maintain this phase relationship. The voltage used to control the oscillator also serves as the frequency shift signal during a measurement. The reference is phase shifted by the FM controller to give a 90º phase shift between the cantilever drive voltage and the cantilever response, and is convolved with the output of an amplitude controller to drive the cantilever at a constant amplitude at its resonant frequency. The FM detector outputs two voltages corresponding to the cantilever frequency shift (one channel is intended for use in a feedback loop during constant frequency scanning, described in Section 3.7.1), and the FM controller outputs signals for the amplitude and dissipation (the dissipation voltage reflects the drive power needed to maintain the cantilever amplitude setpoint). During scanning, the frequency output is monitored. The drive voltage from the FM controller is applied to the sample holder to drive the cantilever capacitively. A DC voltage is added to the AC drive voltage to increase the capacitive force on the cantilever (Stowe 2000).

3.4.1 Noise levels

The system frequency noise level δf is due to the contributions from noise in the Nanosurf FM detector δf_{det}, cantilever thermal noise δf_{th}, and interferometer noise δf_{int}:

$$\delta f = \sqrt{\left(\delta f_{det}\right)^2 + \left(\delta f_{th}\right)^2 + \left(\delta f_{int}\right)^2} \qquad (3.17)$$

A measured noise spectrum is shown in Figure 3-15. I have also included a measured noise spectrum from the Nanosurf FM detector, and calculated the noise contributions due to thermal noise and interferometer noise based on a measurement of the deflection noise and using Equations (2.11) and (2.12). The y axis of the spectrum is the noise in the cantilever frequency shift Δf. This frequency shift is dependent on the force gradient at the cantilever, and is independent of scan rate. The x axis of the spectrum is the modulation frequency f_{mod}. This is essentially the frequency of the cantilever frequency shift. For example, consider a cantilever scanning over an array of magnetic bits with a regular spatial period L at a velocity v. The cantilever frequency shift will be modulated at a rate of $f_{mod} = v/L$. If the maximum frequency modulation is Δf, the cantilever frequency f is described by:

$$f = f_o + \Delta f \cos 2\pi f_{mod} t \qquad (3.18)$$

The frequency shift signal can be low pass filtered to reduce the noise. The cutoff frequency should be chosen to be higher than the characteristic f_{mod} for the image. I use a cutoff frequency that gives a time constant which is less than the time spent per pixel. For a 128 pixel line taken at a 0.5 Hz scan rate, the time per pixel is 8 ms. I typically use a low pass cutoff frequency of 100 Hz, which corresponds to a time constant of $\left(2\pi \cdot 100 Hz\right)^{-1} = 1.6 ms$.

For the relatively stiff, high frequency cantilevers used for the imaging in this thesis, noise for the frequency modulation detection is dominated by interferometer noise. Noise spectra from the easyPLL output were measured using several low-pass filter cutoffs, and are shown in Figure 3-16. The dominant interferometer noise generates a noise spectrum which increases with frequency, as opposed to thermally dominated frequency noise which is white. The result is that the noise increases as $BW^{3/2}$, and low pass filtering significantly improves the sensitivity of the frequency measurement. Averaging the voltage output corresponding to the frequency shift as described in the next section further improves the noise level. Using a 100 Hz low pass cutoff frequency, and

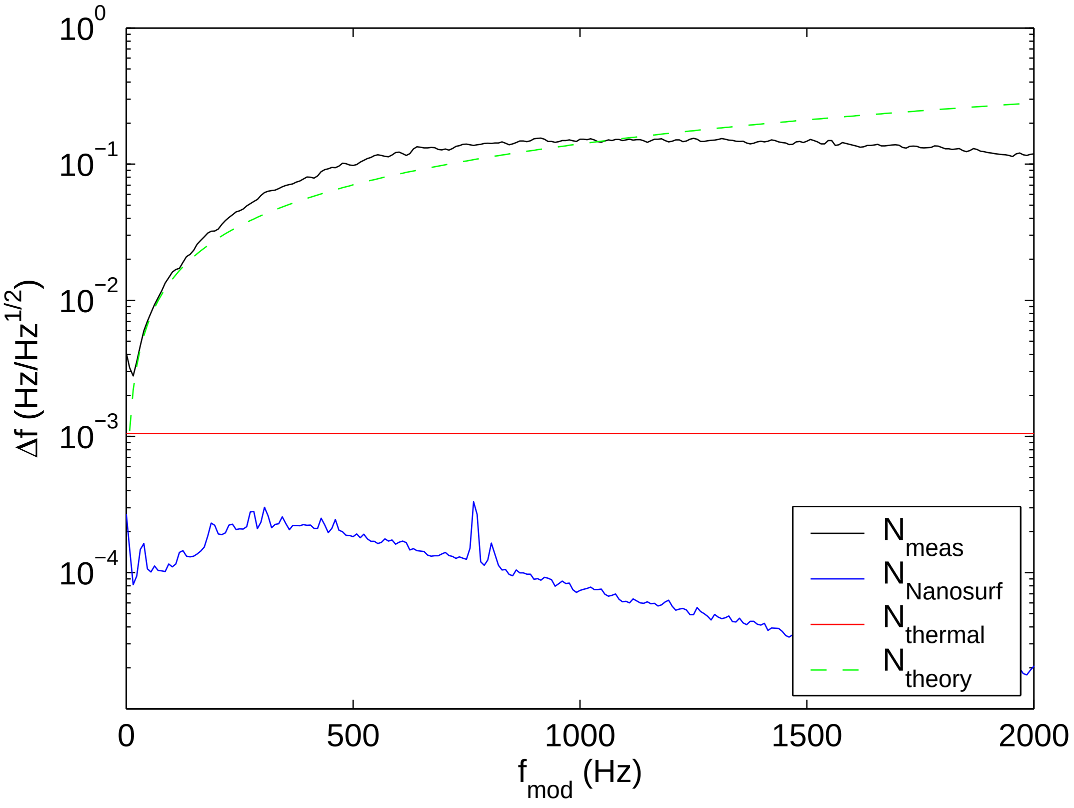

Figure 3-15: The noise level of the frequency shift measurement is due to noise from the frequency detector, thermal cantilever noise, and interferometer noise. The blue curve illustrates the measured noise level of the Nanosurf frequency detector, which is negligible. The red line shows the calculated frequency noise due to cantilever thermal noise, based on a cantilever with k=4 N/m, f_o=88 kHz and Q=31000, with an rms vibration amplitude A=10nm, and at a temperature of 295 K. The green curve shows the frequency noise level calculated from the measured interferometer noise level using Equation (2.12). The measured noise is dominated by the interferometer noise.

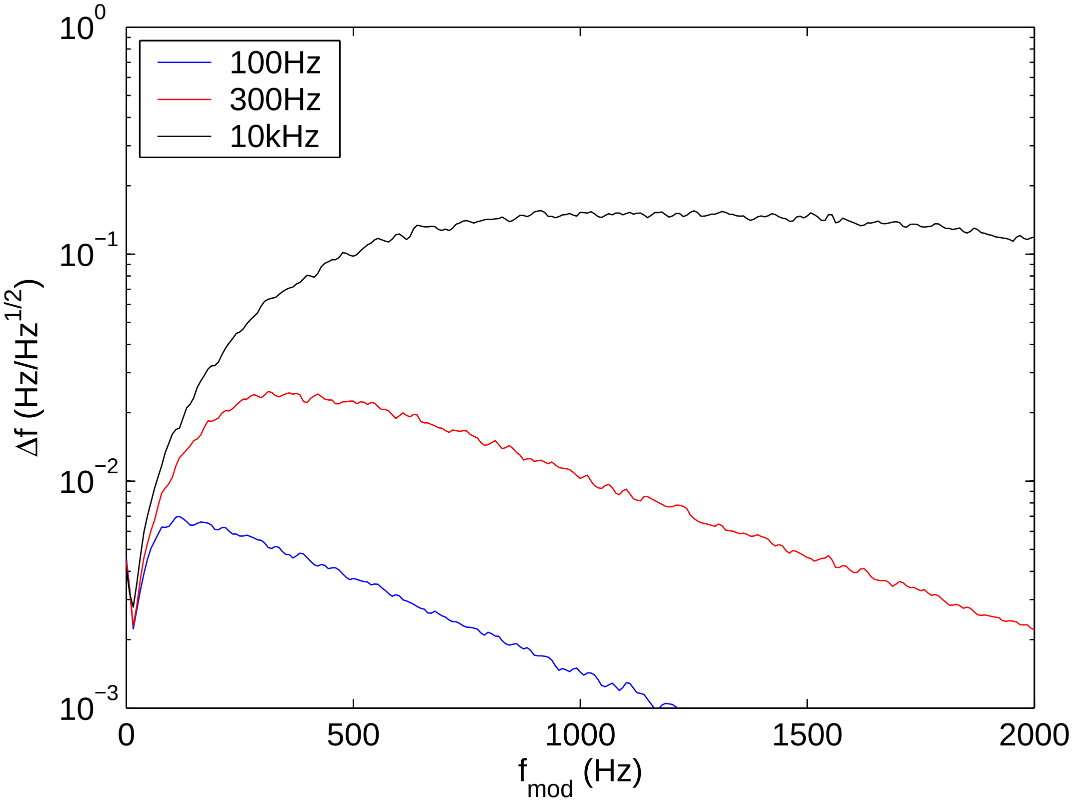

Figure 3-16: The noise level of the frequency measurement can be greatly reduced by low pass filtering the frequency shift signal. I use a low pass cutoff frequency of either 100 or 300 Hz during scanning.

averaging for 20 ms, I measured a frequency shift standard deviation of 1.2 mHz, corresponding to a force gradient sensitivity of 1.4 x 10^{-7} N/m.

With the force gradient sensitivity currently limited by interferometer noise, it would be well worth some time to investigate improvements to the interferometer as discussed in Section 3.3.1. It would also be worth reexamining the use of cantilevers with lower spring constants (<1 N/m). These cantilevers would have increased thermal noise compared to the ~5 N/m cantilevers I have primarily used, but which would also give a larger frequency shift for an equivalent force gradient. Also, the limits of high speed data acquisition and averaging along with low pass filtering could be further explored and pushed to improve the final sensitivity of the system.

3.5 Programming

The control software is written in MATLAB, using the data acquisition and instrument control packages. Most instruments are computer controlled using RS232 or GPIB, and a variety of useful programs for measuring cantilever properties (e.g. Q) have been written. However here it is only the scanning software which will be discussed as it is the most critical and most complicated. A particular emphasis was placed on scanning smoothly at high scan speeds.

A National Instruments PCI-6733 board is used for analog output, and an NI PCI-6120 simultaneous sampling board is used for the digital outputs and analog inputs. The clocks of the two boards are synchronized using the RTSI bus. With the boards synchronized, the input and output samples are directly related to one another, whereas when they are not synchronized errors result. This synchronization is critical for successful fast scanning, where the position and cantilever response must be directly correlated for imaging. A digital trigger is used to synchronously trigger the output and input boards.

The waveforms applied to the piezotube for scanning are shown in Figure 3-17. To minimize vibrations during a fast scan, the voltages are smoothed in software, avoiding quick direction changes and starts and stops which would excite higher frequency vibrations in the setup. The x waveform consists of a linear ramp, followed by one half period of a sine wave, and another linear ramp in the opposite direction. During this time, the y voltage is held constant. During the x direction change occurring after each pair of

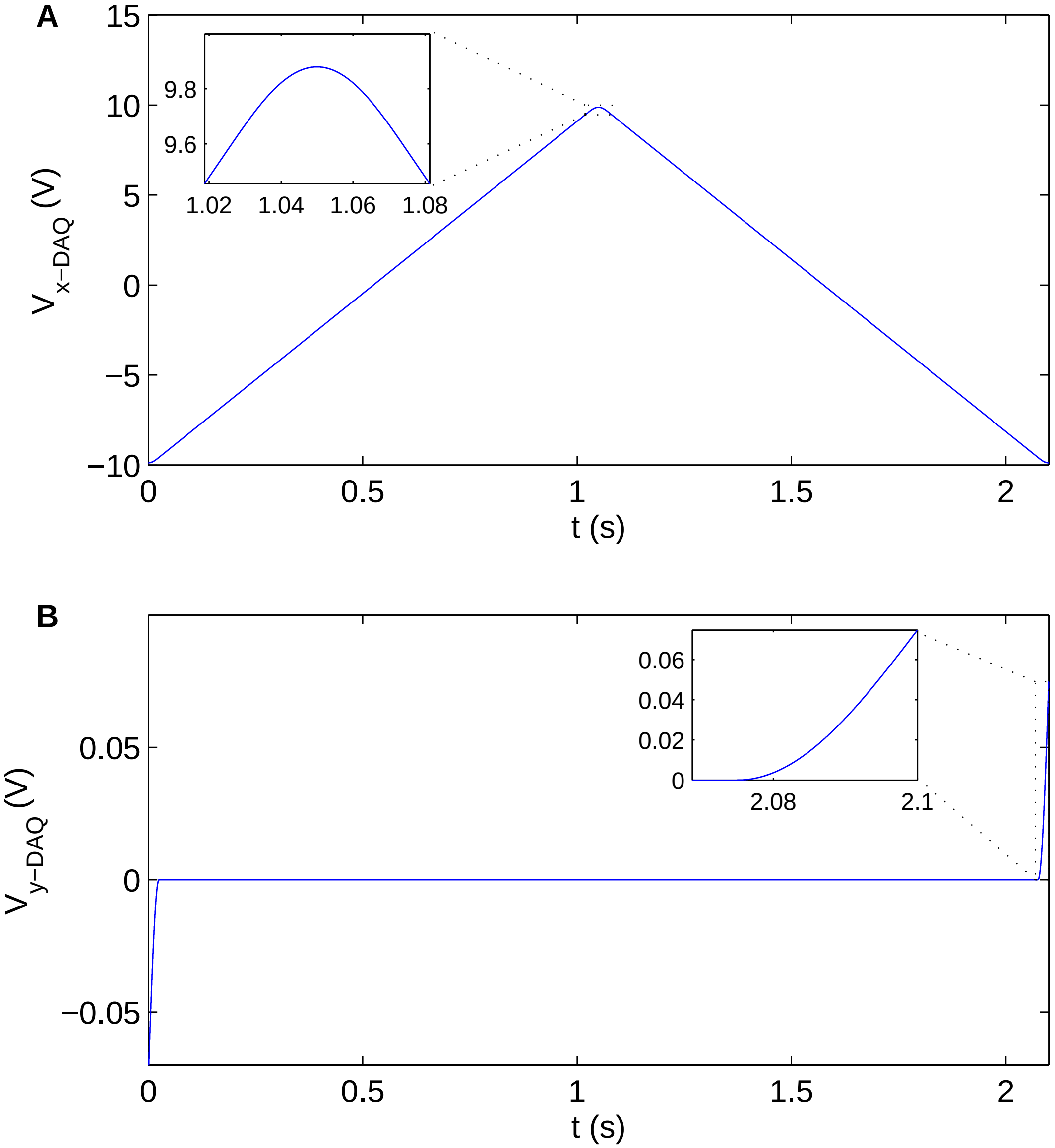

Figure 3-17: The waveforms applied to the x and y piezotube electrodes for scanning. (A) The x voltage is ramped up sinusoidally from zero velocity at the start of a line. At the end of the ramp, the voltage is increased linearly across t. At the end of the line, the voltage smoothly changes direction, and the linear ramp is repeated but in the opposite direction. The voltage then smoothly ramps down to zero velocity, after which the next scan line immediately begins. Data is acquired during the linear ramps, with one image acquired for each ramp direction. (B) The y voltage is maintained at a constant level during the data acquisition phase of a scan line. As a scan line ends and the next begins, the y voltage is smoothly ramped to position the piezotube at the new line. The ramp at the beginning is omitted for the first scan line, and the ramp at the end is omitted at the end of the scan.

linear ramps, the y voltage is smoothly incremented with a half period sinusoid transition. Image data is taken only during the linear parts of the scan motion, and the rounded turning points are ignored and treated as dead time for the imaging. This does reduce the useful scan range slightly, with an effective DAQ output range of about 19 V instead of the full 20 V available. The output board is sampled at a rate of 160 kS/s (kilo-samples per second), and a typical scan rate is 0.5-1 Hz. The nominal voltage change between samples is then 59-119 μV/S, while the 16-bit analog output board has a resolution of 305 μV/S. This resolution results in a step frequency of about 65 kHz for a scan covering 20V in 1s. This is sufficiently high that it is filtered by the low pass filters described in Section 3.6. Additionally, the size of the steps is small such that I believe that the digitization is not a significant source of vibrations. The fact that the board resolution is less than the nominal output voltage means that there is some irregularity in the actual output voltage, depending on the specific sample at which the output board switches. This also should be insignificant, again due to the small step sizes and the filtering at the high frequencies at which they occur. The voltage applied to the center electrode of the piezotube (the z voltage) is described in Section 3.7.

The analog input board is operated at its maximum rate of 800 kS/s, such that 5 input samples are measured per output sample. As a simultaneous sampling board, four channels can be measured at the maximum rate without any errors due to switching between channels. The fast sample rate allows for a great deal of averaging, which reduces the noise and improves the quality of the images obtained. I typically image at a rate of about 0.5 Hz, such that for a 128 pixel image, 6250 samples are averaged for each pixel.

To facilitate fast scanning, the following algorithm is used. First, the piezotube is moved to the start position, which is the nearest corner on the left side of the image from the current position. To start the scan, a full line of x, y, and in the case of constant height scanning, z voltages, is sent from the computer to the DAQ board. A digital trigger starts both the analog output channels and the input channels. A second line is then sent to the board. Once the first output line is completed, the first input line is read from the DAQ, and the third output line is sent to the DAQ. The reading of the analog inputs always lags the sending of outputs by one line in order to maintain output data in the DAQ buffer such that undesirable stops and other blips are avoided between scan lines. The DAQ board does synchronize the actual inputs and outputs so that they are directly correlated. For a typical rate of 0.5 Hz, a typical line involves 1.6 MS on each of two input channels, plus 320 kS on each of 3 output channels. The demands on the computer are high, and it does crash if any attempts are made to multitask during a scan, but the ability to do such fast scanning and so much averaging is quite powerful.

3.6 Scan Electronics

The scan electronics are illustrated in Figure 3-18. x, y, and z scan voltages are generated by the analog output boards as described in the preceding section. Next, the voltages go through a potentiometer box which allows the voltages to be smoothly ramped down to 0 V in the event of a computer crash or a similar event, a safety feature that has been used in another low temperature force microscope (Topinka 2002). A homemade instrument was constructed to take the x and y voltages and generate ±x and ±y voltages, and to add a manual offset to the z voltage.

The outputs from the instrument are input into an RHK HVA 900 high voltage amplifier. The ±x, ±y, and z voltages are amplified by a factor of 45, and the outputs are then connected to a feedthrough on the microscope through a breakout box. The breakout box contains 2 MΩ resistors which can be used to “short” the piezotube to the microscope ground to eliminate any built-up charge, and low pass filters with a cutoff frequency of 250 Hz. The filters have been found to be absolutely essential for operation of the microscope. Without them, a large amount of noise is added to the cantilever resonance. This may be due to high frequency noise on the scan voltages causing the piezotube to vibrate the entire microscope head, which is amplified by the cantilever resonance, or due to a ground loop. Cantilever noise spectra with and without the filters in place are shown in Figure 3-19. The presence of these filters may eliminate the need for the software-smoothed scan voltages described in Section 3.5, but since the programming preceeded the addition of the filters the smoothed scan voltages have remained in use.

Another instrument constructed for this microscope is a proportional-integral (PI) controller, used for doing constant frequency (constant force gradient) scanning. The

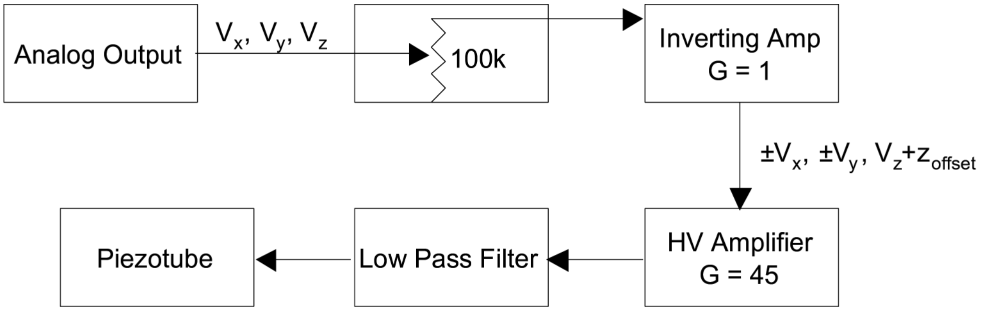

Figure 3-18: The electronics for positioning the piezotube. X and y scan voltages are generated by an analog output board. The z voltage is generated by the AO board for constant height scanning, or a PI controller for constant frequency scanning. A 100kΩ potentiometer allows me to reduce the voltage to the amplifier to zero in the event of a software crash, which prevents instantaneously changing the piezo voltage from 450 V to zero. A set of inverting amplifiers copies and inverts the x and y voltages and adds a manual offset to the z voltage, and sends 5 voltages to the high voltage amplifier. The high voltage amplifier output is connected to the piezotube via a set of 5 low pass filters.

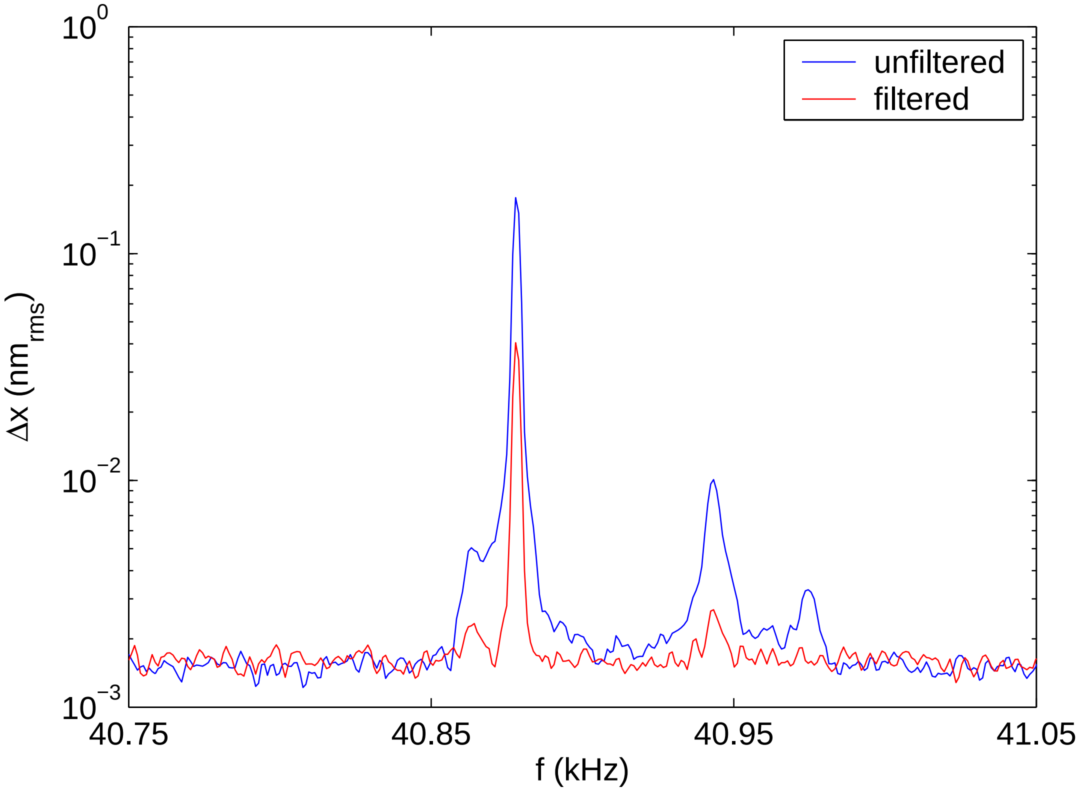

Figure 3-19: The deflection spectrum of a cantilever with and without filtered scan voltages. The blue curve illustrates the cantilever noise when the high voltage amplifier was connected directly to the system. Adding low pass filters after the amplifier output greatly improves the noise level, as shown by the red curve. This noise may be due to amplifier noise coupling to the cantilever, or it could perhaps also be due to a ground loop created when the amplifier is connected to the microscope.

“Output” voltage from the easyPLL FM Detector is amplified and low-pass filtered and connected to the PI controller input. The controller then generates a z voltage in order to maintain a zero input voltage, thus maintaining a constant frequency.

3.7 Imaging

Magnetic imaging can be done in either of two modes, constant frequency/force gradient mode or constant height mode. The constant frequency mode is simple to set up and is good for doing quick scans, particularly at the start of an experiment when one is trying to get a feel for the cantilever and sample. Constant height mode is preferable for imaging from which any quantitative information is desired, and for imaging in which it is necessary to have a controlled force on the sample. This mode has been most commonly used for this thesis, and has generally been found to produce superior images, in the case of imaging superconducting vortices.

This microscope can also be operated as a non-contact atomic force microscope when desired. To measure an atomic force instead of the magnetic force, standard AFM cantilevers can be used, without a magnetic film on the tip. Alternatively, the tip-sample separation can be decreased to the point at which the atomic force dominate over the magnetic forces. The constant frequency mode of operation is best used for AFM imaging. Also, stiff cantilevers should be used in order to obtain a small tip-sample separation without inducing snap-in of the cantilever to the surface. To date, the AFM mode has only been used to determine the plane of the sample, and an attempt at imaging with high resolution was not terribly successful. It is likely that low pass filtering of the PI controller output (V_z) and the use of stiffer cantilevers (>50 N/m) would improve the results.

3.7.1 Constant Frequency Imaging

The electronics for the constant frequency mode of imaging are illustrated in Figure 3-20. A proportional-integral (PI) controller is used to control the piezotube z voltage and maintain a constant frequency shift. A DC voltage is applied to the sample holder to generate an electrostatic force gradient. This combines with the magnetic force gradient to create a monotonic interaction between the sample and cantilever, which is important

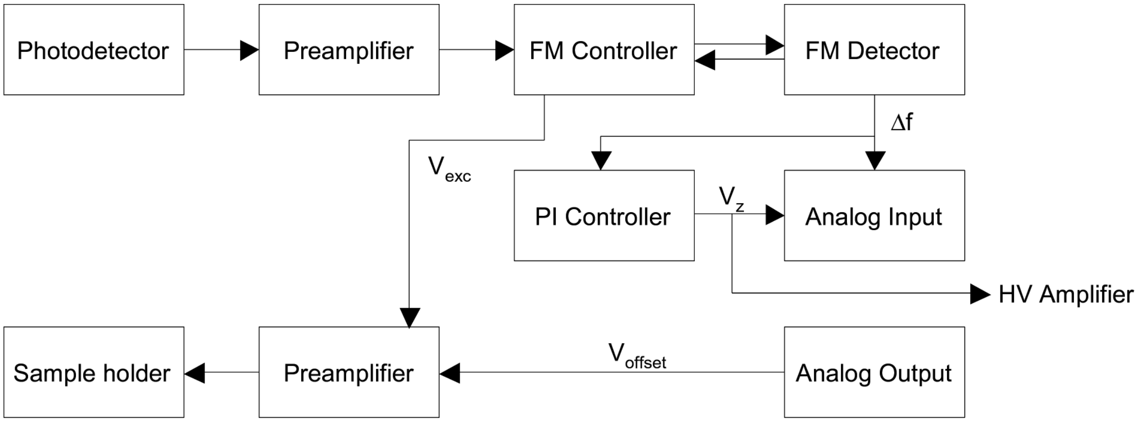

Figure 3-20: The electronics for constant frequency scanning. An FM controller and FM detector made by Nanosurf drive the cantilever using the frequency modulation method. The drive voltage is summed with a DC offset and applied to the sample holder to drive the cantilever capacitively. A PI controller feeds back on the frequency shift signal and adjusts the cantilever-sample separation to maintain a frequency shift of zero.

for scanning with z feedback (Grütter et al. 1995). The feedback gains are increased to a point at which the frequency is held constant, but V_z does not oscillate. The PI output (i.e. V_z) is the primary signal for the scan, and the frequency shift is also measured as an error signal. Generally there is a slope to the sample surface which dominates the raw data. The data can be fit with a quadratic equation to determine the coefficients c_i describing the location of the sample surface:

$$V_z = \begin{bmatrix} V_x & V_x^2 & V_y & V_y^2 & 1 \end{bmatrix} \begin{bmatrix} c_{V_x} \\ c_{V_x^2} \\ c_{V_y} \\ c_{V_y^2} \\ c_1 \end{bmatrix} \tag{3.19}$$

These coefficients are used for determining the z voltage for scanning at a constant height above the sample surface. Typically the quadratic terms are small. Coefficients are determined for the forward and reverse scan directions, and for both slow scan directions. Generally they are sufficiently similar that one set of coefficients may be used for all directions during constant height scanning.

The quality of the AFM images is not great, and it is the electrostatic force which dominates images taken in this way, but it is sufficient for determining the coefficients of the sample plane. Currently the PI output is not low-pass filtered, it is likely that simple filtering would dramatically improve the quality of future AFM imaging.

Typically the non-contact AFM mode is used for the first scans at the start of an experiment. When imaging a superconductor, the sample is heated above T_c to eliminate magnetic signals. A DC voltage in the range of 0.25-2 V is applied to the sample, and a set of four AFM images are taken, one immediately following the next. The first two images are used to reduce the effects of piezo creep and are discarded, and the following two scans are used to determine the plane coefficients for use when operating in the constant height imaging mode. The values for c_{V_x} and c_{V_y} can be fairly large, up to about 0.3. This indicates that the sample is quite sloped relative to the plane of the piezotube scan. This has not been a major problem to date, but it would certainly be desirable to reduce that slope if it were feasible. The values for $c_{V_x^2}$ and $c_{V_y^2}$ are generally small, around 0.0001, indicating that the sample surface is actually quite well described by a flat plane. c_1 is the offset on the z voltage.

For initial testing of the microscope, a 100 MB Zip disk was used. Data was first written to the disk to the point at which it was full, and subsequently a small piece of the magnetic media was cut out and mounted in the microscope. Constant frequency images of the disk taken at 295 K and at 5 K are shown in Figure 3-21. The scale bar may be off by a factor of 2 for the x direction. It was later discovered that one high voltage channel was broken, however it is not known whether the malfunction occurred before or after imaging the Zip disk.

3.7.2 Constant Height Imaging

The electronics for imaging in constant height mode are illustrated in Figure 3-22. After determining the coefficients for the plane of the sample from a set of constant frequency NC-AFM mode scans, magnetic images may be obtained in the constant height mode. For each x and y voltage during a scan, a corresponding z voltage is calculated and output to the piezotube from the DAQ, such that the cantilever tip moves in a plane parallel to the sample surface. The frequency shift is measured and used as the image signal. The dissipation signal is also commonly measured, although to date dissipation images have all been too noisy to obtain any useful information from them. Low-pass filtering of the dissipation signal would improve the results, but it is likely that there is not much to observe.

After withdrawing and reapproaching the cantilever to the sample using the coarse approach mechanism, the coefficients remain the same, except for the c_{z_o} term. This coefficient must be reset by finding the surface position. This can be accomplished by measuring the cantilever deflection as the piezotube is extended, with a bend in the curve indicating snap-in of the tip to the sample. However, I generally prefer to determine the z position by measuring Δf vs z, as shown in Figure 3-11. When Δf exceeds a setpoint, typically around 40 Hz, I consider that value of z to be the surface level. Repeating the surface finding procedure does not always return the same result, due to drift and

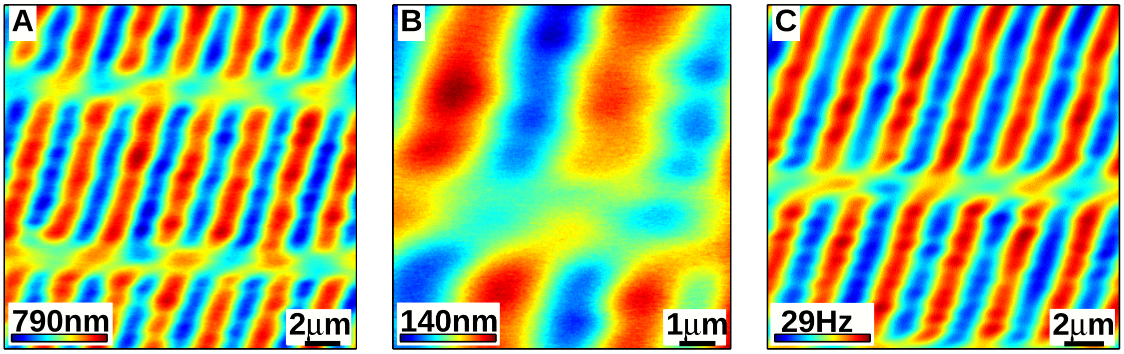

Figure 3-21: Initial testing of the magnetic force microscope was done by imaging a 100 MB Zip disk. (A) Bits are clearly visible in a constant frequency scan obtained at 295 K. (B) I also successfully imaged bits at 5 K, again using the constant frequency mode. (C) An image of the Zip disk taken using the constant height imaging mode at 295 K further demonstrates the capabilities of the microscope.

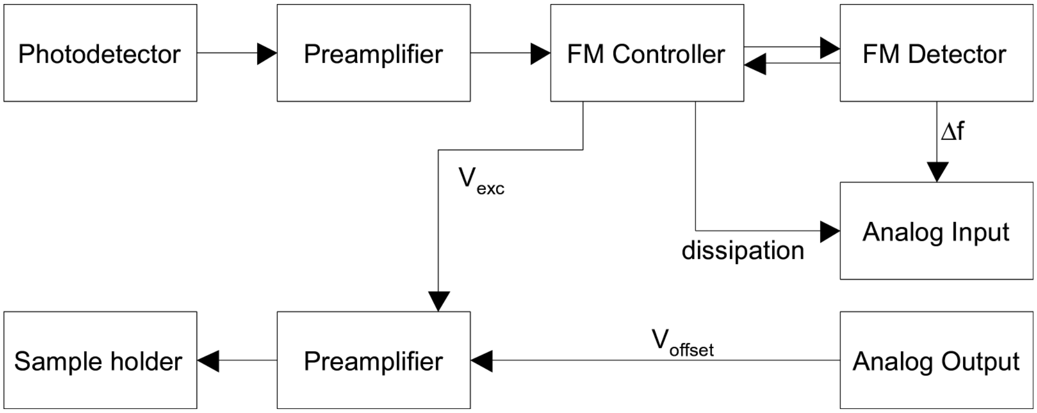

Figure 3-22: The electronics for constant height scanning. An FM controller and FM detector made by Nanosurf drive the cantilever using the frequency modulation method. The drive voltage is summed with a DC offset and applied to the sample holder to drive the cantilever capacitively. The frequency shift is directly measured as the imaging signal. The cantilever dissipation can also be measured in this mode.

piezotube creep. A thorough procedure for minimizing inconsistencies was never developed, although I did find that starting the measurement after sitting briefly at a V_z value that was not too far from the surface helped. I also found that using a slow ramp rate (about 0.25 V_{DAQ}/s) on the piezotube V_z results in more consistent results. The error is typically on the order of 10 nm. I did not thoroughly investigate these effects however, and there is certainly an opportunity for improvement here.

The Zip disk sample was also used to test the microscope in constant height mode. An image of the disk taken at 295 K using the constant height mode is shown in Figure 3-21C.

3.8 Scan Calibration

The piezotube used for the experiments in this thesis was calibrated in the x and y directions using a grid of posts with a 700 nm pitch, fabricated by Advanced Surface Microscopy. Images (shown in Figure 3-23) were obtained at 300 K, 78 K, and 5K using the non-contact AFM mode. A DC voltage of 2 V was applied to the sample. A plane of the form given by Equation (3.19) was then subtracted from the data. The calibration coefficients for x and y were determined by measuring the voltages corresponding to the centers of posts on opposite side of the image (between which there is a known distance given by the number of posts times the pitch), accounting for the angle between the grid and the scan directions. The calibration coefficients are listed in Table 3-1. One point to note is that the calibration values are higher at 78 K than at 295 K. This is a bit surprising since typically less motion of the piezoelectric material occurs at a given voltage as temperature decreases. However, the material chosen for the piezos is EBL #4 from Staveley Sensors, which has reduced temperature dependence at the expense of having reduced motion at room temperature (it is similar to other piezoelectric materials at 4 K).

The z calibration was determined at 5 K using the fiber interferometer directly. In this case, the interference signal was created by the reflection from the fiber end, and the reflection from the sample surface, in this case a Nb thin film. The interferometer voltage was measured while ramping the z voltage, as shown in Figure 3-24. By fitting the data with a sine wave, the piezotube calibration coefficient for the z direction was determined to be 58 nm/$V_{z\text{-}DAQ}$. The z calibration was not measured at any other temperatures. I

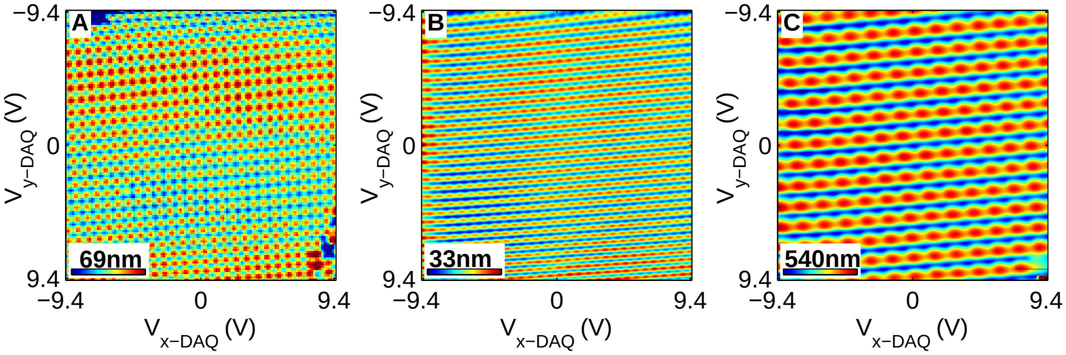

Figure 3-23: The piezotube was calibrated in the x and y directions by imaging a 700 nm pitch grid using the constant frequency method. A 2 V DC voltage was applied to the sample surface, providing the contrast in the images. (A) Calibration values of $0.99\,\mu m/V_{x-DAQ}$ and $0.97\,\mu m/V_{y-DAQ}$ were measured at 295 K. (B) At 78 K, the calibration values were $1.02\,\mu m/V_{x-DAQ}$ and $1.13\,\mu m/V_{y-DAQ}$ (C). The calibration values were measured to be $0.47\,\mu m/V_{x-DAQ}$ and $0.48\,\mu m/V_{y-DAQ}$ at 5 K.

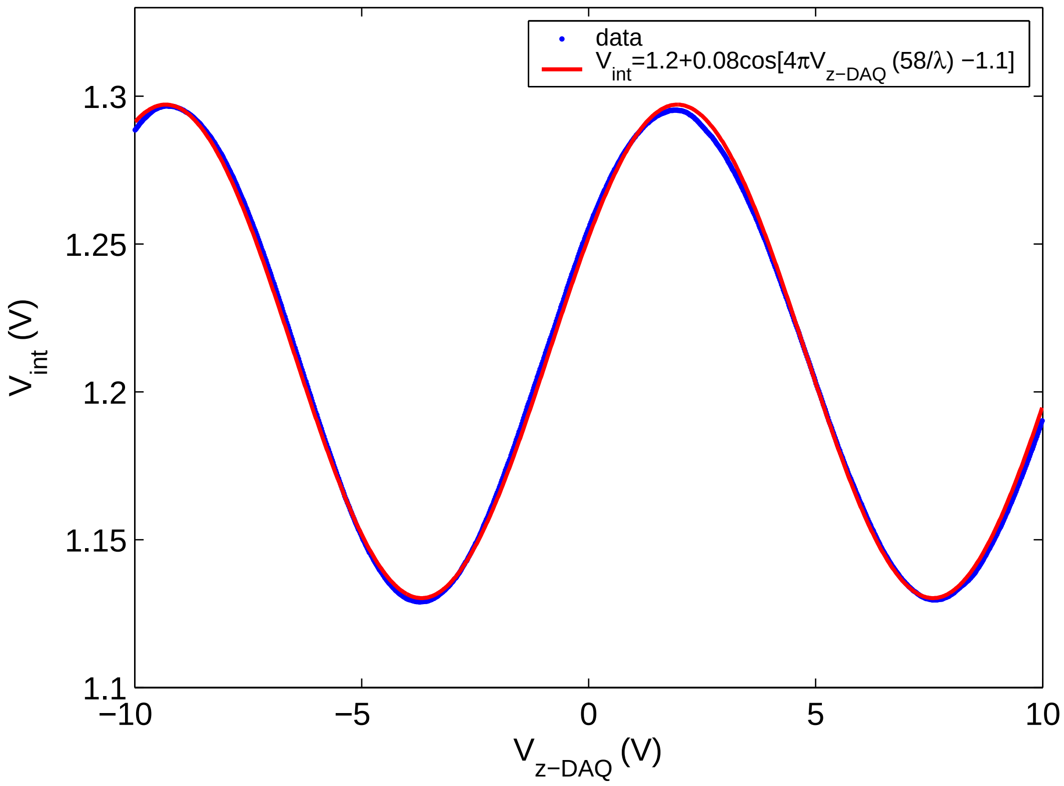

Figure 3-24: The piezotube was calibrated in the z direction using the fiber interferometer. The reflections giving the interference are from the cleaved fiber end and from a shiny Nb sample mounted on the piezotube. A fit to the data gives a calibration value of $58\,nm/V_{z-DAQ}$.

estimated the z calibration values at 79 and 295 K by scaling the 5 K value by the average of the ratios between the x and y calibration values at the respective temperatures. The estimated values are listed in Table 3-1.

Table 3-1: Calibration values for the piezotube at various temperatures

$T(K)$	$cal_x \left(\mu m / V_{x-DAQ}\right)$	$cal_y \left(\mu m / V_{y-DAQ}\right)$	$cal_z \left(nm / V_{z-DAQ}\right)$
295	0.99	0.97	120
78	1.02	1.13	131
5	0.47	0.48	58

3.8.1 Piezotube hysteresis and creep

It is important to be aware of the effects of piezotube hysteresis and creep when imaging. The hysteresis effect is illustrated in Figure 3-25. When making direct, pixel to pixel comparisons between images, one should always compare images that were taken in the same fast and slow scan directions.

Piezo creep occurs when a voltage is applied to the piezotube for a length of time. To minimize its effects, images were obtained using a set of scans. One scan immediately follows the next such that the piezotube does not rest at a particular voltage and creep does not have sufficient time to occur. The first one or two scans, which exhibit the effects of creep, are discarded, and the following scans are used as the images.

3.9 Possible Improvements

The magnetic force microscope generally functions quite well, but of course there are a number of ways in which it might be improved. A list of items which could/should be developed are the coarse approach, vibration isolation, interferometer performance, cantilevers, temperature sensor setup, and the general wiring setup.

The coarse approach mechanism has been the greatest source of grief in operating the microscope thus far. The fine pitch screw has seized on a number of occasions, which has been a major problem. Even when it does not seize however, it is still not an ideal mechanism for the coarse approach. One issue is that as the screw is turned, the cantilever-sample angle changes. Another is that vibrations can be coupled from the

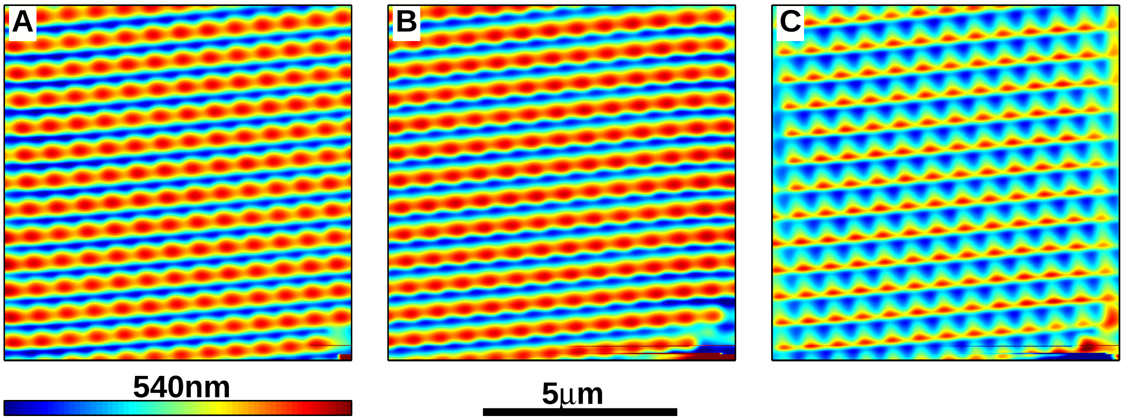

Figure 3-25: The piezotube exhibits hysteresis during scanning. The calibration grid was imaged at 5 K using the constant frequency method. Data is collected for both the (A) forward and (B) reverse directions of a scan line. (C) A pixel-by-pixel subtraction of image B from image A illustrates the hysteresis in the piezotube.

stepper motor rod to the microscope head, and in general the assembly is not as stiff and resistant to vibrations as other coarse approach setups. It would be preferable to construct a piezo stick-slip coarse approach mechanism such as the Pan-design (Pan et al. 1999), or to incorporate a commercial apparatus from Attocube. The Attocube setup would also allow for coarse x and y positioning, which would be a very powerful addition to the microscope and could open up a wide range of new experimental possibilities.

With a new coarse motion device in place, the options for vibration isolation for the microscope head open up dramatically. It is likely that a set of very flexible springs would provide better isolation than the current bellows setup. Currently this cannot be implemented because of the need for a rod to couple the stepper motor to the coarse approach screw, however with a piezoelectric stick-slip mechanism this would no longer be necessary and a spring-based isolation system would become feasible. It is likely necessary to consider the damping of a spring-based system before implementing any such design.

The frequency noise of the microscope is currently dominated by interferometer noise, thus some effort could be made to improve the interferometer performance. The most simple change to make is to optimize the laser power. In the shot noise limit, the SNR goes as $\sqrt{P}$. However, increased power leads to cantilever heating and optical feedback. It is possible that using a shorter wavelength laser would improve the noise level because of the higher fringe slope. However, shorter wavelengths are more easily absorbed by silicon cantilevers. It may be worth considering the use of silicon nitride cantilevers. These have much lower Q's than silicon levers, but this may not affect the frequency noise in the regime where interferometer noise dominates. Another possible improvement is to increase the reflectivity of the fiber end by coating it with Si with a thickness maximizing constructive interference of the fiber reflection. This would be expected to have the most dramatic effect on the interferometer performance, however it is also the most difficult to implement, particularly if damage occurs to the fiber end on a regular basis.

One aspect of the microscope which could definitely be improved is the location of the temperature sensor. Currently the sensor is mounted on the copper block containing the heater on the microscope head, with the sample and cantilever connected to this block by copper braids. It would be preferable to mount a second temperature sensor directly on the sample holder to obtain a more accurate measurement of the sample temperature. The Lake Shore Cryotronics 340 Temperature Controller does allow for monitoring two sensors simultaneously.

A final item for improvement is the general wiring of the microscope, and in particular the connectors used. I have never been all that happy with the current connectors in the microscope. Also, the heat sinking of wires is done in somewhat of a messy and disorganized fashion. I have found the preferred connectors to be the SIP style connectors, such as the Samtec connectors used to connect the wires for the scan piezotube. These could be used for all of the connections. Even better would be to use pin and socket connectors mounted into homemade Macor blocks, making a reasonably small but robust connector assembly. This does of course require more work in the initial design and assembly process, but it may be worth it in the long run.

This page intentionally left blank.

Chapter 4 : Magnetometry of Cobalt Nanomagnets

Nanomagnets are interesting materials for study because of their potential applications in areas such as high density storage media, spin electronics, and basic physics experiments such as macroscopic quantum tunneling and nanomagnetism studies. Chemical methods have shown promise for producing uniform, high quality nanomagnets (Sun and Murray 1999; Sun et al. 2000). The Bawendi lab at MIT has produced cobalt nanomagnets with size distributions as small as 6 % (Dinega 2001). Nanomagnets such as these could potentially make good MFM tips, as their small size means that they could provide high spatial resolution.

Many groups have made steps to improve the resolution of MFM cantilevers, by evaporating thin magnetic films onto sharp tips made using an electron beam (Ruhrig et al. 1996; Skidmore and Dahlberg 1997), or modified tips using a focused ion beam (Folks et al. 2000; Philips et al. 2002). Magnetic films have also been evaporated onto in-plane tips (van den Bos et al. 2002). At the time this work using nanomagnets began, the idea of using a nanomagnet for the magnetic material as opposed to a thin film was to my knowledge a novel one. Since then however, magnetic Ni particles have been grown on the end of nanotubes on cantilevers using a CVD process (Arie et al. 2000) for use as MFM tips. Nonetheless, the greater uniformity of the MIT nanomagnets could be advantageous for making quantitative MFM measurements, as it could be possible to calibrate the nanomagnets and model the signals from cantilever-nanomagnet setups. The small moment of the nanomagnets could also be an advantage, because it would exert less force on the sample under study and would thus be a less intrusive measurement device. With this small moment there would be a correspondingly small measurement signal, however, and a sensitive cantilever would be necessary in order to detect the small signals that would be generated.

To evaluate the potential of these nanomagnets for use as MFM tips, I set out to characterize their magnetic properties using the technique of cantilever magnetometry. This technique was chosen both because the end application would involve measurements with nanomagnets on cantilevers, and also because the cantilever technique is capable of sensitive magnetic moment measurements. In this chapter, I discuss studies of chemically synthesized cobalt nanomagnets from the Bawendi lab. This chapter is not intended as a thorough study of nanomagnet properties, but rather as a brief overview of the research that was carried out in the early days of my career as a graduate student. It is primarily intended to serve as a demonstration of the potential of the cantilever magnetometry technique, as well as a record of the nanomagnet work that was done.

4.1 Attaching Nanomagnets to Cantilevers

Silicon nitride cantilevers (Figure 4-1) fabricated in the Stanford Nanofabrication Facility (Yasumura 2000) were used for the measurements in this chapter. Cobalt nanomagnets with a diameter of 9 nm were produced at MIT, and were suspended in hexane. I diluted this suspension with additional hexane to reduce the density of Co particles, and proceeded to attach the particles to cantilevers using one of two methods.

The first method for attaching nanomagnets to cantilevers was to use a microdroplet ejection apparatus (Loomba et al. 2000) to place droplets of the suspension on the end of a cantilever beam. A steady stream of microdroplets of the hexane suspension was ejected from the pipette. The cantilever end was moved through this stream such that several droplets struck the cantilever. Upon evaporation of the hexane solvent, nanomagnets were left attached to the cantilever. An SEM image of a cantilever prepared in this fashion is shown in Figure 4-2. It appears that the nanomagnets have collected in a corner of the cantilever beam, likely drawn to the edge by meniscus forces as the hexane evaporated.

The second method for attaching nanomagnets was much more simple than the first. 5000 Å and 7000 Å thick Si_3N_4 cantilevers were dipped into a diluted suspension of 9 nm Co nanocrystals in hexane for ~1 s, following which the hexane was allowed to evaporate leaving the nanoparticles adhered to the cantilever surface. An SEM image (Figure 4-3) of a 7000 Å thick cantilever shows a reasonably good distribution of particles, with mostly individual particles scattered over the surface along with some clumps of ~2-5 particles. Attempts were made to obtain measurements using this cantilever in the magnetometry setup, but unexpected problems with noise and drift, possibly due to the fact that these cantilevers were not overhanging (i.e. there was a Si background behind

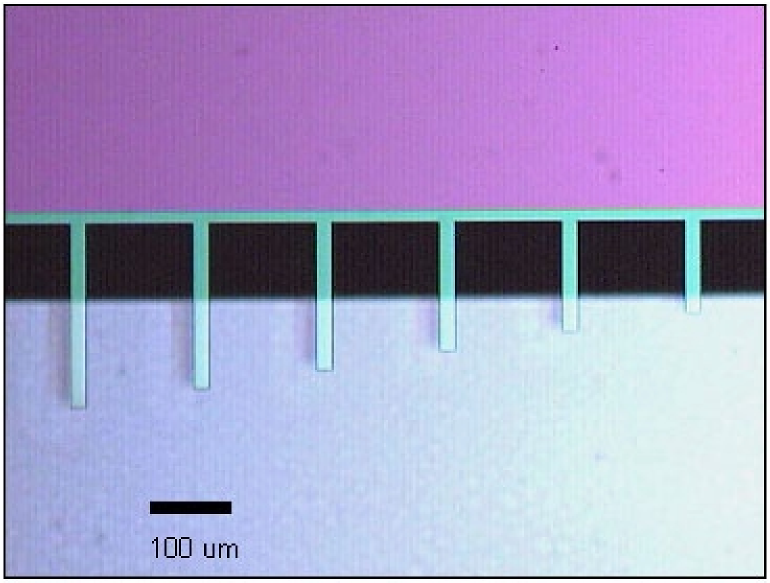

Figure 4-1: An optical microscope image of the silicon nitride cantilevers used for the magnetometry measurements on cobalt nanomagnets. The cantilevers are rectangular beams without the sharp tips characteristic of AFM or MFM cantilevers.

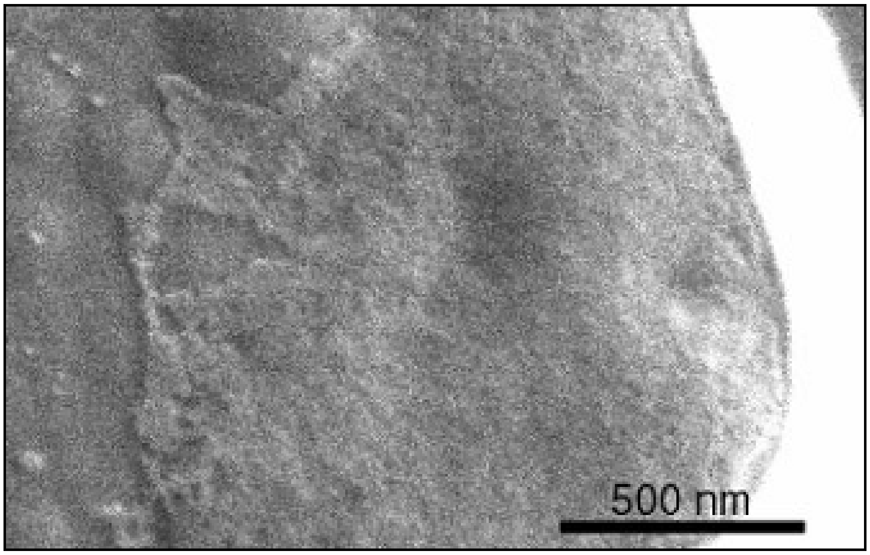

Figure 4-2: An SEM image of cobalt nanomagnets on the surface of a silicon nitride cantilever, at a corner at the end of the cantilever beam. This nanomagnet-cantilever sample was prepared by ejected a dilute suspension of nanomagnets in hexane from a microdropper such that some of the drops landed on the cantilever, leaving nanomagnets attached to the lever surface upon evaporation of the hexane. The nanomagnets appear to have collected in a corner of the cantilever, such that measurements of these nanomagnets are highly dependent upon interactions between nanomagnets rather than only the intrinsic properties of the individual nanomagnets themselves.

Figure 4-3: An SEM image of cobalt nanomagnets on the surface of a 7000 Å thick silicon nitride cantilever, at a corner at the end of the cantilever beam. The large circular objects in the image are bumps in the surface of the cantilever, and the small white dots are the cobalt nanomagnets. This nanomagnet-cantilever sample was prepared by dipping the cantilever in a dilute suspension of nanomagnets in hexane. Magnetometry measurements shown in this chapter were taken using a cantilever prepared with this method.

the cantilevers, affecting the reflected signal in the interferometer), prevented the acquisition of any useful data. Later samples were prepared in a similar fashion, although no SEM images were taken. More particle clumping is expected to have occurred, as the Co particles were adhered to the cantilevers about 7 weeks after they were fabricated. "Old" particles were used as this was expected to be a test run to confirm a hypothesis about the observed noise and drift. The noise and drift was better than any levels previously obtained however, and as such some time was taken to take a more extensive data set than originally planned. The measurements presented in the following sections were all obtained using a 240 μm x 25 μm x 5000 Å Si_3N_4 cantilever coated with nanomagnets attached using this dipping technique.

4.2 The Measurement System

Cantilever magnetometry measurements were made in collaboration with John Chiaverini and Aharon Kapitulnik, using their cantilever system (Chiaverini et al. 2001). This system operates using the same principle as the magnetic force microscope described earlier, although the details of the electronics differ. A homemade "self-oscillation circuit" (Yasumura 2000) was used to control the cantilever vibration, and a Stanford Research Systems frequency counter was used to measure the cantilever frequency. A split-coil superconducting magnet was used to generate magnetic fields for the experiment, and a rotation stage allowed for adjustment of the cantilever angle in the field. The base temperature of the system slightly below 8 K. The noise level of the system was measured using nanomagnet-coated cantilever, in zero field at 8.0 K. The standard deviation of the frequency measurement was found to be 0.28 mHz for a set of 24 s measurements. Using a Young's modulus $E = 126 GPa$ for Si_3N_4 (Yasumura 2000) to estimate $k = Ewt^3 / 4l^3 \approx 7\, mN/m$, and the cantilever length $l = 240 \mu m$, this corresponds to a moment sensitivity of 1.4 x 10^6 μ_B/T (from Equation (2.23)).

4.3 Angle Dependence at 8.0 K in a 1.6 T Magnetic Field

The cantilever resonant frequency was measured as a function of angle in a 1.6 T magnetic field, at a temperature of 8.0 K. The results are shown in Figure 4-4. The data

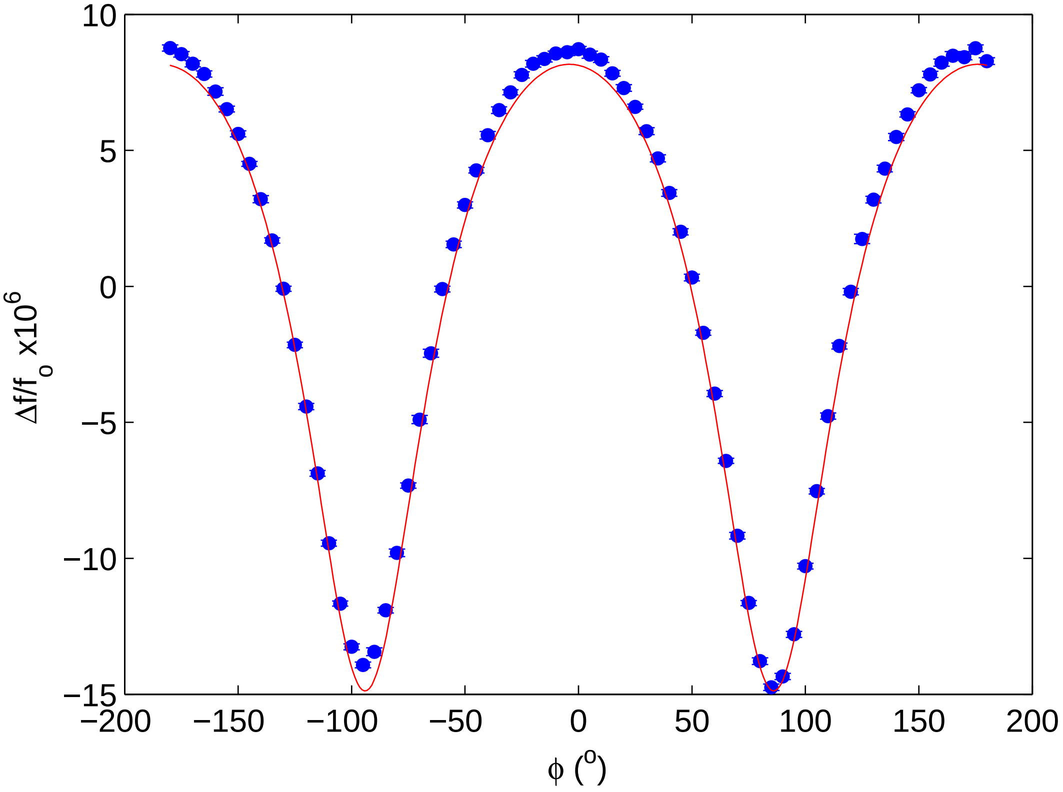

Figure 4-4: The cantilever frequency Δf was measured as a function of the cantilever-magnetic field angle ϕ in a 1.6 T magnetic field, at a temperature of 8.0 K. The data are illustrated by the blue points. The shape of the curve is fit reasonably by a numerical model using $B_a = -0.47T$, as shown by the red curve.

were modeled using the numerical model presented in Section 2.2.1, with a hard axis ($B_a < 0$; the magnetic moment would be oriented in the plane of the cantilever in the absence of a magnetic field, with all orientations in that plane possible) perpendicular to the cantilever surface. This situation might be expected for randomly oriented interacting magnets, which could be the situation here for nanomagnets clumped together on the surface of the cantilever. The shape of the data is reasonably well fit for $B_a = -0.47T$. However, properties of the nanomagnets themselves were not determined due to the difficulty of modeling a set of randomly oriented nanomagnets.

4.4 Hysteresis Measurements at 8.0 K

The cantilever resonant frequency was measured as a function of magnetic field, with the field aligned parallel to the length of the cantilever ($\phi = 0^\circ$). The nanomagnet moments were first saturated by applying a –1.6 T magnetic field. Measurements were subsequently taken at fields between –1.6 T and 1.6 T, to determine the hysteresis in the sample.

The frequency hysteresis loop is shown in Figure 4-5. The scan shows evidence of small hysteresis, with the positions of the red and blue colored data points with respect to each other being as expected for a ferromagnetic sample. However, despite this consistency with a ferromagnetic signal it is not completely certain that the hysteresis is due to magnetic effects and not due to hysteresis in the generation of the magnetic field or to frequency drift with temperature. No saturation was observed up to the maximum field possible with the current source presently in use (1.6 T); this could be an indication that there are some clumps of large numbers of particles which are responsible for the majority of the observed hysteresis. Equation (2.22) can be rearranged to give the following form:

$$\frac{f_o}{\Delta f} = \frac{kl^2}{m}\frac{1}{B} + \frac{kl^2}{m}\frac{1}{B_a} \tag{4.1}$$

Some numbers were extracted using the data for fields of at 0.6 T and greater, with the assumption that at this field the moment of the particles should be near saturation and

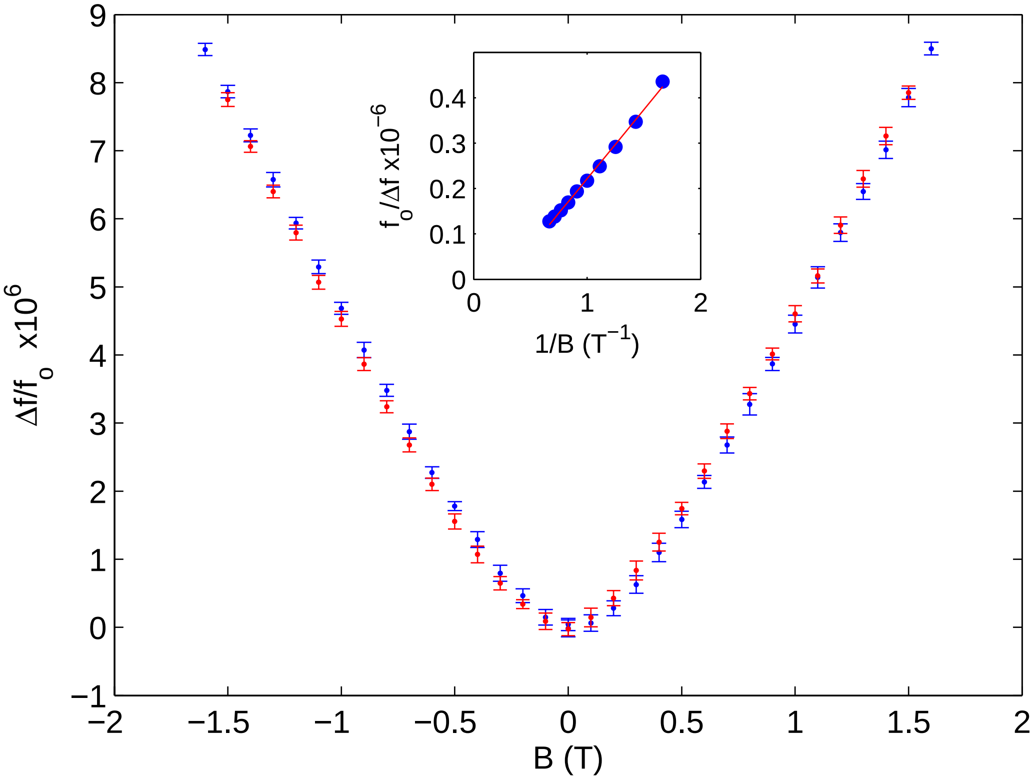

Figure 4-5: The cantilever frequency shift Δf was measured as a function of magnetic field angle B at a temperature of 8.0 K, with the field aligned along the length of the cantilever. Some hysteresis is observed, although it is not clear that this is due to magnetic effects and not due to frequency drift in the system, or hysteresis in the superconducting magnet and/or current source. The inset shows the data taken above 0.6 T plotted as $f_o/\Delta f$ vs $1/B$. From the slope and intercept respectively, the magnetic moment was determined to be ~10^8 μ_B, and the anisotropy field B_a was calculated to be –4.8 T, using Equation (4.1).

aligned with the magnetic field. From the slope of a plot of $f_o/\Delta f$ vs $1/B$, the moment was determined to be ~10^8 μ_B, and from the intercept, B_a was calculated to be –4.8 T. Without SEM images from which the number of particles could be obtained, it is difficult to say much about the value of the moment, other than that it is not obviously incorrect, as it corresponds to the moment from ~3000 particles if they are assumed to be ideal hcp Co spheres aligned with their easy axes along the length of the cantilever. However, the anisotropy value is large in absolute magnitude, and is not consistent with the value determined from the angle dependence data. As the particle anisotropy axes are likely to be distributed throughout many directions, the theory used to describe the sample here is too simplistic. Substantial numerical modeling is necessary to account for such a distribution.

4.5 Temperature Dependence of Hysteresis

Hysteresis measurements were made at different temperatures, as shown in Figure 4-6. Measurements at 20 K and 50 K also show some small amount of hysteresis, although with higher noise levels. The overall magnitude of the observed frequency shifts at these temperatures is smaller than at 8 K. The temperature dependence of the frequency shifts was further examined by measuring frequency vs temperature in the absence of a field (the frequency is quite dependent on temperature, so a baseline is needed) and in 1.6 T. The results are shown in Figure 4-7. A bend in the $\Delta f/f_o$ vs $1/T$ curve near 15 K indicates an increase in the strength of the magnetic anisotropy with decreasing temperature. I was surprised at the fact that this occurred at such a low temperature, since the blocking temperature of the particles should be around 200 K (Dinega 2001), such that I would expect a strong magnetic signal at a temperature of 20 K. The low signal may be due to the fact that the particles were 7 weeks old at the time they were measured. Oxidation is likely to have occurred, such that the magnetic volume of the particles was effectively reduced.

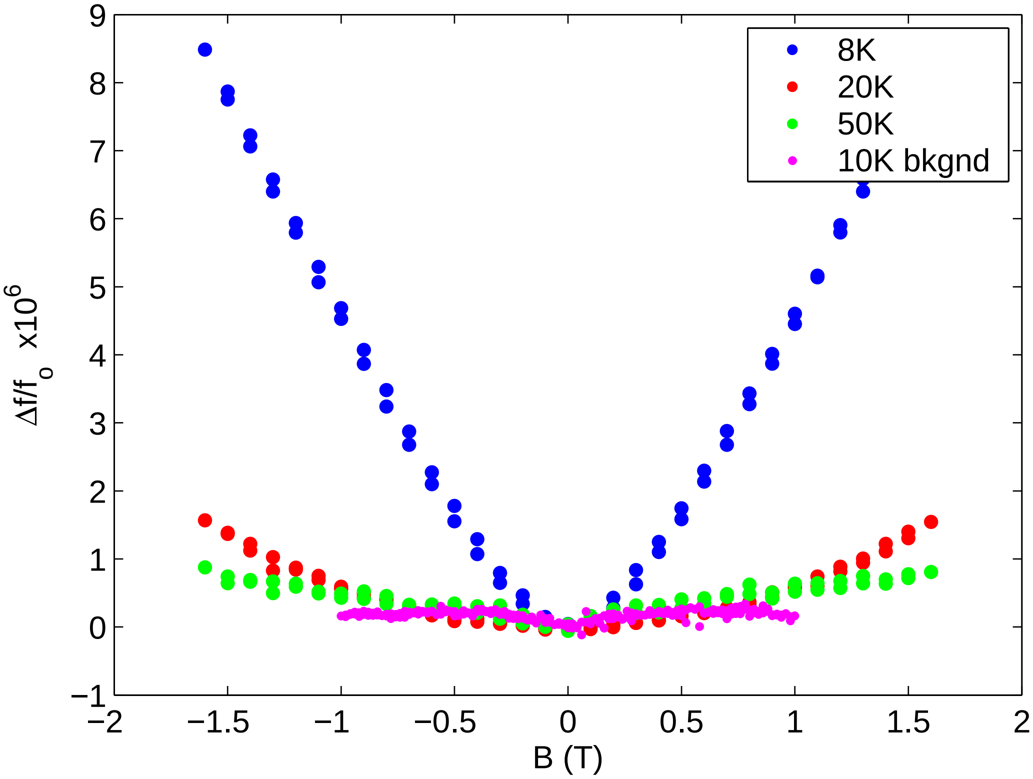

Figure 4-6: The cantilever frequency shift Δf as a function of magnetic field B at various temperatures, with the field aligned along the length of the cantilever. The signal drops dramatically with temperature, such that by 20 K there is only a small signal measured. The magenta curve illustrates the field dependence of the frequency shift of a cantilever without nanomagnets as a reference level.

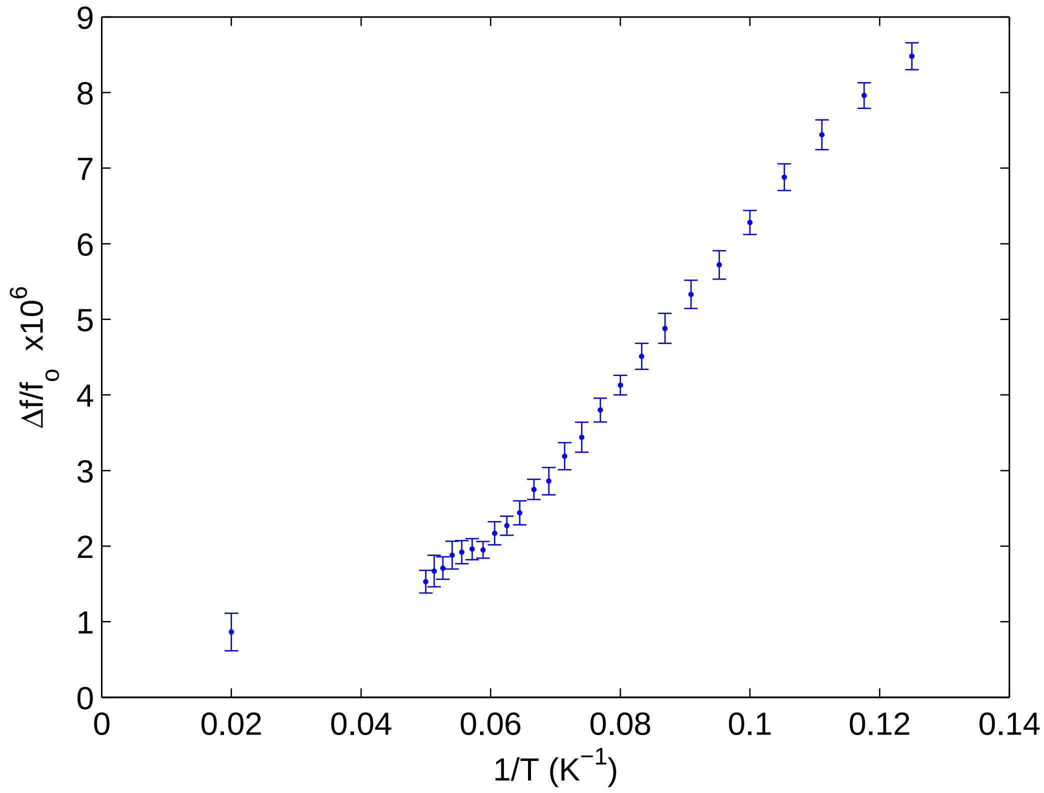

Figure 4-7: The frequency shift Δf was measured as a function of temperature T in a 1.6 T field. The signal has largely disappeared by 20 K. Data between 20 and 50 K was not obtained due to instrumentation problems that developed.

4.6 Summary

Unfortunately, new noise problems developed which prevented the further taking of useful data. If the problems could be solved, future measurements which would be useful are measurements at magnetic fields above 1.6 T to check for saturation of the moment, and lower noise f vs T data, over a more complete range of temperatures, and ideally at temperatures lower than 8 K (the current lower limit for the temperature in the cryostat). Also, SEM images of the cantilever used in the measurements must be obtained to determine the number and distribution of the Co particles. The new scanning electron microscope available in the Geballe Laboratory for Advanced Materials (which was not present at the time these measurements were carried out) has the resolution to image the nanomagnets, and would be an important tool for preparing samples for magnetometry studies.

I do feel that the cantilever magnetometry technique has the potential to be a powerful and interesting tool for characterizing magnetic samples. This has been demonstrated previously by other groups. At IBM, Barry Stipe et al used the technique to characterize the magnetic properties of materials for use as MRFM (magnetic resonance force microscopy) tips, and measured the magnetic dissipation in the materials (Stipe et al. 2001). At the University of California at Santa Barbara, Jack Harris and David Awschalom studied the magnetic properties of a two-dimensional electron gas integrated into a GaAs cantilever using the magnetometry technique (Harris et al. 1999; Harris 2000; Harris et al. 2000; Harris et al. 2001). At Stanford, John Chiaverini and Aharon Kapitulnik studied vortex dynamics in BSCCO using a cantilever magnetometer (Chiaverini et al. 2001).

With cantilevers optimized for making magnetometry measurements, the cantilever magnetometry technique could be a very sensitive one. The modeling in Section 2.2.1 further shows the potential power of the technique. In the future, if anyone were to return to doing magnetometry measurements, I would recommend setting up a system with the capability to control the cantilever-field angle, and initially developing an understanding of the technique and instrumentation by studying a magnetic sample with a well known anisotropy, such as a rectangular thin film on the end of the cantilever with a well understood shape anisotropy. It would be interesting to see if the modeling could accurately describe measurements on such a sample, and if it could then be extended to studying more complicated and challenging samples such as nanomagnets.

Chapter 5 : Magnetic Force Microscopy of Vortices in Nb

Imaging vortices in a superconductor is considered to be one of the greatest challenges for a magnetic force microscope (Hug et al. 1999). A number of groups have succeeded in imaging vortices however. Low temperature force microscopes have been constructed using fiber optic interferometers (Hug et al. 1999; Roseman and Grütter 2000) and piezoresistive cantilevers (Yuan et al. 1994; Volodin et al. 2000), and have been used to image vortices in YBCO (Yuan et al. 1996; Moser et al. 1998), BSCCO (Yuan et al. 1996; Pi et al. 2003), Nb (Roseman and Grütter 2001; Volodin et al. 2002), and $NbSe_2$ (Volodin et al. 2000).

Initial MFM studies of vortices by the Güntherodt group focused on the development of the technique and instrumentation of low temperature magnetic force microscopy. They also demonstrated the creation of vortices and vortex bundles, vortex manipulation, and depinning measurements (Moser et al. 1998), and studied a vortex-glass phase in YBCO (Moser et al. 1995). More recently, this group has focused on further development of low temperature MFM and on quantitative MFM measurements and calibration, but without a focus on superconductivity (Hug et al. 1998; Hug et al. 1999; van Schendel et al. 2000).

The group in Leuven has developed a technique using the 3rd resonance of piezoresistive cantilevers to improve the noise sensitivity (by operating far from the knee of the 1/f noise curve of the piezoresistor) (Volodin et al. 2000), and were the first (and to date only) to observe the formation of a vortex lattice, in $NbSe_2$ (Volodin et al. 1998). They have imaged vortices in Nb and $NbSe_2$, and have worked on correlating vortex pinning sites with topography, concluding that vortices are pinned at grain boundaries (Volodin et al. 2002; Volodin et al. 2002). However, this involves compensating for the difference in position between the physical tip (for AFM imaging of the surface structure) and the magnetic tip.

At McGill University, Mark Roseman and Peter Grütter have imaged vortices in a Nb thin film patterned with antidots (Roseman et al. 2001; Roseman and Grütter 2002). They have also measured the penetration depth using force gradient approach curves (Roseman et al. 2001), and by fitting constant height images of vortices (Roseman and Grütter

2001). Force gradient approach curves have also been used to measure the penetration depth in YBCO at the University of Texas at Austin (Lu et al. 2002).

In this chapter, I present images of vortices in a niobium film taken with the microscope I constructed, which is described in Chapter 3. The niobium film is a 300 nm thick sputtered film on a silicon substrate provided by HYPRES. The critical temperature T_c was measured to be 8.6 K using a Quantum Designs Squid Magnetometer as shown in Figure 5-1. The cantilever used for the measurements is a MESP standard magnetic force microscope cantilever from Veeco. The cantilever had a resonant frequency of 71 kHz and a spring constant of 3 N/m. The images presented in this chapter were all taken using the constant height mode described in Section 3.7.2. Additional images of vortices in the niobium film acquired during later cooldowns are presented in Chapter 6.

5.1 Imaging as a Function of Field

Images of vortices in the Nb film were taken as a function of the magnetic field. The sample was first heated above T_c, and then cooled in the desired magnetic field. The field from the MFM tip was minimized by withdrawing the cantilever from the sample using the microscope's coarse approach mechanism, but it does still contribute somewhat to the field at the sample. Frequency shift images were then taken using at a tip-sample separation of 350 nm. The images taken at various fields are shown in Figure 5-2.

If all vortices are trapped, the number of vortices expected in an area A of the sample is given by:

$$N_{vortex} = \frac{BA}{\Phi_o} \tag{5.1}$$

where B is the magnetic field and $\Phi_o = 20.7 G\mu m^2$ is the superconducting flux quantum. A value for Φ_o can be estimated from the slope of the N_{vortex} vs B curve in Figure 5-3. The slope gives a value for the flux quantum $\Phi_{o_{meas}} = 41.04\mu m^2 / 2.12 G^{-1} = 19.3 G\mu m^2$. This is reasonably close to the actual value for Φ_o. Equation (5.1) may in fact not be completely valid, or some vortices may not have been trapped within the scan range. The discrepancy could also be due to a slight inaccuracy in the scan calibration. It should be

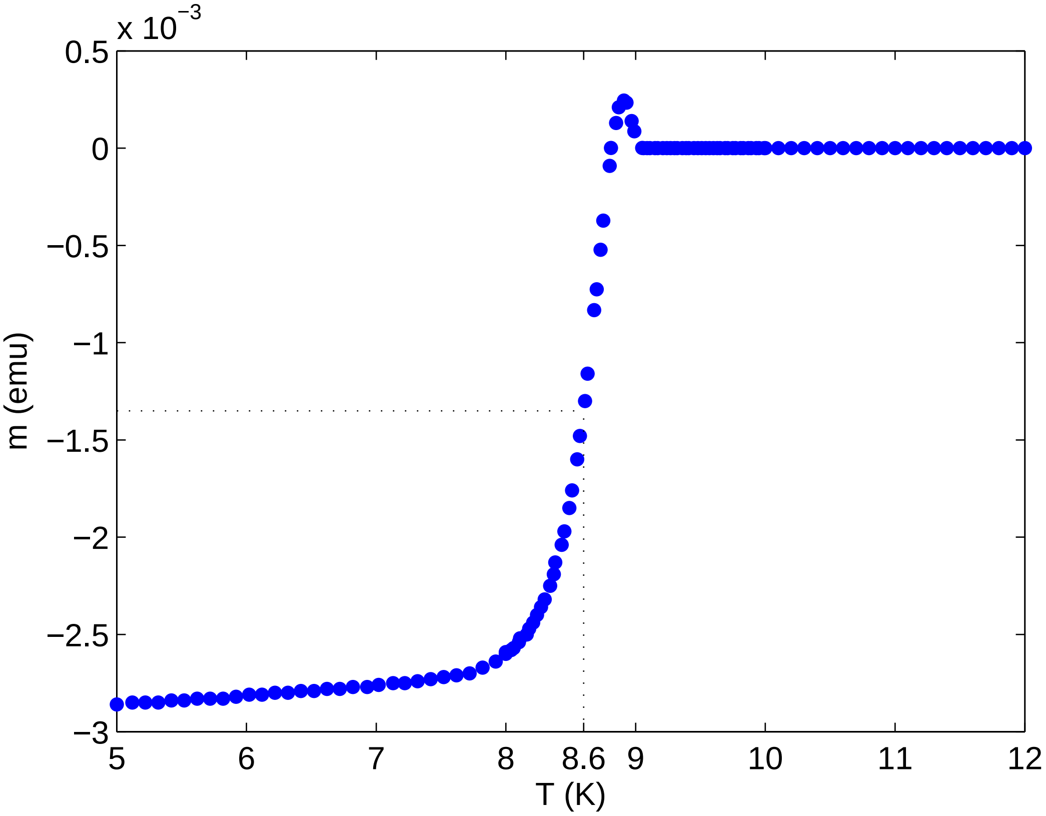

Figure 5-1: The critical temperature T_c of the Nb film studied was determined by measuring the magnetic moment m as a function of temperature T using a Quantum Designs SQuID Magnetometer. T_c was determined to be 8.6 K by taking the midpoint of the moment signal between the zero level well above T_c and the level at which the curve starts to levels off (about –0.0027 emu).

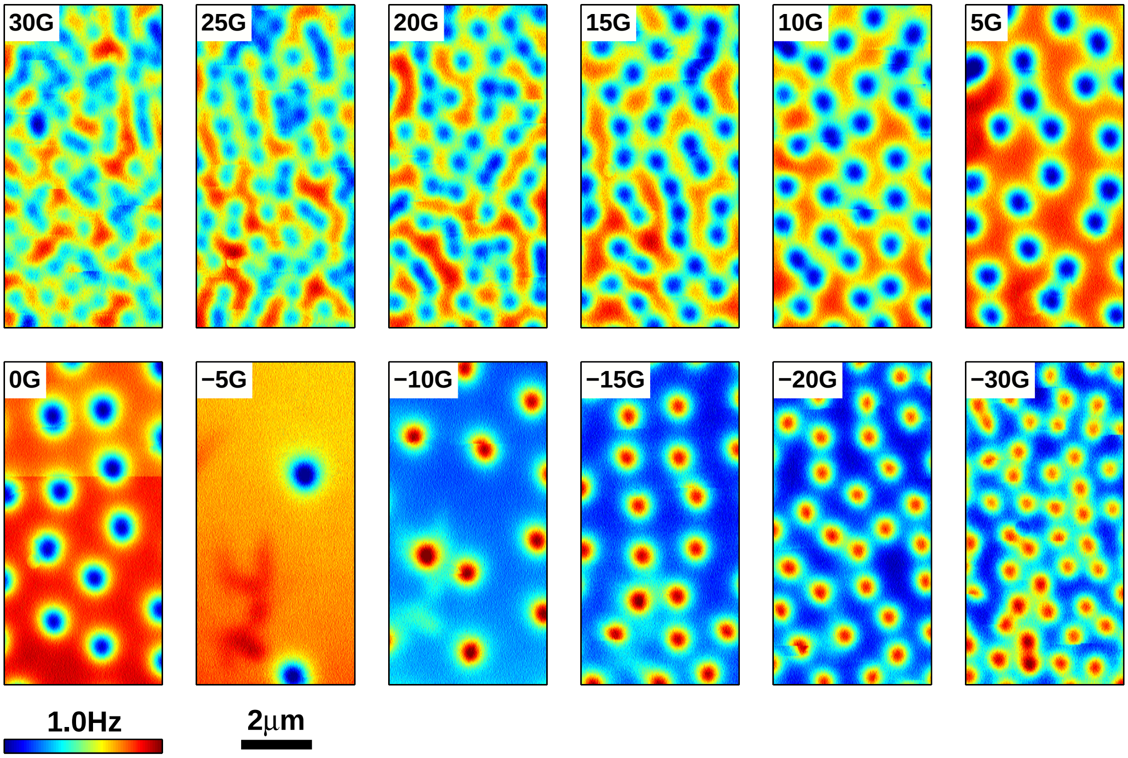

Figure 5-2: Magnetic force microscope images of vortices in a 300 nm thick Nb film as a function of magnetic field. These images were taken at a temperature of 5.5 K and a scan height of 350 nm. The vortices appear more intense at lower fields because the overlapping fields between neighboring vortices at high fields decrease the total contrast in those images.

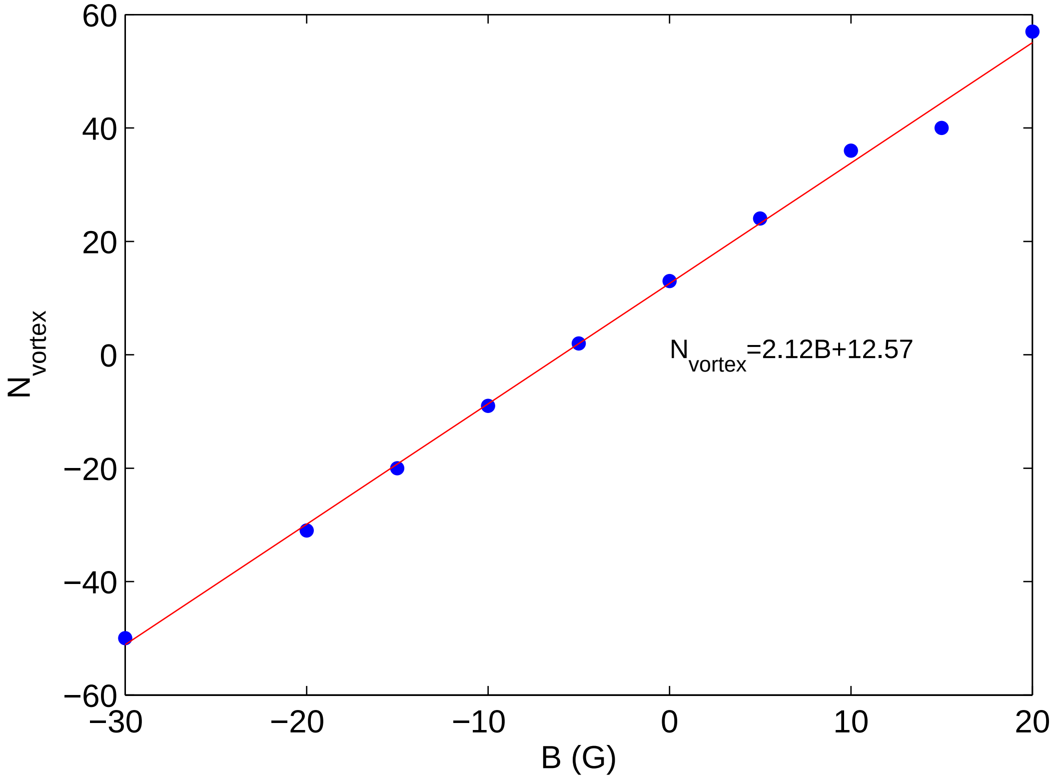

Figure 5-3: The number of vortices in the field of view of the MFM in Figure 5-2 scales linearly with the magnetic field. The offset in the magnetic field needed to obtain zero vortices is due to the field from the MFM tip, trapped flux in the superconducting magnet, and other ambient fields in the laboratory (e.g. Earth’s magnetic field).

noted that these images (and all other images in this chapter) were taken with only half of the normal x scan range due to a malfunctioning high voltage amplifier channel, while the scan calibration was carried out for the full scan range.

5.2 Imaging as a Function of Temperature

Vortices were also imaged in the niobium film as a function of temperature. The film was first cooled through T_c in a -10 G magnetic field, following which the images were taken with a tip-sample separation of 400 nm. The results are shown in Figure 5-4. There are a few things worth taking note of from these images. To start, it is evident that the vortices are more strongly pinned at lower temperatures. At 6.5 K, the first signs of vortices shifting in between scan lines becomes evident. Large motions of vortices are apparent at 7K and 7.5K, and by 8K the vortices are easily depinned by the radial force from the MFM tip. At 9K the sample is no longer superconducting, and vortices are not present. Line scans from the images are shown in Figure 5-5.

5.3 Imaging as a Function of Height

Images were also taken as a function of height, after cooling through T_c in a -10 G field, to the measurement temperature of 5.5 K. The images are shown in Figure 5-6, and line scans are illustrated in Figure 5-7 to demonstrate the spatial resolution. The spatial resolution increases as the separation decreases, indicating that the resolution is limited by the separation rather than by the cantilever tip itself. As the tip-sample separation is decreased, the signal strength increases, due to the increased force gradient observed closer to the vortices. However, the radial force exerted by the cantilever tip on the vortices also increases with decreasing scan height, leading to an increase in depinning. The depinning is particularly evident in the scans at 230 nm and 170 nm, in which numerous vortices are observed to have shifted in between scan lines.

5.4 Modeling

The images from Figure 5-6 were analyzed in an attempt to characterize the magnetic properties of the cantilever tip. From Section 2.3, the stray field from a vortex can be

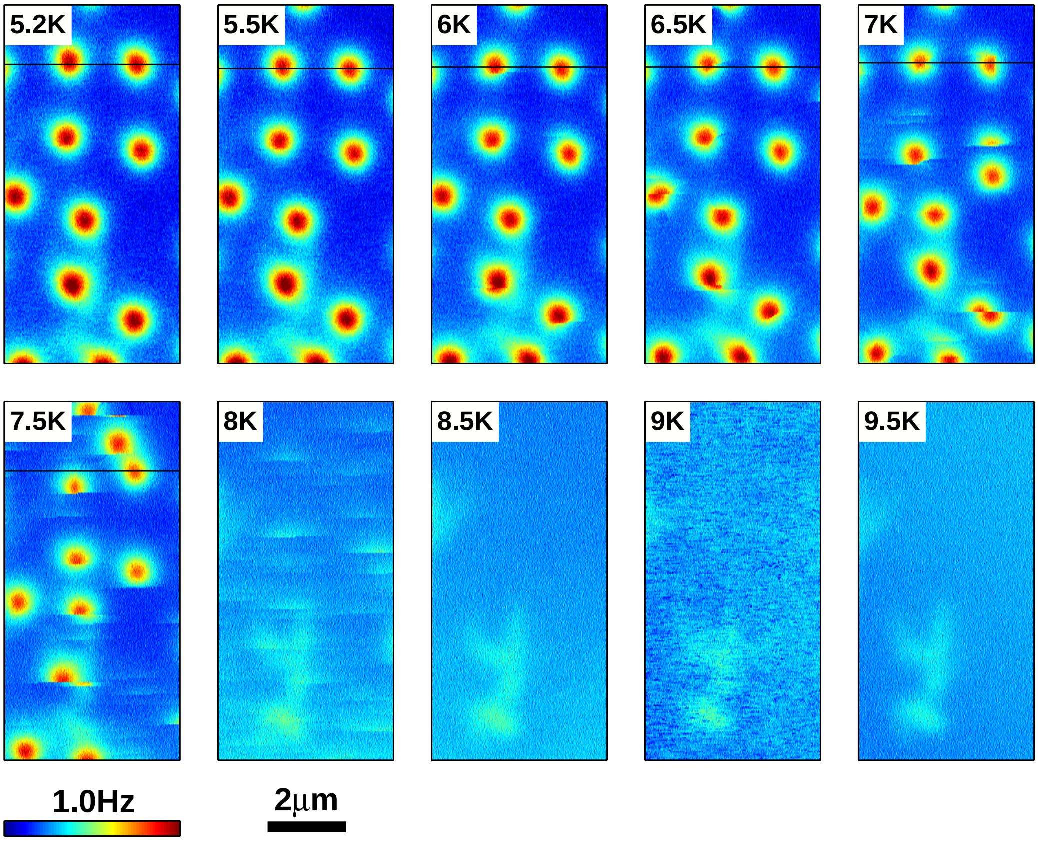

Figure 5-4: Magnetic force microscope images of vortices in a Nb film, taken at different temperatures. The scan height was 400 nm. As the temperature increases, depinning of vortices can occur, and vortex motion is occasionally observed between scan lines. The black line across each image indicates the location from which a line scan is plotted in Figure 5-5.

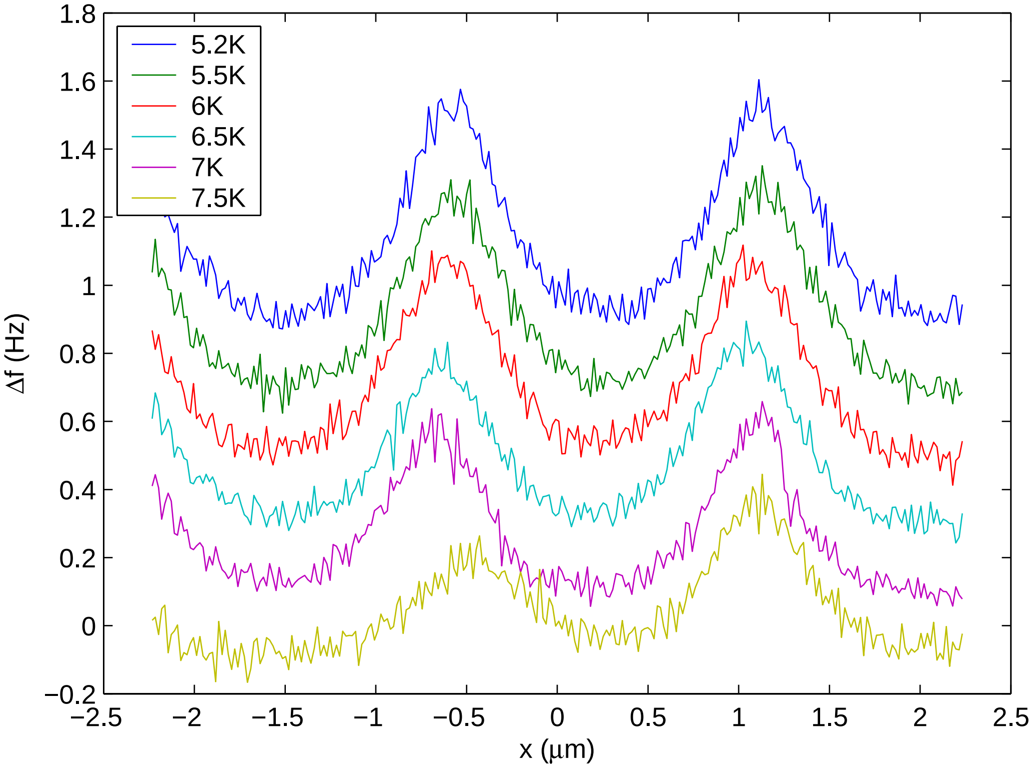

Figure 5-5: MFM line scans taken from the images in Figure 5-4. The curves have been offset by 0.2 Hz for improved visibility. The peak height decreases with increasing temperature because the vortex spreads out with an increasing penetration depth λ, decreasing the force gradient.

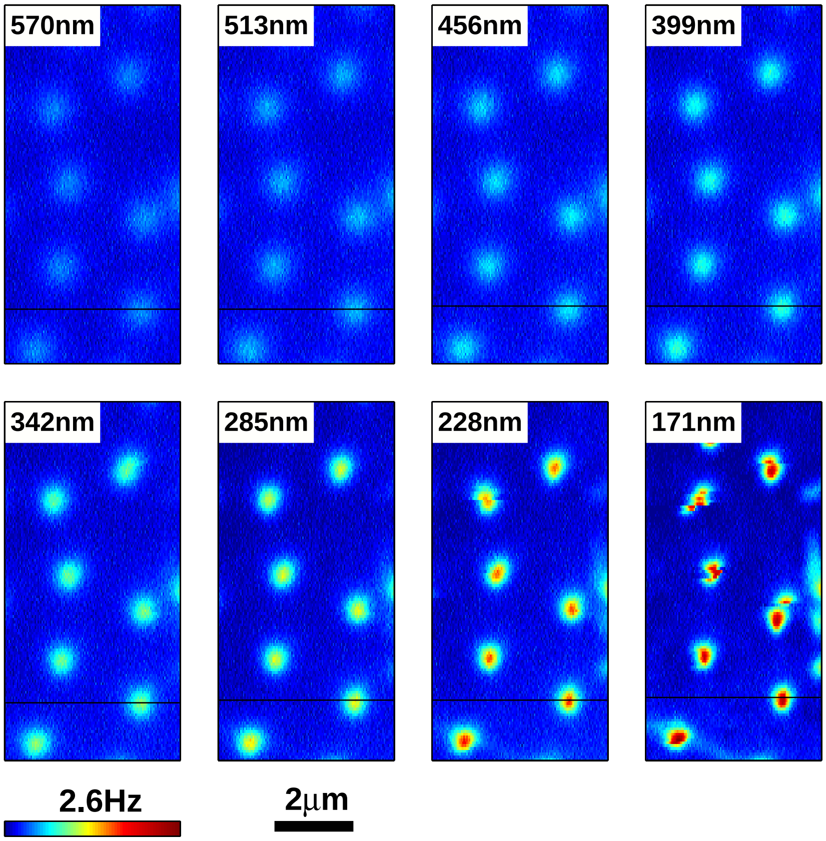

Figure 5-6: MFM images of vortices in Nb taken at different scan heights. These images were obtained at a temperature of 5.5 K. At lower scan heights, the MFM tip exerts more force on a vortex, and the probability that a vortex will depin increases. This is evident from the vortex shifts between scan lines at the lower heights. The black line across each image indicates the location from which a line scan is plotted in Figure 5-7.

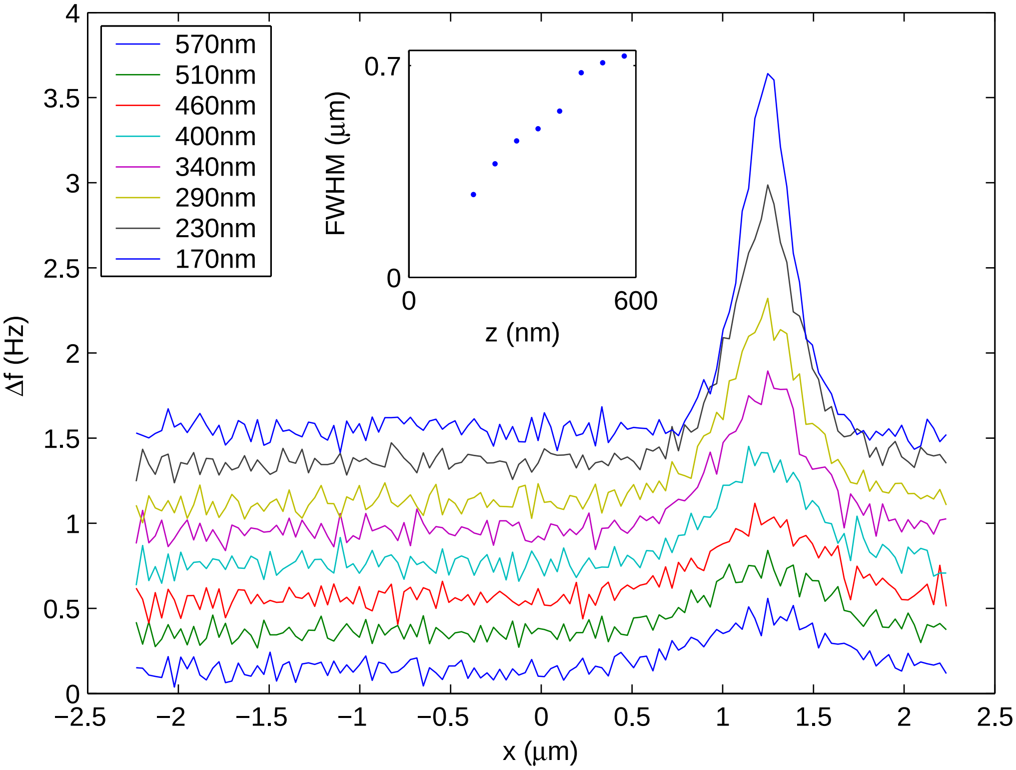

Figure 5-7: MFM line scans taken from the images in Figure 5-6. The lines have been offset by 0.2 Hz for better visibility. The signal strength increases at lower scan heights because the force gradient is stronger closer to the vortex. The spatial resolution also improves, as shown in the inset where the FWHM is plotted as a function of scan height.

approximated by the field from a monopole of strength Φ_o at a depth of λ below the sample surface. The tip can then be modeled as a point dipole using Equation (2.29), or as a point monopole using Equation (2.31). These are not necessarily expected to be good models for the tip, because the magnetic material is not limited to a point and the interaction must be integrated over the full extent of the tip (whether this is accomplished by a volume integration of dipole moments or a surface integration of monopoles). The point models are however worth examining with the hope that these simple models may give some insight into the origin of the measured signal. For the monopole tip model, the data were fit with the following equation:

$$\Delta f = \frac{f_o M_z \Phi_o}{4\pi k} \frac{\left((x-x_o)^2 + (y-y_o)^2 - 2\left(z+\lambda+d_{offset}\right)^2 \right)}{\left((x-x_o)^2 + (y-y_o)^2 + \left(z+\lambda+d_{offset}\right)^2 \right)^{5/2}} + \Delta f_{offset} \tag{5.2}$$

The free parameters in the fit are the vortex center position (x_o, y_o), a frequency offset term Δf_{offset}, the monopole moment per unit length M, and a term d_{offset} which allows for a difference between the location of the physical tip and the location of the effective tip moment. For the dipole tip, the following equation was used:

$$\Delta f = \frac{3 f_o m_z \Phi_o}{4\pi k} \frac{\left(z+\lambda+d_{offset}\right)\left(3(x-x_o)^2 + 3(y-y_o)^2 - 2\left(z+\lambda+d_{offset}\right)^2 \right)}{\left((x-x_o)^2 + (y-y_o)^2 + \left(z+\lambda+d_{offset}\right)^2 \right)^{7/2}} + \Delta f_{offset} \tag{5.3}$$

The free parameters are the same as for the monopole fit, but with M replaced by the magnetic dipole moment m. The results of the fitting are shown in Figure 5-8.

Neither the monopole nor the dipole model describes the tip well. Values for M, m, and d_{offset} can be found to obtain a reasonably good fit at large tip-sample separations, but different values are required at each scan height, as shown in Figure 5-9. This is likely because as the tip moves closer to the sample, the force gradients fall off more quickly, such that a smaller volume of the tip is significant for the measurement. At the lower scan heights (<250 nm), the vortex appears to be less round than at the larger heights. This may be due to the repulsive radial force exerted by the tip on the vortex, which causes the

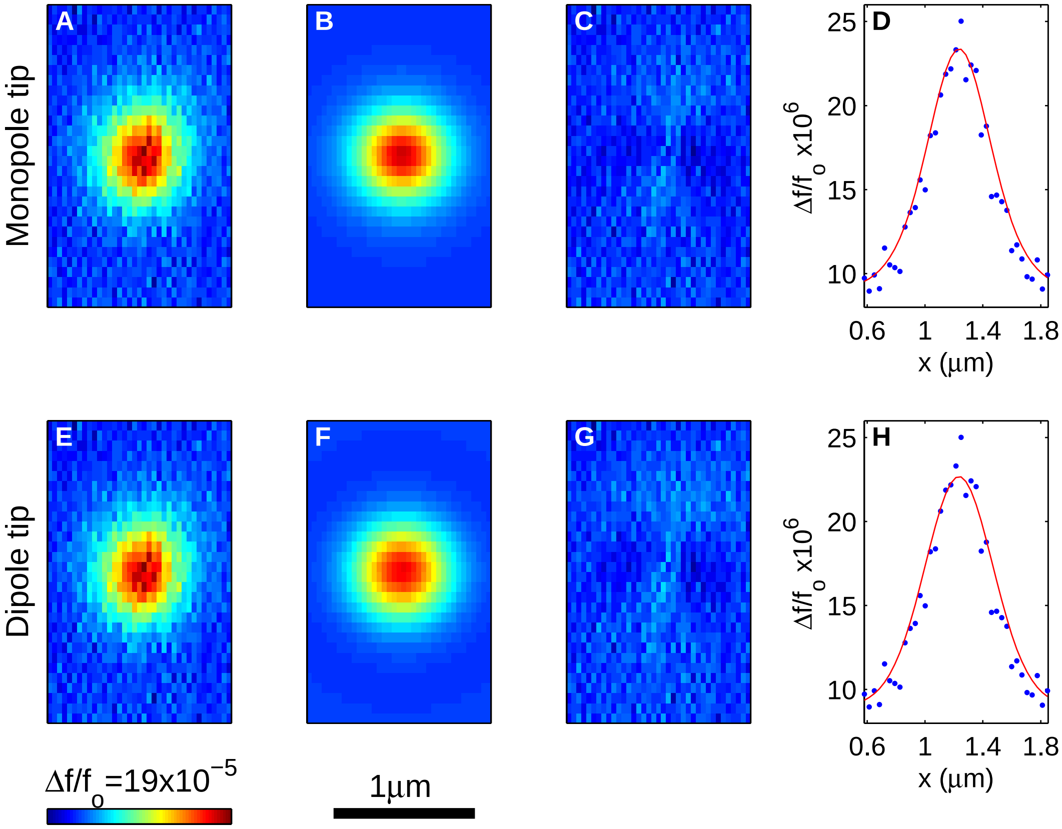

Figure 5-8: Fitting a vortex from Figure 5-6 imaged at a scan height of 290 nm. The vortex has been modeled as a monopole a distance $\lambda = 90nm$ below the sample surface. In the top row, the MFM tip has been modeled as a monopole oriented in the $\hat{z}$ direction. (A) The raw data. (B) A 2D fit for a monopole vortex-monopole tip interaction, with the fit parameters $x_o = 1.24\mu m$, $y_o = 3.08\mu m$, $f_o M/2k = -2.9\times10^{-7}\ \mu m/Gs$, $d_{offset} = 130nm$, and $df_{offset} = 9.3\times10^{-6}\,Hz$. (C) The error in the fit. (D) The fit through the center of the vortex. In the bottom row, the MFM tip has been modeled as a dipole oriented in the $\hat{z}$ direction. (E) The same raw data as in A. (F) A 2D fit for a monopole vortex-dipole tip interaction, with the fit parameters $x_o = 1.24\mu m$, $y_o = 3.08\mu m$, $f_o m/2k = -1.7\times10^{-7}\ \mu m^2/Gs$, $d_{offset} = 330nm$, and $df_{offset} = 9.8\times10^{-6}\,Hz$. (G) The error in the fit. (H) The fit through the center of the vortex. Both the monopole and dipole tip models fit reasonably well here. However, different parameters are needed for the fit at each scan height.

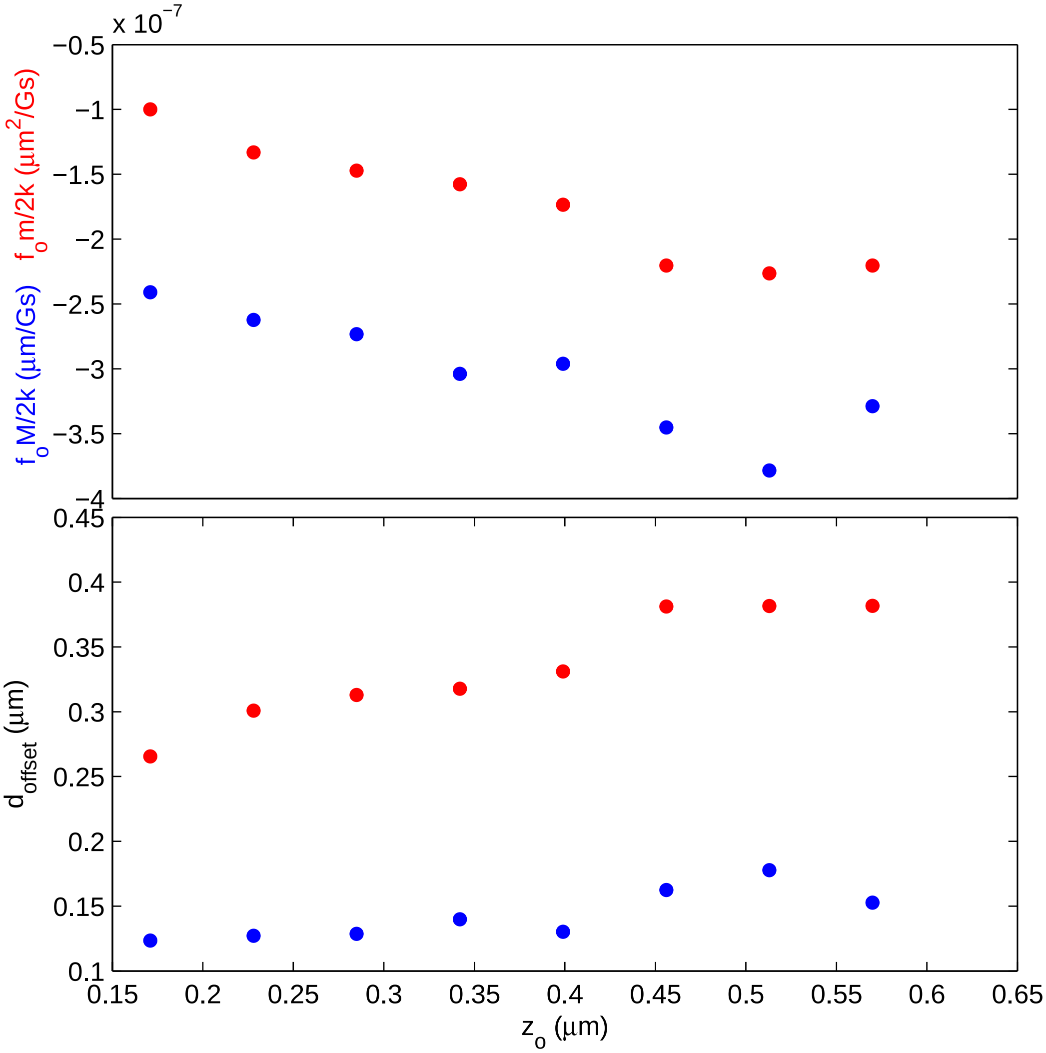

Figure 5-9: The values for M, m, and d_{offset} determined in fitting a vortex at different heights z_o. Values from the fit of a monopole tip are shown in blue, and values from the fit of a dipole tip are shown in red. The fit values change as a function of height because the effective size of the tip changes.

vortex to shift slightly (and reversibly) in the potential well of its pinning site as it is scanned. It may be possible to reduce this effect in the fitting by performing a 1D fit to a line scan through the vortex center rather than a 2D fit to an image, such that the oval shaped vortex is not fit. However, although the fit may improve, the shifting of the vortex is likely to have the effect of changing the apparent penetration depth. A 1D fit may be most useful for obtaining a value for the peak frequency shift. An additional source of error results from the fact that it is impossible to distinguish between z, λ, and d_{offset}, such that any error in the value of one parameter results in a corresponding error in the others.

To obtain a good tip calibration using a superconductor as the sample, one would ideally have a tip that was sufficiently weak so as to avoid disturbing the vortex while providing sufficient signal strength. Also, it is important to known the scan height and penetration depth accurately. Tips shaped as sharp spikes would be expected to be more monopole-like, however my one brief attempt to characterize a cantilever with a Fe-coated EBD (electron beam deposition) tip did not yield improved results. This inability to accurately describe an MFM tip with a monopole and/or dipole model has been observed previously (Lohau et al. 1999; van Schendel et al. 2000). The accurate modeling of an MFM tip (i.e. quantitative MFM measurements) is an important problem to solve, and is certainly worth further investigation, but it remains as a great challenge in magnetic force microscopy.

Chapter 6 : Vortex Manipulation and Pinning Measurements in Nb

An MFM cantilever exerts a force on a vortex which can depin the vortex. Generally, this is considered to be a disadvantage of the MFM technique because the sensor influences the sample that it is imaging. However, the cantilever can also be used to intentionally exert a force on a vortex, for the purpose of manipulating the vortex and for studying its pinning characteristics. A great deal of work has been done on pinning in superconductors to date, both in terms of characterizing the pinning using a variety of techniques (Lairson et al. 1990; Behler et al. 1994; Diaz et al. 1998; Jooss et al. 1999), and altering the pinning through the introduction of artificial pinning sites (Paulius et al. 1997; Martin et al. 1999). Very little work has been done to study pinning on small length scales however. Magnetic force microscopy offers a potentially powerful tool for characterization of vortex pinning at the individual vortex level. Forces and force gradients can be used both to image and manipulate vortices, and can be tuned to perform the desired function in-situ by adjusting the tip-sample separation, or ex-situ by changing the properties of the magnetic tip of the cantilever. Additionally, at very small tip-sample separations the cantilever can be used to measure atomic forces, and correlations can be drawn between magnetic and topographic images to determine the nature of the pinning site in which a vortex is trapped (Volodin et al. 2002). A previous study has demonstrated the potential of MFM for characterizing pinning (Moser et al. 1998).

In this chapter, I present my work on manipulation of individual vortices, which is the first ever demonstration of such control over vortex position using any technique. I also present a new MFM-based technique for measuring depinning, and demonstrate its capabilities by studying pinning in a Nb thin film. A further demonstration of the technique is presented in Chapter 7, where I present preliminary depinning measurements on a YBCO thin film.

6.1 Manipulating Individual Vortices

After my initial success with imaging vortices in my microscope, Kam and I were curious to push the microscope and see what it was capable of. At her suggestion, I attempted to manipulate vortices in a controlled fashion, along the lines of the manipulation of atoms with a scanning tunneling microscope (Eigler and Schweizer 1990), and the manipulation of nanoparticles with an AFM (Baur et al. 1998). In this section, I will present the manipulation of vortices from two separate cooldowns.

For the first manipulation experiment, I used the same MESP cantilever and Nb film that was used for the vortex images in Chapter 5. To obtain an initial arrangement of vortices, I heated the sample above T_c, and subsequently cooled to 5.5 K in an external field of 5 G. This field was chosen to give an appropriate vortex density, and to generate vortices of the polarity that would be attracted to the MFM tip. I then proceeded to image the sample using the constant height imaging method, at a scan height of 350 nm. At this height, the force exerted on the vortices is too low to depin them.

To move a vortex, I used the procedure illustrated in Figure 6-1. First, I identified a vortex which I desired to move, and selected its coordinates from the MFM image, along with selecting the coordinates of the desired new position. Next, I stopped the cantilever vibration, and moved the cantilever to a position above the vortex, at the scan height. I then reduced the scan height such that the tip was just above the sample surface, and proceeded to move the cantilever tip at that height to the new position. The cantilever was then raised back to the scan height, the vibration was resumed, and an MFM scan was obtained to determine whether or not the manipulation attempt was successful. In a successful attempt, the vortex would be pulled by the attractive force from the MFM tip and would end up in a pinning site at the desired new position.

The results of this manipulation experiment are shown in Figure 6-2. I was successful at moving vortices with the MFM tip, and was able to construct an “S” (for Stanford). The final location of a vortex is of course dependent on the availability of pinning site at or near the desired location. Pinning sites were found to be abundant in the material however, and a site was generally found close to the desired location. The strengths of the pinning sites were found to differ however, as the success of attempts to reposition a vortex varied. Some vortices moved to the new location with no trouble, however for others multiple attempts were required.

I attempted to improve upon these first results in a later cooldown. In this instance, I used a commercial AFM cantilever (DP18-Sting) from MikroMasch, with a resonant

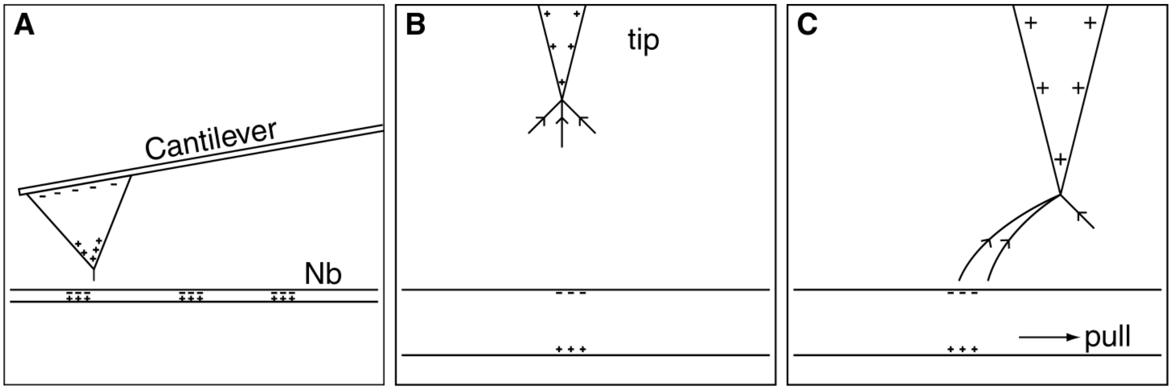

Figure 6-1: The procedure for manipulating vortices with an MFM cantilever. (A) Vortices are created in a superconducting film by cooling through T_c in a small magnetic field, with a polarity that generates vortices attracted to the MFM cantilever. (B) At large tip-sample separations, the force on the vortex is too small to depin it, and an MFM image can be obtained. (C) After identifying a vortex to be moved, the tip can be brought close to the sample surface. The vortex is depinned by the attractive force from the MFM tip and follows the tip to a new location in the sample, where it finds a new pinning site.

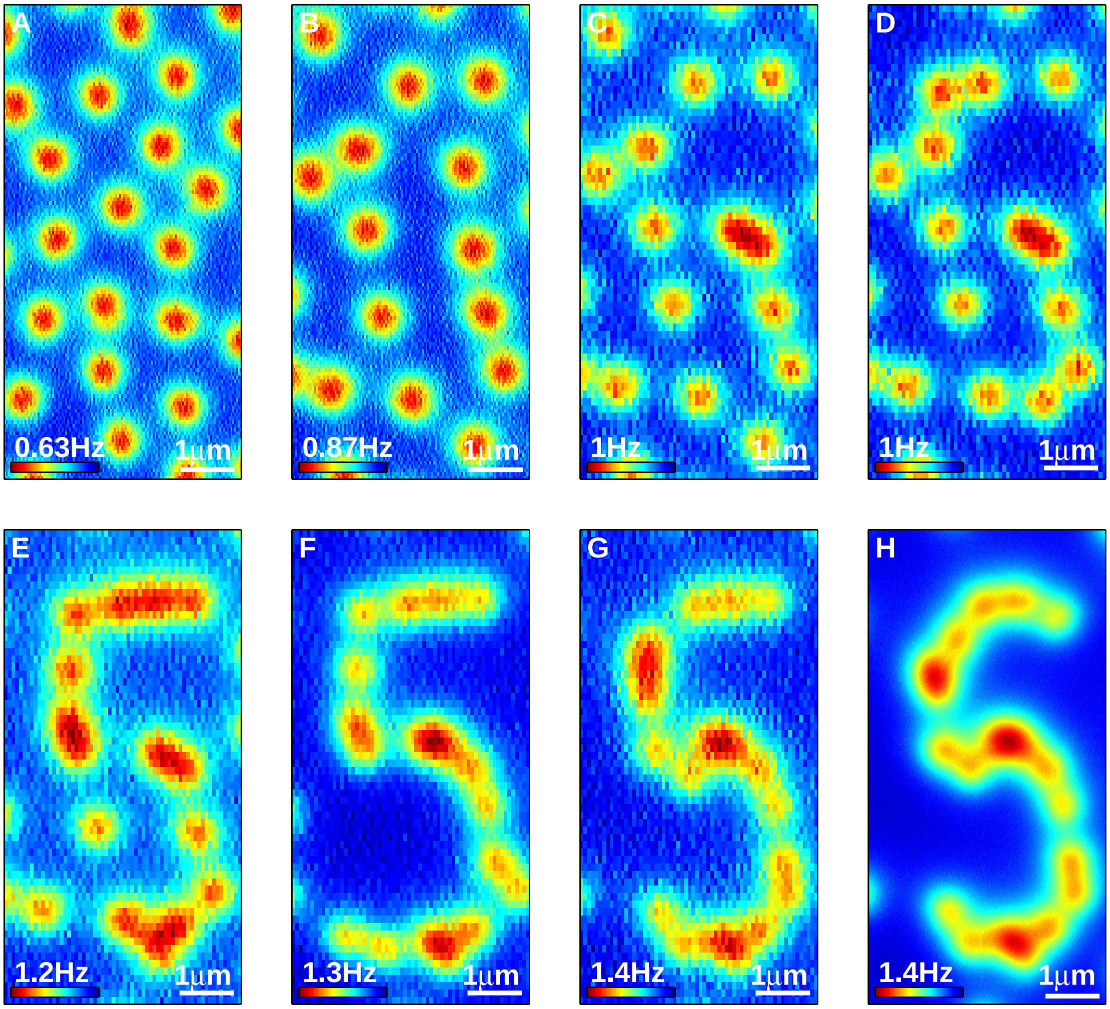

Figure 6-2: This series of images shows the manipulation of vortices in a niobium film to form an "S". (A) The initial configuration of vortices was obtained by cooling through T_c in a 5 G field. (B) For the first attempt to manipulate the vortices, I rastered the cantilever over the surface at a small separation, shifting the vortices to new pinning sites. (C-G) I moved vortices in a more controlled fashion by pulling individual vortices to new locations. (H) After several iterations, the vortex arrangement took the shape of a Stanford "S".

frequency of 81 kHz and a spring constant of 4 N/m. I chose a cantilever with an electron-beam deposition (EBD) tip, with the idea it would behave like a monopole tip due to its shape and aspect ratio. The tip was coated in the Ginzton Microfabrication Laboratory by evaporating a 40 nm thick Fe film, using a razor blade shadow mask to minimize the extent of the film on the cantilever beam itself. A titanium adhesion layer was used, and the Fe film was also coated with 7 nm of Au to protect against oxidation.

The strength of the magnetic tip was much less than that of the MESP tip used previously. For this reason, the manipulation was done at a higher temperature (7.0 K) than in the first experiment, such that the lower forces could be used to depin and tow the vortices. Otherwise I used the same manipulation procedure as described earlier. I repeated the procedure until the vortex assembly took the form of the initials "SU", for Stanford University. The initial and final vortex configurations are shown in Figure 6-3. The final vortex configuration was imaged at a temperature of 5.5 K and a scan height of 120 nm, which along with the increased number of pixels is why the image quality and resolution are much improved.

This is the first ever demonstration of vortex manipulation with actual control over the vortex position. It is a powerful new capability, and has the potential to enable a number of fascinating experiments. An experiment has recently been proposed (Olson Reichhardt and Hastings 2004) to study vortex entanglement by using an MFM to manipulate . Another experiment, suggested by David Nelson at Harvard University, is to use the MFM to measure the rigidity of a vortex. We chose to use our ability to manipulate vortices and to exert forces on them to study pinning in the Nb film, and later in a YBCO film as described in Chapter 7.

6.2 Depinning Measurement Procedure

The procedure I used to study pinning is illustrated in Figure 6-4. With the cantilever withdrawn to minimize the field at the sample, the sample is cooled through T_c to the measurement temperature (between 5.25 K and 8.50 K) in a small external field to generate a random arrangement of about 16-19 vortices within the field of view. The cantilever is then approached to the surface, and the surface position is determined from a Δf vs z curve as described in Section 3.7.2. The initial arrangement was imaged at a

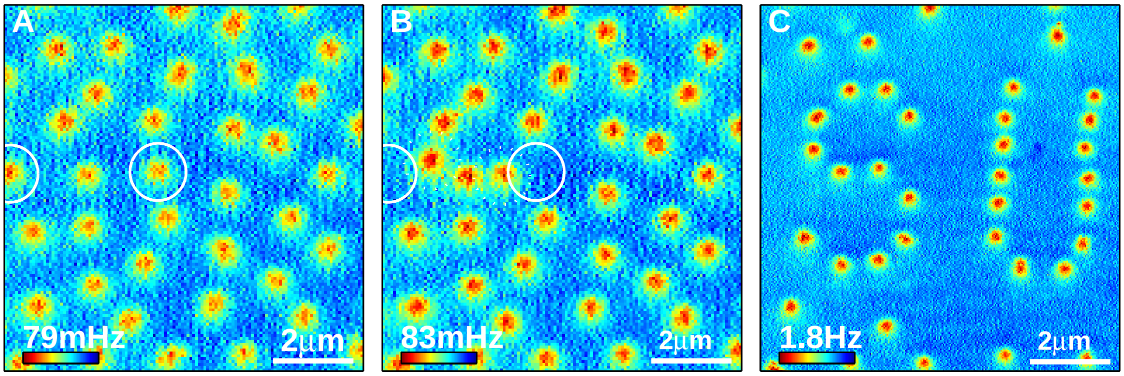

Figure 6-3: I improved upon the first manipulation experiment in a later cooldown using a silicon cantilever with an iron coated EBD tip. (A) The original configuration of vortices was obtained by field cooling the niobium film to a temperature of 7.0 K. (B) The attractive force between the cantilever tip and vortices was used to pull individual vortices to new locations. Here, two vortices have been moved to new positions. The original positions are illustrated by the solid circles, and the new locations by the dashed circles. To move a vortex, the cantilever was positioned immediately above the sample surface. Images were obtained at a height of 300 nm to evaluate the success of each manipulation attempt. (C) The manipulation procedure was repeated to arrange the vortices in the shape of the initials "SU", for Stanford University. This image was taken at a scan height of 120 nm and a temperature of 5.5 K, resulting in a higher quality and higher resolution image.

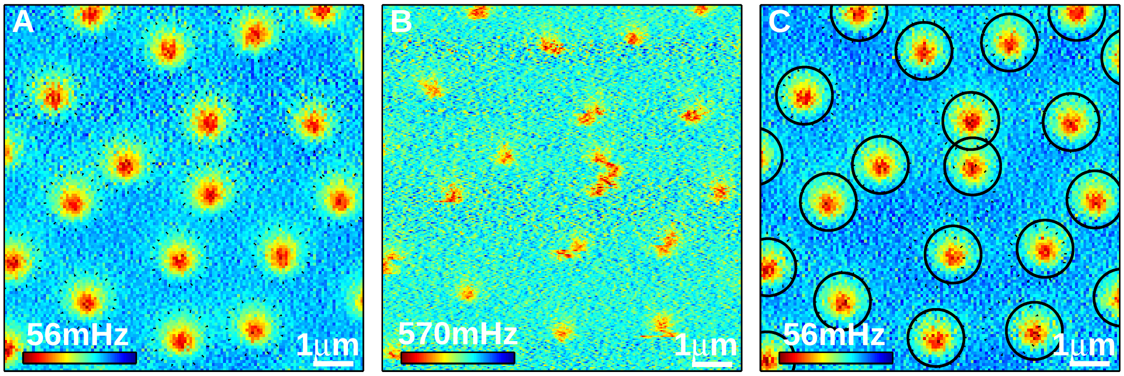

Figure 6-4: The procedure for determining depinning probabilities is illustrated here for a temperature of 7.0 K. (A) An initial vortex configuration is obtained by cooling the sample through T_c. The vortices are imaged at a scan height of 300 nm, at which the force is too low to depin vortices. The center positions, highlighted by the dashed circles, are determined by fitting the vortices by Gaussians. (B) The cantilever is scanned at a reduced height (in this example 45 nm) with the intention of depinning vortices. The cantilever vibration amplitude is reduced for this scan, resulting in an increased noise level in the image. (C) The final vortex configuration is imaged at the same scan height as in A. The center positions are determined by fitting the vortices, with the original positions illustrated by the dashed circles and the final positions by the solid circles. The depinning probability is determined by comparing the center positions from A and C. Here 9 out of 16 vortices depinned, giving a probability of 56%.

constant height of 290 nm, using a vibration amplitude of about 15 nm. The scan rate was 0.5 Hz. The vibration amplitude was then decreased to 3 nm, and the scan height was reduced to a value in the range 30 to 200 nm. A constant height scan was then executed at a scan rate of 1 Hz. At the reduced height, the force is increased substantially, and vortex depinning becomes possible. The lower vibration amplitude allows for smaller scan heights, however it also results in increased noise, contributing to the decrease in quality of the image as observed in Figure 6-4B. A third scan using the same parameters as the first verifies the final positions of the vortices. The effects of piezo hysteresis and creep were minimized by performing several initial scans at the safe imaging height, and immediately continuing with the following scan. The first and third scans were carried out using identical scan directions and scan parameters. Immediately following the final scan, the surface position was checked by measuring another Δf vs z curve. Some drift usually occurred during scanning, such that the surface position did not always match the position initially measured. This was likely due to piezotube creep, although temperature drift and instability of the coarse approach screw may have also contributed. If the final surface position was not within 12 nm of the initial surface position, the data was discarded. This resulted in 7% of the data being discarded for the purpose of determining the depinning probability.

The initial and final vortex positions were determined by fitting the frequency shift images with Gaussians. The theoretical vortex profile is not exactly Gaussian, but it is a symmetric peak and so a Gaussian is convenient for finding the vortex center. The positions of the vortex centers were compared between the two images to determine which vortices moved during the depinning scan, and the distance moved. To analyze the probability of vortex depinning, a cutoff was set at 100 nm, slightly more than the size of a single pixel in the 128 x 128 pixel images obtained. The vortices in the initial scan with their centers at least 100 nm inside the field of view were counted, and of those vortices, those with centers that moved 100 nm or more as determined from the final image were considered to have depinned. The procedure was repeated several times at each of a set of different depinning scan heights (effectively different forces) and temperatures. The probability of depinning P_{depin} at a given temperature and scan height was calculated by dividing the total number of vortices moved in all repetitions with those parameters divided by the total number of vortices:

$$P_{depin}\left(T,z\right)=\frac{\sum_{i} n_{i_{moved}}\left(T,z\right)}{\sum_{i} n_{i_{initial}}\left(T,z\right)} \tag{6.1}$$

where $n_{i_{initial}}$ is the number of vortices within the field of view for the ith measurement, and $n_{i_{moved}}$ is the number of vortices that depinned during the depinning scan. The error on the probability $\sigma_{P_{depin}}$ was calculated as the error for a binomial distribution (Bevington and Robinson 1992):

$$\sigma_{P_{depin}}=\sqrt{n_{initial}P_{depin}\left(1-P_{depin}\right)} \tag{6.2}$$

6.3 Depinning Probabilities

The results of the depinning measurements are shown as a function of temperature in Figure 6-5. As would be expected, depinning is more probable at higher temperatures. For low probabilities, the relation is an exponential. This is consistent with a hypothesis that the depinning-temperature relation is due to the greater amount of thermal energy available for a vortex to jump out of the potential well in which it is pinned at increasing temperatures. However, this temperature dependence could also be due to the pinning potential changing with temperature.

The depinning probability is illustrated as a function of scan height in Figure 6-6. The scan height is related to the force exerted by the cantilever tip on the vortex, with the force and thus the depinning probability increasing as the scan height is reduced. The radial component of the force is responsible for depinning vortices, however it is difficult to determine its size since it is the vertical force gradient that is actually measured. However, the vertical force can be determined by integrating the measured force gradient from images taken at various heights above the sample. In principle, the maximum radial force can be related to the maximum vertical force by geometrical factors, although they

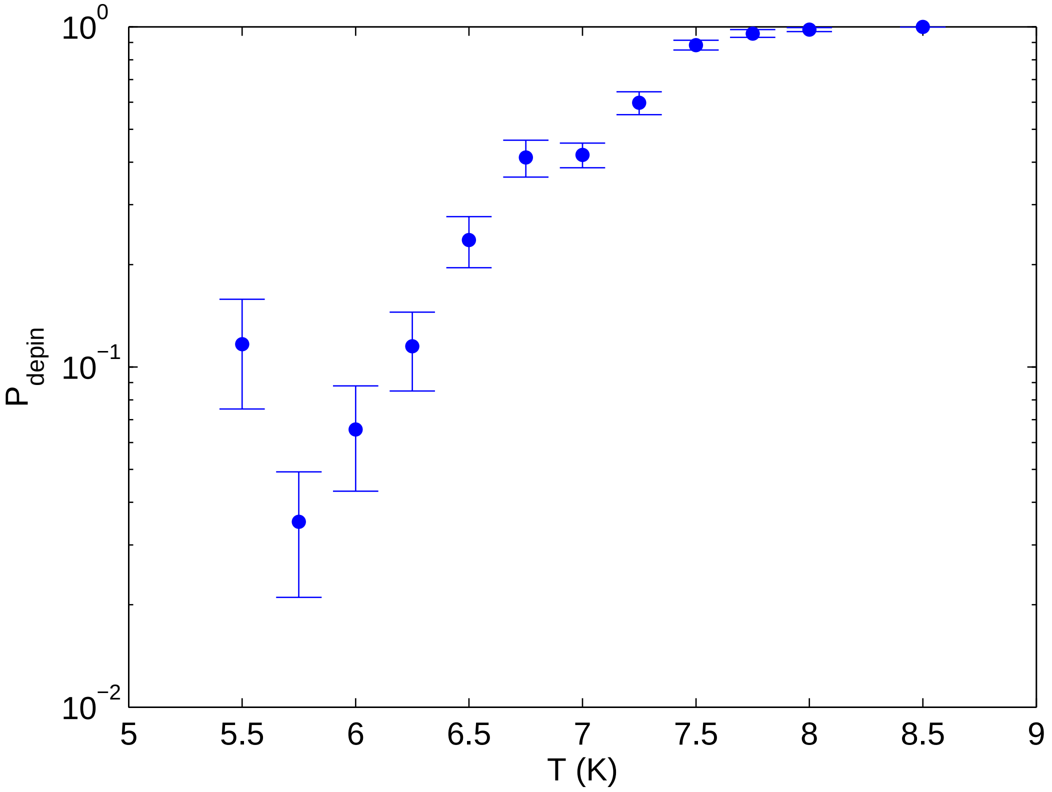

Figure 6-5: The probability that a vortex will be depinned was measured as a function of temperature at a scan height of 90 nm. An exponential relationship is observed at low depinning probabilities. I do not know why the 5.5 K point does not fit this relationship. It may be due to vortices becoming pinned in weak sites at this temperature compared to the higher temperatures.

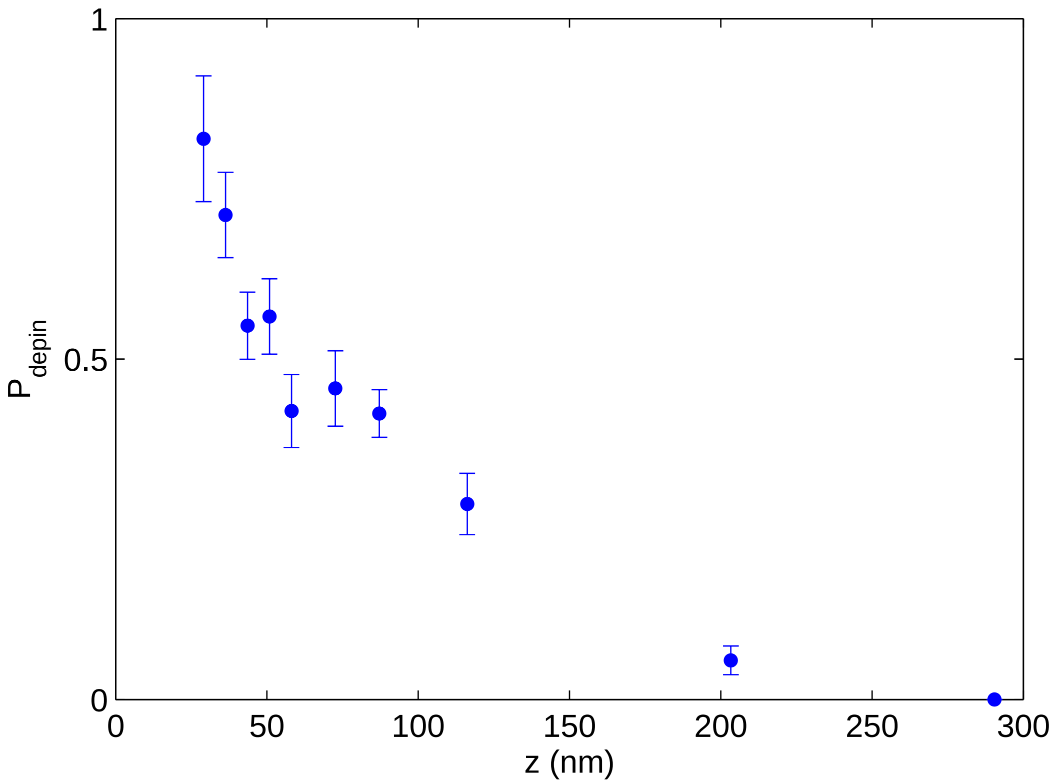

Figure 6-6: The depinning probability was measured as a function of scan height at 7.0 K. As the scan height is decreased, the force on the vortex and thus the probability of depinning increases.

are not known for our tip. For the ideal case of a monopole tip and a monopole vortex, the ratio between the maximum radial and maximum vertical forces is $2/3\sqrt{3}$.

To estimate the vertical force exerted by the cantilever tip on a vortex, I imaged vortices at various scan heights between 290 nm and 60 nm. The minimum and maximum forces were determined by integrating the data to determine the maximum frequency shift above the background, along with the minimum and maximum possible values for the spring constant k, as calculated using Equation (3.3).

The minimum possible force was estimated by numerically integrating the data. This was accomplished by fitting a line to each pair of successive Δf values on the log-log plot and integrating the resulting power law equation (i.e. four separate power law equations were used to integrate between each of the four pairs of successive points). The maximum force was estimated by fitting a power law to the data above 100 nm, illustrated by the dashed lines, and integrating the resulting equation between 290 nm and ∞ to determine the contribution from that range, and adding that to the numerical integration. In reality, we expect the force gradient to fall off more quickly than this power law fit indicates. At large separations the falloff would likely be described by a monopole-monopole interaction, which goes as $(z+\lambda)^{-3}$. This is illustrated by the dotted lines in Figure 6-7A. At 5.8 K, the force at a height of 60 nm falls in the range of 16 to 23 pN, and at 7.0 K, it falls in the range of 11 to 18 pN.

It is interesting to estimate the magnetic field from the MFM tip at the location of the vortex using this force. The force is given by $F = q_m B_{tip}$, where B_{tip} is the magnetic field from the MFM tip, and q_m is the effective magnetic charge of the vortex. I estimated q_m as follows. The magnetic field from a magnetic charge is:

$$\vec{B}_{mc}(\vec{r}) = \frac{\mu_o q_m}{4\pi} \frac{\hat{r}}{r^2} \tag{6.3}$$

where $\mu_o = 1.257\times10^{-6}\ H/m$ is the permeability of vacuum, and $\vec{r}$ is the position at which the field is to be determined, relative to the charge location. Comparing Equation (6.3) with Equation (2.32) for the field from a vortex modeled as a monopole, the effective magnetic charge of a vortex is $q_m = 2\Phi_o/\mu_o = 3.3\times10^{-9}\ Am$. For a force of 20

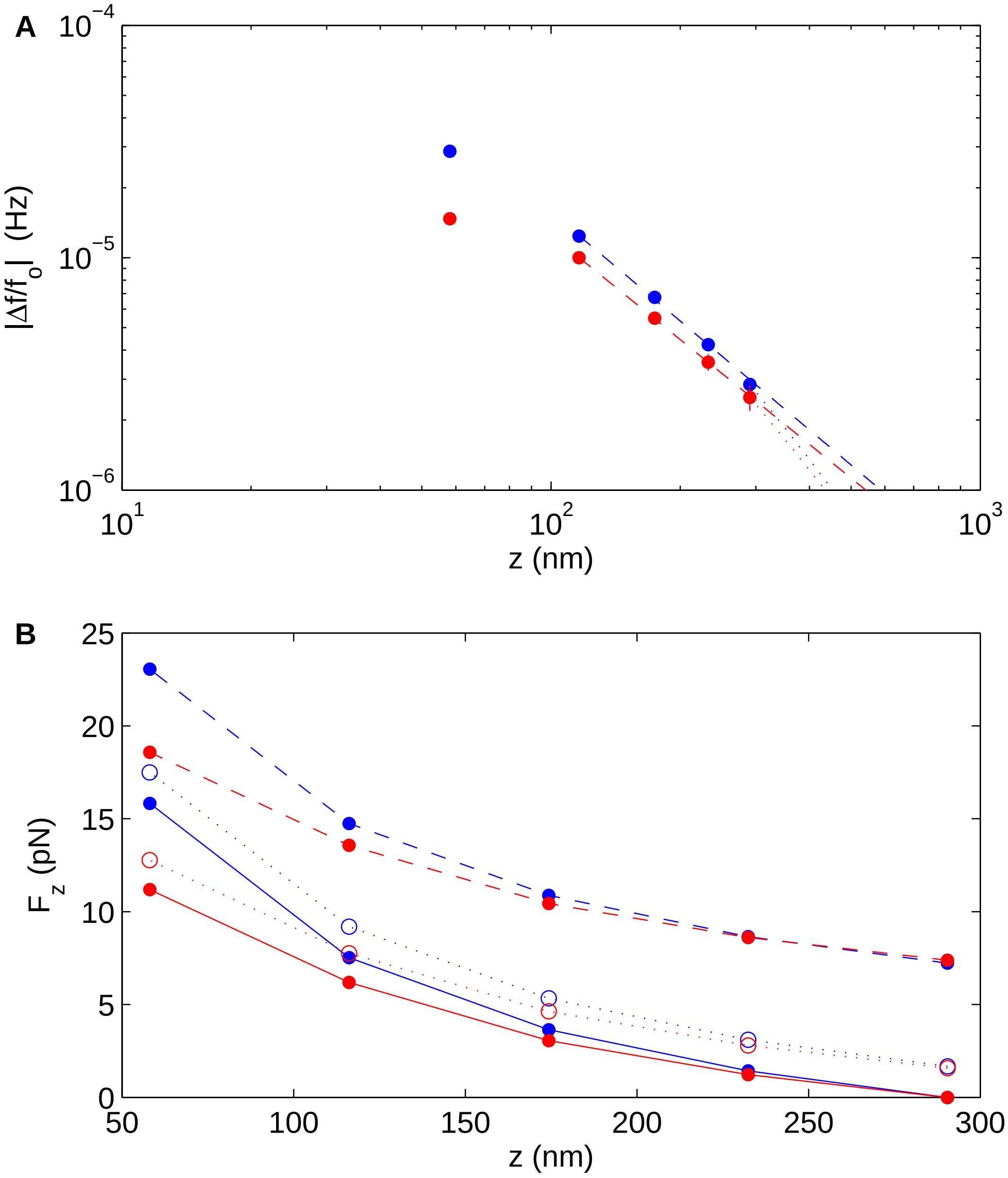

Figure 6-7: The vertical force exerted on the vortex was estimated by integrating the frequency shift (force gradient) vs scan height. (A) The peak frequency shift above a vortex was measured at different scan heights by imaging vortices, and fitting the data with Gaussians. The dashed lines are power law fits to the data, and the dotted lines represent the falloff expected for a monopole tip- monopole vortex interaction. (B) The maximum and two estimates for the minimum possible vertical force on the vortex were estimated by integrating the data shown in A, as described in Section 6.3.

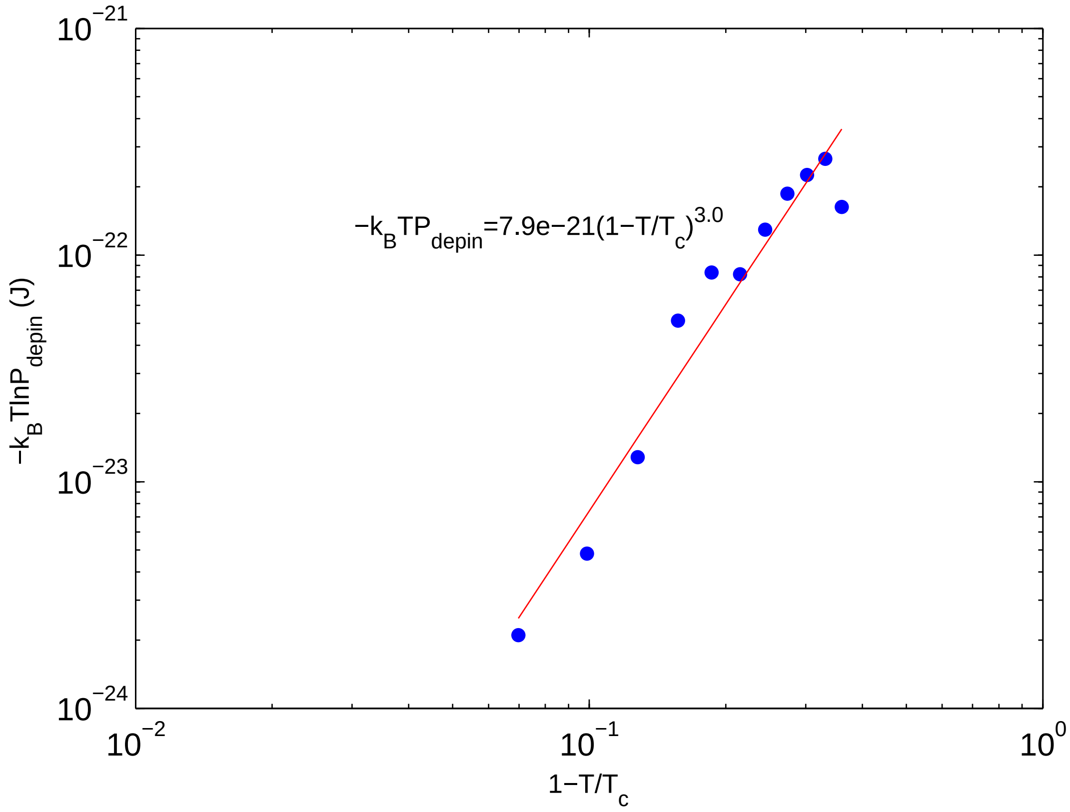

Figure 6-8: The temperature dependence of the pinning energy can be estimated by fitting $-k_B T \ln P_{depin}$ as a function of $1-T/T_c$. Here, the energy is described by $\left(E_{pin}-Fx\right) \propto \left(1-T/T_c\right)^3$.

pN, I estimate a B_{tip} of 6 mT, or 60 G. This could in the future be a valuable parameter for characterizing and comparing MFM tips used in this system.

The depinning probability data can also be used to extract some measure of the temperature dependence of the pinning energy E_{pin}. The depinning probability is given by:

$$P_{depin} = e^{-\left(E_{pin}(T)-Fx\right)/k_B T} \tag{6.4}$$

where F is the force exerted by the MFM tip on the vortex, and x is some depinning length scale (likely the coherence length). Substituting $U \equiv E_{pin} - Fx$, , and assuming a temperature dependence given by:

$$U(T) = U(0)\left(1-\frac{T}{T_c}\right)^n \tag{6.5}$$

one can obtain the following equation:

$$-k_B T \ln P_{depin} = U(0)\left(1-\frac{T}{T_c}\right)^n \tag{6.6}$$

$U(0)$ and n can be determined from the following:

$$\log\left(-k_B T P_{depin}\right) = n\log\left(1-\frac{T}{T_c}\right) + \log U(0) \tag{6.7}$$

This is illustrated in Figure 6-8. For the Nb film studied here, $U(0) = 7.9\times10^{-21} J$, and $n = 3.0$. It should be noted that this temperature dependence reflects the temperature dependence of U. E_{pin}, F, and x are all likely to be temperature dependent, such that the above equation describes the combined effect of each parameter.

This page intentionally left blank.

Chapter 7 : Vortex Pinning Measurements in YBCO

Pinning plays a particularly important role in superconductors for applications. High temperature superconductors, such as YBCO, are of particular interest for applications because they can be cooled using liquid nitrogen, which is much more economical than cooling with liquid helium. For this reason, I extended the pinning measurement technique developed in the preceding chapter to study vortex pinning in a YBCO thin film. There is more work to be done with YBCO, but the preliminary data I present here is an encouraging and educational start to a complete study of vortex pinning in the material.

7.1 Imaging at Liquid Nitrogen Temperatures

Operating the microscope with liquid nitrogen coolant presents two significant obstacles compared to operating with liquid helium. One challenge is that the thermal time constants of the system are very long, and the other is that it is more difficult to generate magnetic fields. To start, the thermal time constants of the system are much longer than those at liquid helium temperatures, such that cycling the temperature above T_c and cooling down to the measurement temperature is a very time consuming exercise. To heat the sample above T_c as quickly as possible, I operated the temperature controller in the open-loop control mode, and used a manual output of 35% with a power level of 7.7 W. I hesitated to send more current through the 42 SWG (~ 0.1mm) copper wires for fear of damaging them, although I never had any indications of a problem with this, so it may be possible to use even larger heater currents. To cool down, the temperature controller setpoint was set and the temperature was allowed to fall to the desired value. To speed this process, I occasionally added helium exchange gas to increase the cooling power, after having turned off all high voltages in the system to avoid problems with arcing. This was only done when taking data manually. The MFM was automated to take the depinning measurement data, in which case exchange gas was not used. One issue to be aware of regarding cooling the sample and cantilever is that the cantilever and sample temperatures take a long time to reach the temperature of the temperature sensor. This can be monitored by tracking the cantilever frequency vs time. T vs t and Δf vs t curves are illustrated in Figure 7-1. A temperature cycle in which helium exchange was used is illustrated in Figure 7-6B.

A second issue when operating with liquid nitrogen is that applying a magnetic field is much more difficult. Usually, I generate fields using the system's 5 T superconducting magnet, but in liquid nitrogen this magnet is no longer superconducting. Small currents can be driven through the magnet, however a large percentage of that current is shunted through the persistent current switch, such that you do not know how much current is actually flowing through the magnet and thus you do not know how much magnetic field you are generating. In Section 7.3 I have estimated the field based on vortex images as a function of the total current in the magnet and switch.

The data shown in this chapter were obtained using a MikroMasch NSC18 cantilever, which is similar to the DP18-Sting cantilever used in the previous chapter, except that it has a standard conical tip rather than an EBD tip. The cantilever had a resonant frequency of 82.1 kHz, a spring constant of 4.0 N/m, and a Q of 75000 at 78 K. The tip was coated in the Ginzton Microfabrication Laboratory with a 40 nm thick iron film, covered with a 7 nm thick gold film for protection against oxidation. A thin titanium film was again used as an adhesion layer.

7.2 YBCO Sample

The YBCO film I studied was grown by Rob Hughes in John Preston's lab at McMaster University. It is a 200 nm thick film grown by pulsed laser deposition (McConnell et al. 1994) on a $LaAlO_3$ substrate, with a T_c of 89.8 K as determined from a measurement of the resistivity vs temperature (Figure 7-2). An AFM image of the sample (Figure 7-3) taken by Rob Hughes shows a surface roughness of 5.8 nm_{rms}. I chose to study this sample because of its relatively smooth surface (compared to other YBCO samples I had access to), and the lack of pinholes in the material. My first attempts to image vortices were made using a YBCO film from Conductus. This film had a large number of pinholes, which made imaging difficult due to the large topography signal they created. It was difficult to distinguish between a vortex and a pinhole, particularly at the time when I was still learning how to operate the microscope.

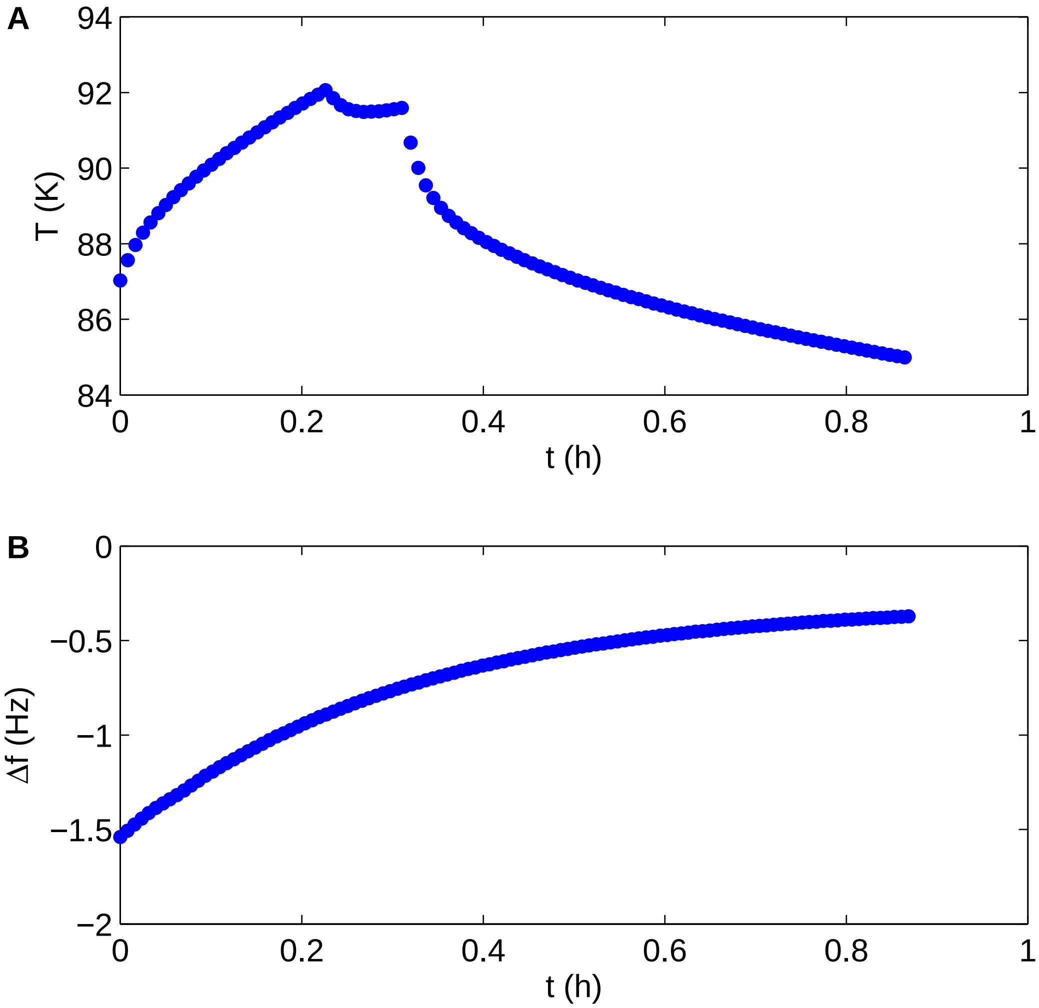

Figure 7-1: Temperature cycling at liquid nitrogen temperatures. (A) The thermal time constants of the microscope are very long at liquid nitrogen temperatures. Also, the temperature sensor reading is not necessarily an accurate measure of the sample temperature. To generate new vortices, I heated to a reading of 92 K and (roughly) maintained that temperature for 5 minutes before cooling, to ensure that the sample went completely normal. (B) The cantilever frequency as a function of time, with the thermometer temperature controlled at 85.0 K starting from t = 0. After cooling, the cantilever frequency drifts for a long time, indicating that the cantilever temperature is changing.

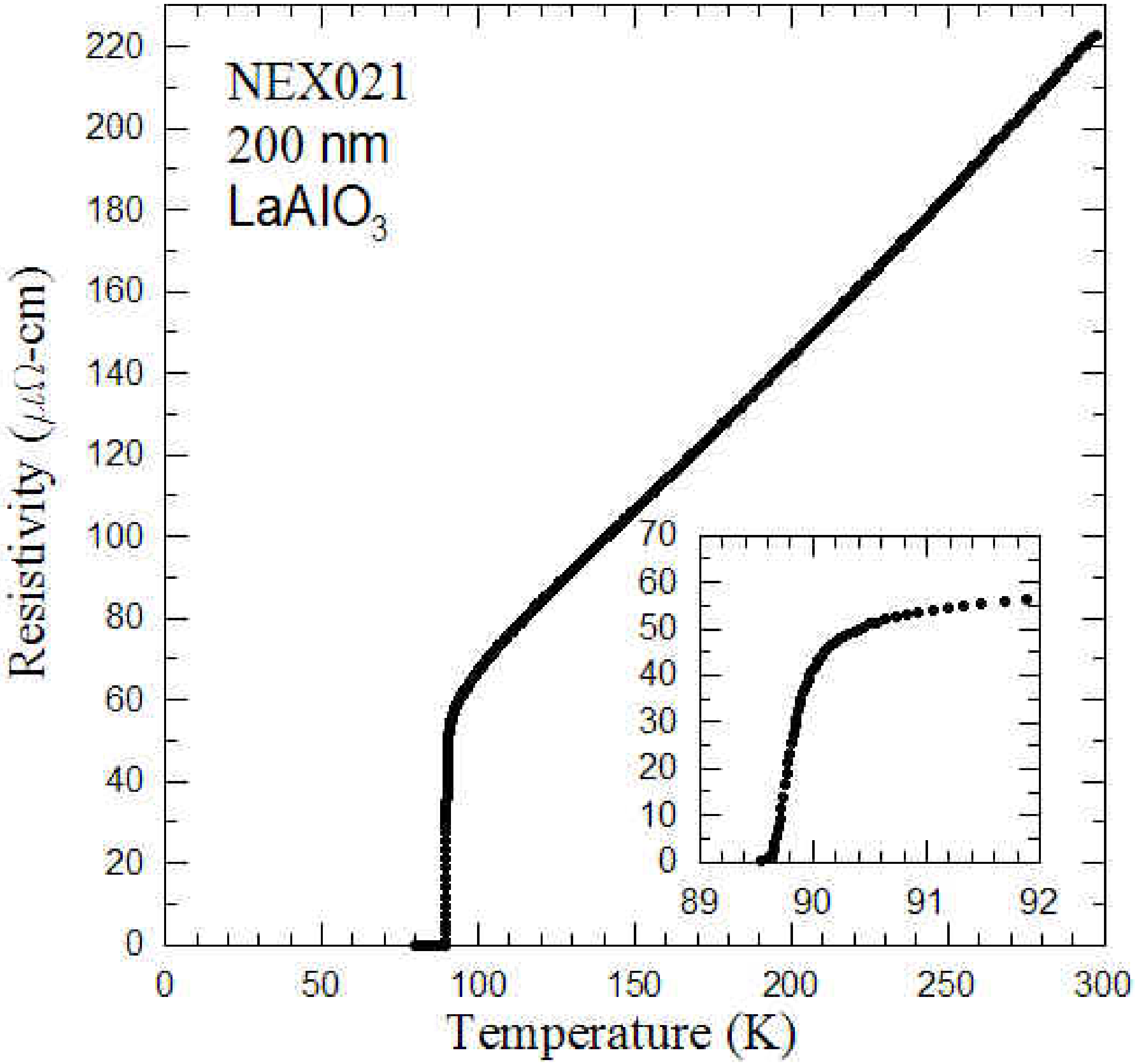

Figure 7-2: The T_c of the YBCO film studied was determined to be 89.8 K from a measurement of the resistivity vs temperature. The data was taken and plotted by Rob Hughes.

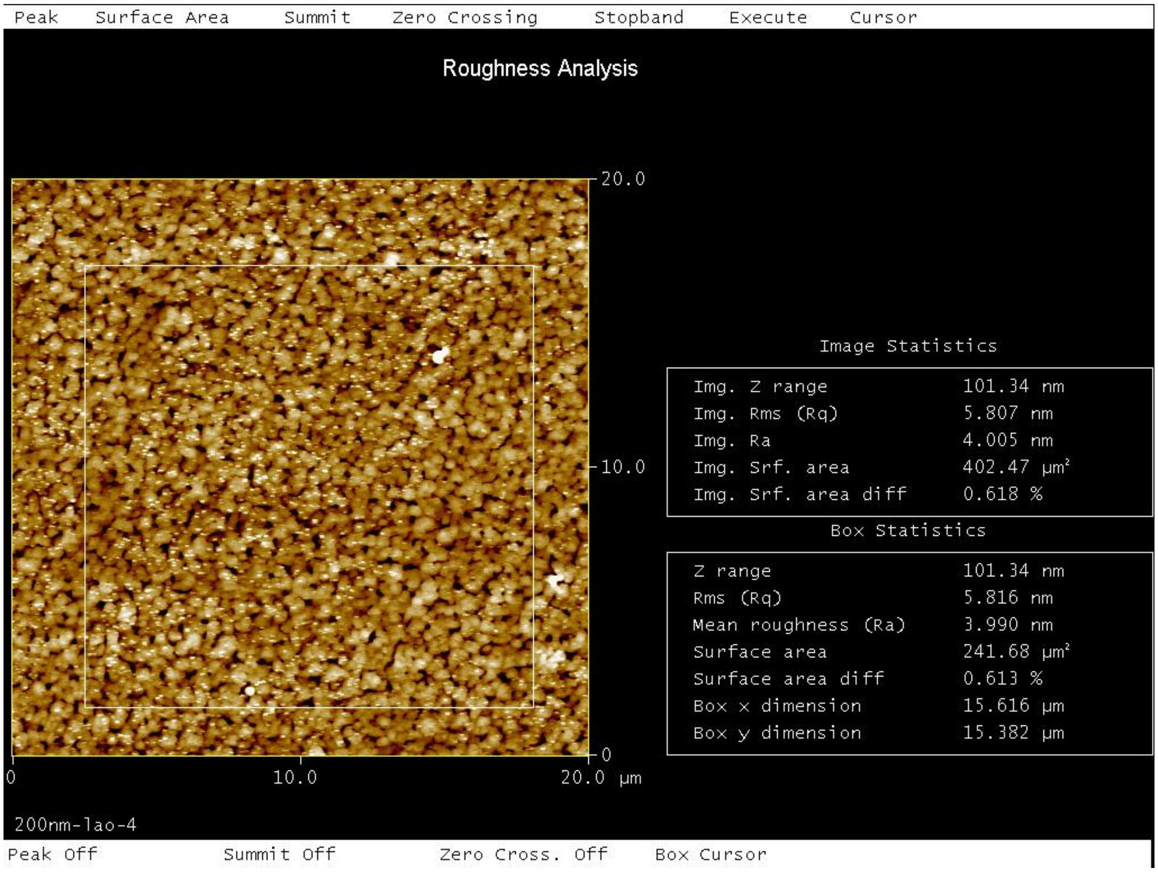

```
Image Statistics
Img. Z range               101.34 nm
Img. Rms (Rq)              5.807 nm
Img. Ra                    4.005 nm
Img. Srf. area             402.47 µm²
Img. Srf. area diff        0.618 %
Box Statistics
Z range                    101.34 nm
Rms (Rq)                   5.816 nm
Mean roughness (Ra)        3.990 nm
Surface area               241.68 µm²
Surface area diff          0.613 %
Box x dimension            15.616 µm
Box y dimension            15.382 µm
```

Figure 7-3: An atomic force microscope image of the surface of the YBCO film I studied shows an rms surface roughness of 5.8 nm. Rob Hughes of McMaster University grew the film and measured this AFM image.

7.3 Imaging Vortices

For the first attempts at imaging vortices in YBCO, I took MFM constant height scans after cooling through T_c while flowing a current through the magnet using a Valhalla current source. The images are shown in Figure 7-4. In Figure 7-5, a plot of N_{vortex} vs I_{total} (where $B_{applied} \propto I_{total}$) shows a linear dependence, again as expected from Equation (5.1). The actual magnetic field can be estimated from Equation (5.1) and the measured scan range of the piezotube at 78 K:

$$\begin{aligned} N_{vortex} &= \frac{BA}{\Phi_o} + const \\ &= \frac{R_{magnet} C_{magnet} A}{\Phi_o} I_{total} + const \end{aligned} \tag{7.1}$$

where $C_{magnet} = 659.6\,G/A$ is the magnet coil constant, and R_{magnet} is the fraction of I_{total} that actually goes through the magnet. The slope of the N_{vortex} vs I_{total} gives a value of 0.22 for R_{magnet}, such that when operating the magnet in liquid nitrogen $B_{applied} = 0.145 I_{total}$ where I_{total} is measured in mA and $B_{applied}$ is measured in G.

During the course of imaging vortices after cooling in different fields, I observed an interesting phenomena, illustrated in Figure 7-6. After cooling in a field and imaging vortices, the sample could be heated to around T_c and subsequently cooled again, and the original vortices would not completely disappear. In fact, if I cooled down in a field of the opposite sign, some of the original vortices remained, but also some new antivortices were generated. These antivortices and vortices did not all annihilate, the reason for which I admittedly do not have an explanation. For the purposes of the rest of the measurements presented here, the important point to take from this phenomena is that the sample temperature lags behind the thermometer temperature (in the same way Figure 7-1 showed that the cantilever temperature lags behind the thermometer temperature), and that to ensure that the superconductor goes completely normal before generating a new vortex arrangement, the thermometer temperature should overshoot T_c and one

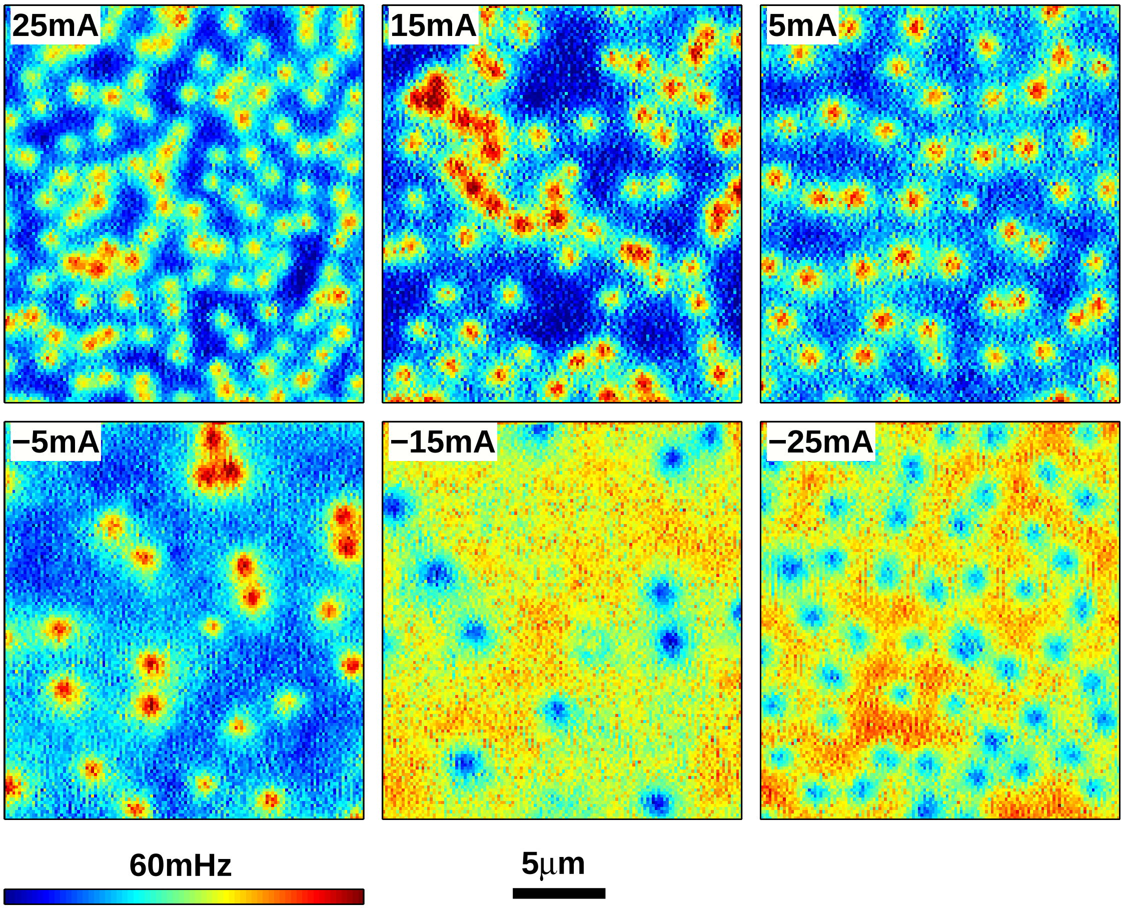

Figure 7-4: I successfully imaged vortices in the YBCO film after cooling in external fields generated by running various currents through the external magnet.

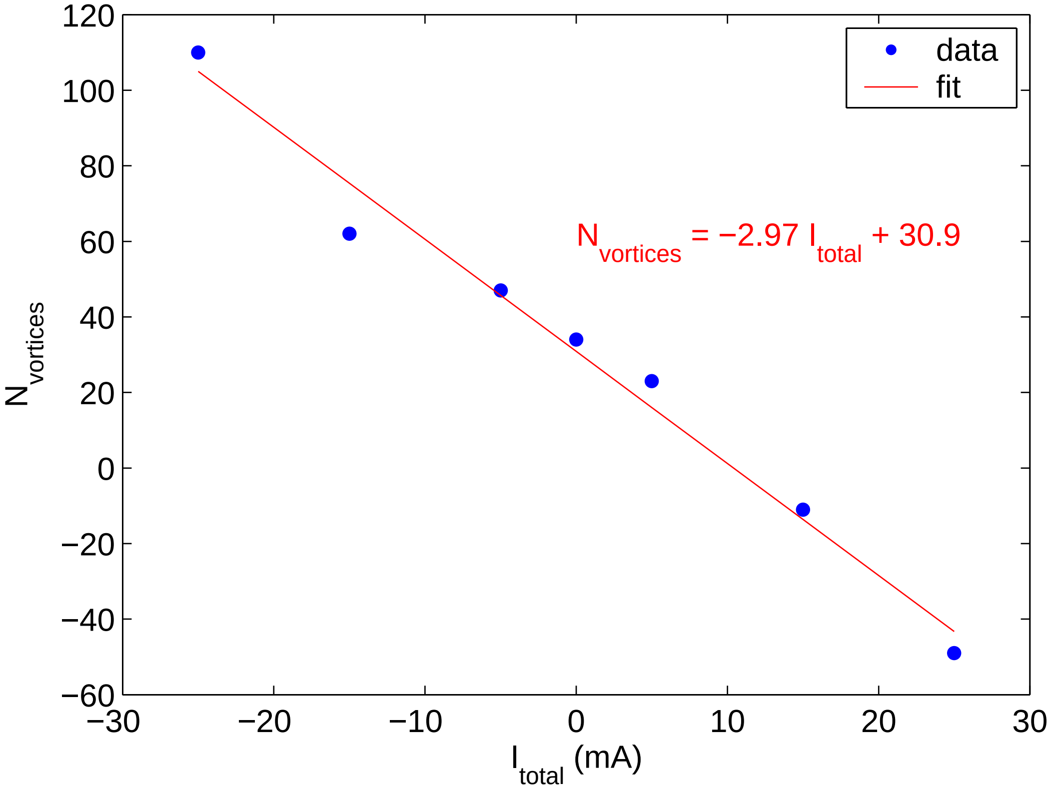

Figure 7-5: The number of vortices observed is linearly related to the current flowing through the magnet, which is proportional to the magnetic field. When operating the magnet in liquid nitrogen, it is not clear how much of the total current actually goes through the magnet and how much goes through the persistent current switch. An estimate of the field generated by the magnet can be made from the slope of the fit. I found that 22% of the total current goes through the magnet, giving an effective conversion of 145 G/A.

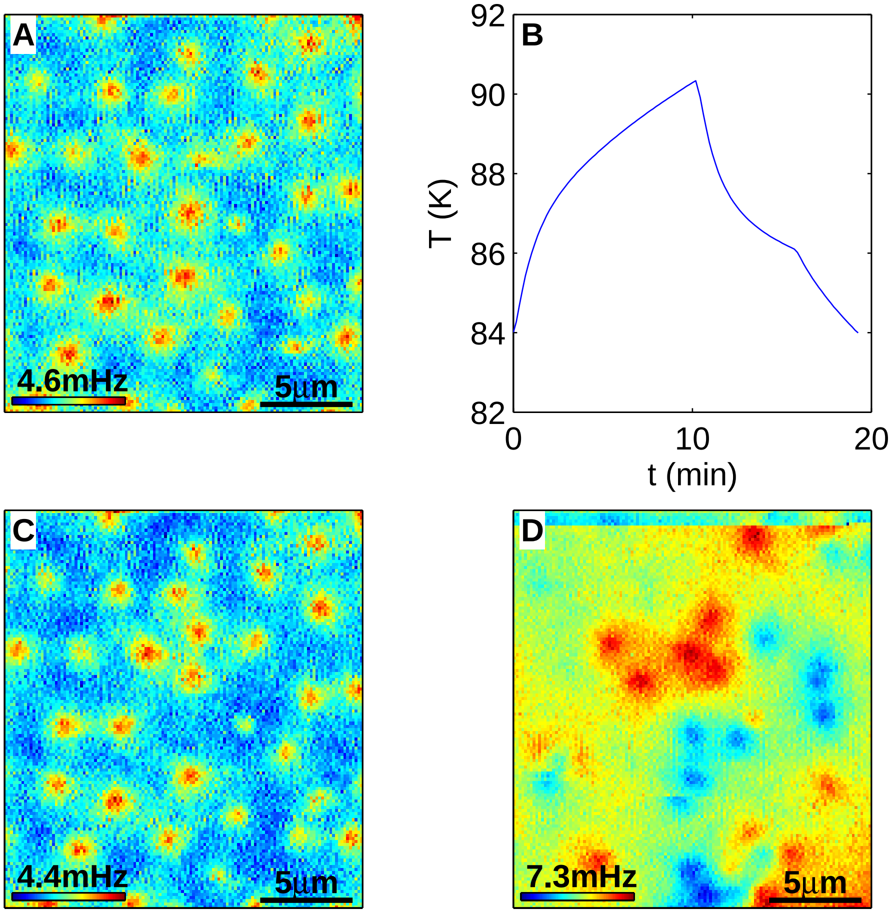

Figure 7-6: I observed antivortices and vortices in the YBCO film after short temperature cycles. (A) An initial configuration of repulsive vortices was generated by heating well about T_c and cooling with no external field (a small field is still generated by the magnetic tip, which was withdrawn from the surface). (B) The temperature (at the thermometer) was cycled to 90 K and back down to 84 K in an external field of –1.5 G (giving a total field of about zero). (C) Vortices are again visible in an MFM image, located in positions largely well matched to A. (D) The temperature was cycled again as in B, and the sample was cooled in a -3 G field, which would generate vortices of the opposite polarity compared to A. Attractive and repulsive vortices were simultaneously imaged in the film.

should wait a few minutes to be sure the sample temperature is sufficiently high before continuing.

One other point to note in Figure 7-6E is the sudden jump in frequency between two scan lines near the top of the image. I believe that this is due to an unstable wobble in the coarse approach screw causing a shift in the scan height. This problem was a new development that was not present in previous data sets shown in this thesis. The coarse approach screw had seized in an attempted cooldown just prior to this YBCO run, and after being repaired, the screw was unfortunately relatively loose for use in a high resolution scanning microscope. Movement of the piezotube would occasionally cause the screw and/or kinematic mount to shift. However, it was generally possible to obtain images without this problem occurring by changing directions smoothly, and slowly for large position changes.

I also obtained images of vortices at various temperatures, as shown in Figure 7-7. Vortices were readily observed at low temperatures (around 80 K), but were difficult to observe near T_c as the vortices spread out and the signal strength decreased.

7.4 Depinning Measurements

I measured the probability of depinning vortices in the YBCO film using the same procedure as used in Section 6.2 with the Nb film. In the case of the YBCO measurements, after a temperature cycle to generate a new arrangement of vortices, the frequency was monitored until the standard deviation of the 10 most recent measurements was less than 1 mHz, to ensure that the cantilever was at a steady temperature. Ideally this temperature matched the thermometer temperature, but it is quite possible that there was some error present in the reading of the cantilever and sample temperatures. Once the frequency was stable, a depinning measurement was carried out as in Figure 6-4.

The signal to noise ratio in the images obtained was fairly low, and it tended to be difficult to identify vortices definitively. This is due to the fact that the depinning measurements were largely obtained at and around 85 K, at which the penetration depth is large and thus the force gradient from the vortex is small. It is likely also due to tip damage which I believe occurred between the time when the images shown previously in this chapter were taken and the time at which the depinning measurements were carried

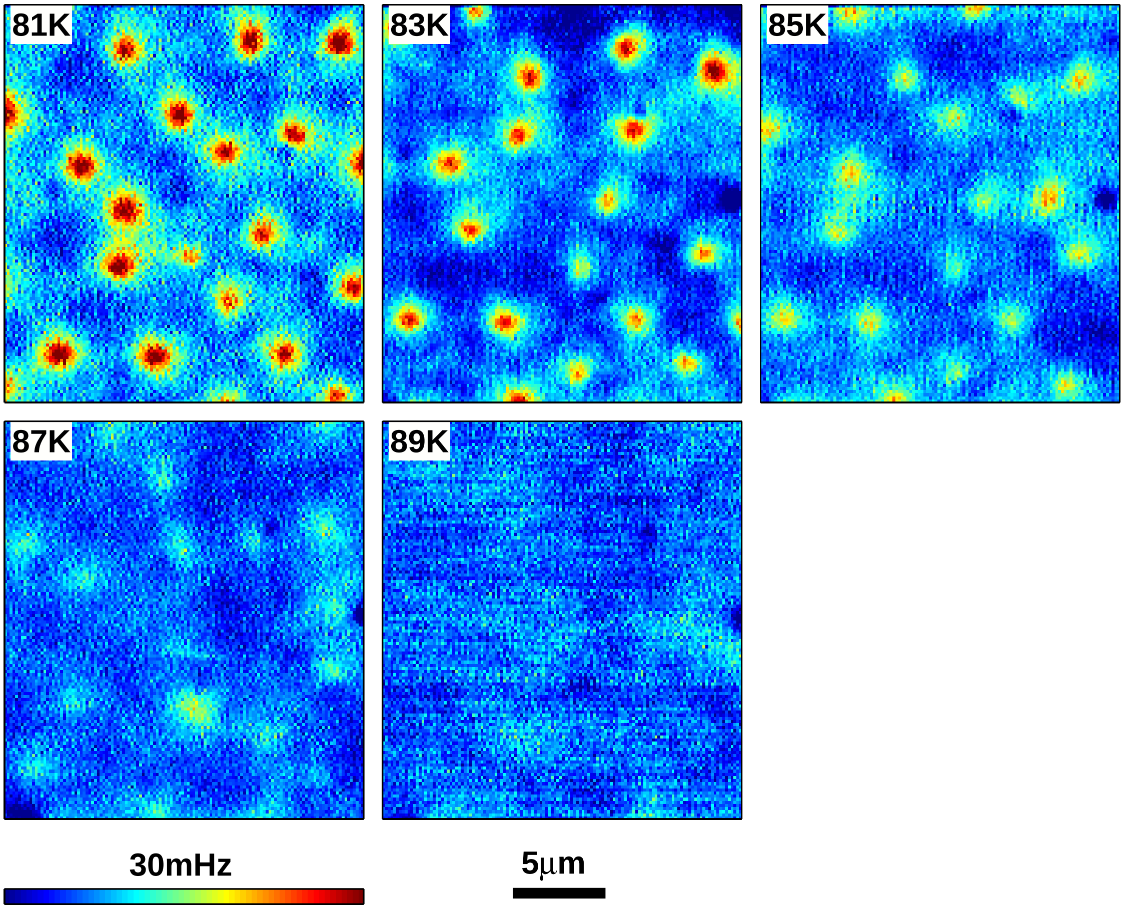

Figure 7-7: Images of vortices in a 200 nm thick YBCO film at various temperatures. At higher temperatures, the signal strength decreases due to the vortex spreading out, and as the sample's T_c of 90 K is approached, vortices are no longer visible.

out. This damage would reduce the magnetic moment of the cantilever tip and thus would reduce the measured signal.

To improve the image quality, it was necessary to do a plane subtraction on the data, despite the fact that the scans were obtained using the constant height imaging mode. This could be due to inaccurate coefficients, or it may also have been due to some remaining frequency drift during the time of the scan. Following the plane subtraction, the image quality was further improved using the filtering technique illustrated in Figure 7-8. First, the raw data was Fast Fourier Transformed to identify the signal and the noise. The signal is contained at the center of the FFT, while the noise is contained around the edges. To reduce the noise level, the FFT was convolved with the Gaussian illustrated in Figure 7-8C. The signal at the FFT center is multiplied by 1, and the noise at the outer edges by 0, with a Gaussian falloff in between. This convolution results in the filtered FFT shown in Figure 7-8D. The signal has been retained, while the bulk of the noise has been eliminated. After a reverse FFT, the filtered image, shown in Figure 7-8E, shows the vortices much more clearly compared to the unfiltered image of Figure 7-8A.

To analyze the probability of depinning, vortices in the before and after images were identified manually, as the automated vortex finding routine used in Nb was insufficient to reliably identify vortices in the YBCO images. The center positions were determined by fitting Gaussians to vortices in the images taken before and after the depinning scan. Vortices in the "before" images for identical depin parameters with a center positioned 200 nm or more inside the field of view were summed to determine $n_{initial}$. A vortex was considered to have depinned if the new center location was 200 nm or more (200 nm is slightly more than the size of a single pixel in the images) away from the initial position. As for the Nb measurements, the surface position was measured at the beginning and end of a depinning measurement set, and data sets for which the difference between the touchdowns exceeded 25 nm were discarded.

The results of the YBCO depinning measurements are illustrated in Figure 7-9 and Figure 7-10. As for the Nb measurements, the depinning probability increases with increasing temperature, and an exponential relationship is observed for low probabilities. The depinning probability also increases with decreasing tip sample separation and thus increasing force as one would expect. The temperature dependence of the pinning energy

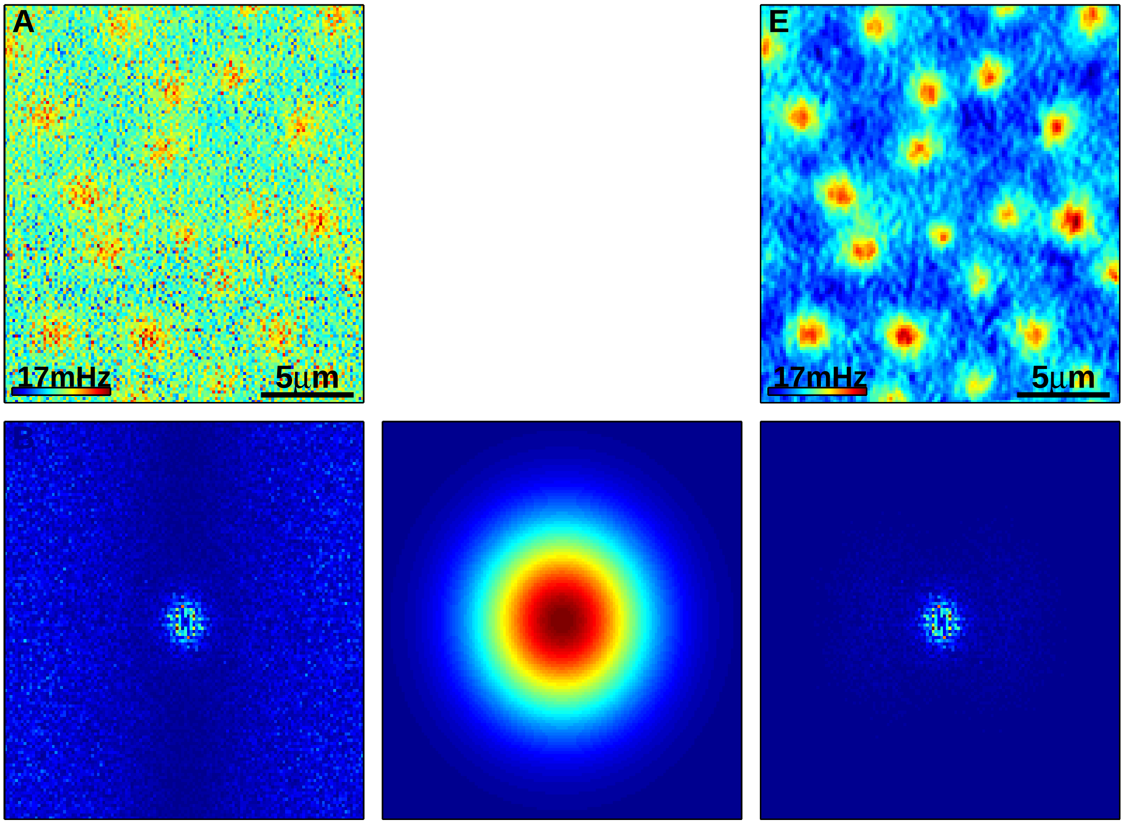

Figure 7-8: Images of vortices in the YBCO film were filtered by convolving the Fourier transformed image with a 2D Gaussian. (A) Vortices are visible in the raw data, but the noise level is quite high. This image was obtained at a scan height of 650 nm, and a temperature of 84 K. (B) The 2D FFT of the raw image data. The real signal is contained in the bright area in the center of the FFT, while the noise is in the areas towards the edges. (C) A Gaussian filter is used to remove noise from the image. The Gaussian has a value of 1 at the center, and 0 at the edges, with a Gaussian falloff in between. Convolving B with C leads to (D), the filtered FFT. Much of the noise has been removed by the filter, while the signal remains at the center of the FFT. (E) After transforming the filtered FFT back into real space, vortices are much more readily visible. This filtering technique was used to analyze the images for depinning measurements, but was not used in the images shown in the images preceding this figure.

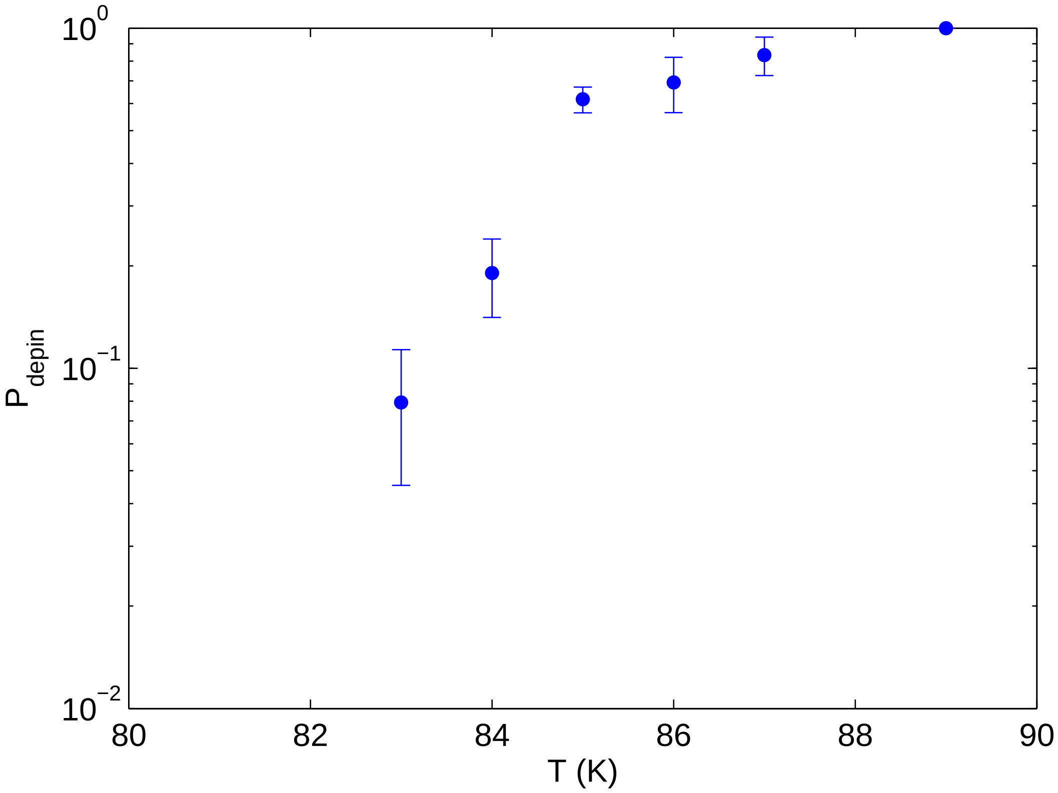

Figure 7-9: The probability that a vortex will be depinned was measured as a function of temperature at a scan height of 200 nm. Similar to the Nb data, an exponential relationship is observed at low depinning probabilities.

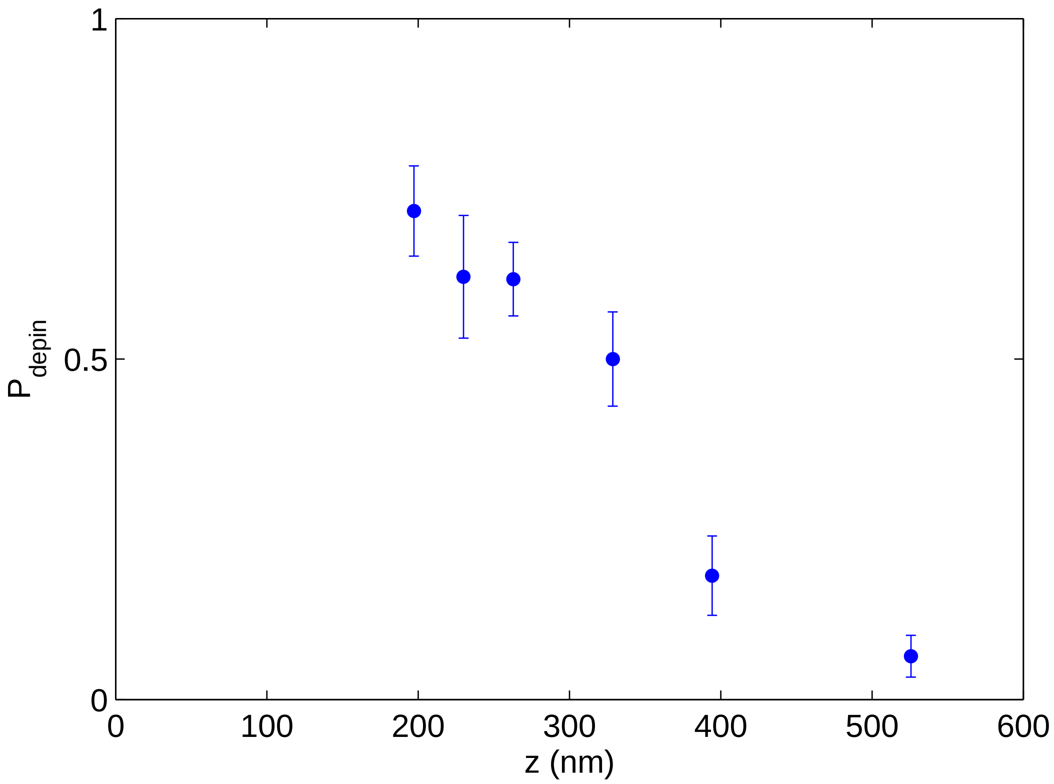

Figure 7-10: The probability of depinning a vortex was measured as a function of scan height at a temperature of 85 K. Lower scan heights give increased forces on the vortices, thus the depinning probability increases.

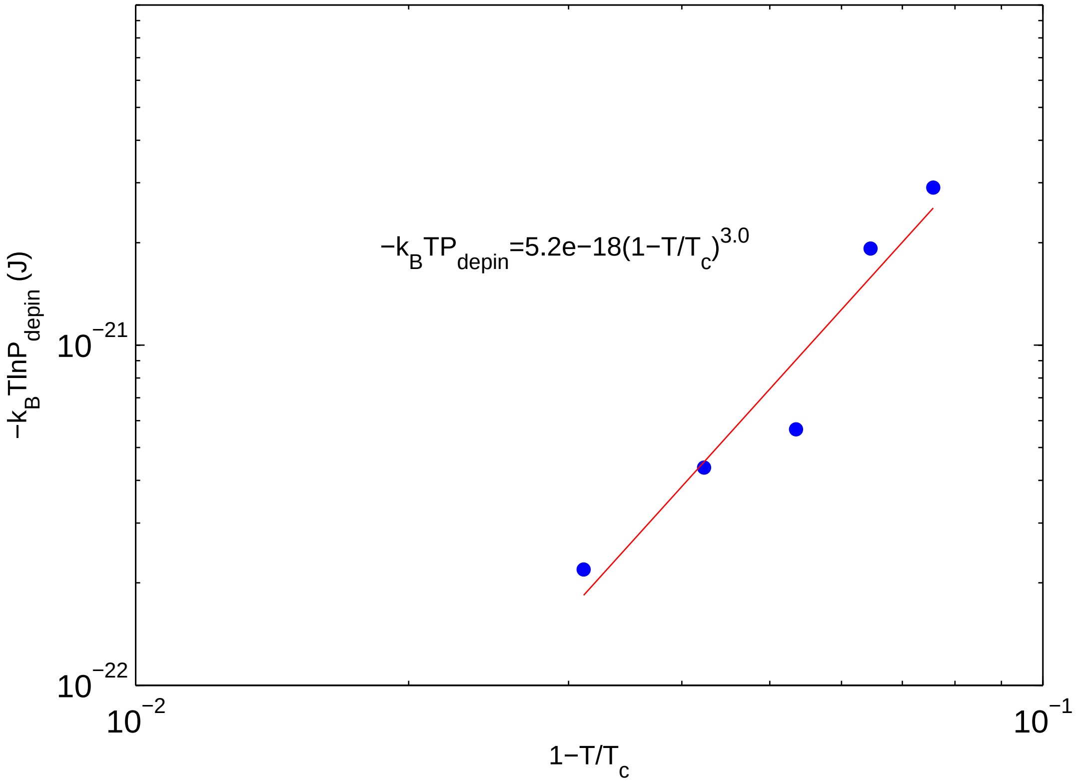

Figure 7-11: The temperature dependence of the pinning energy can be estimated by fitting $-k_BT\ln P_{depin}$ as a function of $1-T/T_c$. As for the Nb film, the energy in the YBCO film is described by $\left(E_{pin}-Fx\right)\propto\left(1-T/T_c\right)^3$.

can also be estimated as described by Equations (6.4) to (6.7). From Figure 7-11, for the YBCO film studied here $U(0) = 5.2\times10^{-18} J$, and $n = 3.0$.

Unfortunately, I was not successful in estimating the force on a vortex using the technique presented in Section 6.3. I found that it was difficult to obtain useful images at low scan heights, because for small vibration amplitudes the noise level was too high, and for large vibration amplitudes the tip struck a variety of topographic features during the scan, ruining the images. Some of the topographic features are likely to have been dirt on the surface (the sample had been exposed to lab air several times due to failed cooldowns, caused by seizure of the coarse approach screw for example), and perhaps even some fragments of the tip from early part of the run, rather than features of the film itself. I don’t believe that the YBCO film is so rough that it would prevent one from obtaining good measurements within 100 nm of the surface, and these measurements should be revisited in a future experiment.

7.5 Next Steps

The depinning measurements described in the previous section are encouraging preliminary measurements, but could be improved upon. To repeat the experiment, I would likely choose to use a cantilever with a stronger magnetic tip (a thicker magnetic film). This would allow for doing the depinning measurements at a slightly lower temperature, closer to 80 K, which would improve the signal to noise ratio for imaging and would thus make analysis of the measurements (i.e. identifying vortices and fitting to find their centers) easier. The signal to noise ratio could also be improved by using a cantilever with a lower spring constant than the 4 N/m cantilever I used, although issues with tip snap-in would have to be considered. Scans at a number of different heights should be obtained, in order to determine the force gradient as a function of height for integration for a force estimate. Images should be obtained at heights slightly larger than where vortices are first visible, in order to improve the estimate of the contribution from the large separation force gradients to the overall force. The separation between vortices should be sufficiently large that there is negligible overlap between the magnetic fields of the vortices.

Following a force measurement, a study of depinning should be repeated. A full study needs to be carried out with the same cantilever, because differences between the magnetic properties of different tips would complicate the analysis. It would also be a good idea to repeat the force measurement at the end of the depinning study, to ensure that the force is the same as at the start of the run and check that the tip was not damaged during the run.

In the long term, it would be interesting to explore the possibility of directly measuring the radial force on the vortex using vertically oriented cantilevers (Stowe et al. 1997).

Chapter 8 : Conclusions

For this thesis, I have constructed a low temperature magnetic force microscope, and have used it to study vortices in Nb and YBCO. In particular, I have manipulated individual vortices in a Nb thin film to form the initials "SU" for Stanford University, and have used the manipulation capability to study vortex pinning in Nb and also a YBCO thin film. I have also studied the magnetic properties of chemically synthesized cobalt nanomagnets using the technique of cantilever magnetometry.

The microscope I constructed is based on a design by Dan Rugar. It uses a fiber optic interferometer with a displacement sensitivity of about $5x10^{-3}$ Å/$Hz^{1/2}$ as the deflection sensor. I operated the microscope in the frequency modulation detection mode, and measured a force gradient sensitivity of $1.4x10^{-7}$ N/m. This was achieved using a MikroMasch DP18-Sting cantilever with a resonant frequency of 81 kHz and a spring constant of 4 N/m. I also filtered the frequency shift signal with a 100 Hz low pass filter, and averaged for 20 ms. The sensitivity is limited by interferometer noise as demonstrated by the fact that the frequency shift noise level increases with increasing modulation frequency. The interferometer noise is limited by shot noise in the interferometer.

I carried out cantilever magnetometry measurements on cobalt nanomagnets with a diameter of 9 nm, with the long-term goal of using the nanomagnets as magnetic tips on MFM cantilevers. Measurements of the frequency shift in a 1.6 T magnetic field as a function of the field- cantilever angle were obtained, and were modeled for a hard axis perpendicular to the cantilever surface. The model matched the data reasonably well for an anisotropy field of –0.47 T, but the field dependence was not consistent with the model. Hysteresis measurements on the nanomagnets showed some small hysteresis at 8 K, but at temperatures of 20 K and higher the magnetic signal had largely disappeared. I believe this is due to the fact that the data were obtained using nanomagnets which were produced 7 weeks prior to being measured. The particles may have oxidized such that the magnetic portion of the particle was effectively smaller and the moment and anisotropy were reduced. The weak magnetic signal indicated that the particles are probably not suitable for use as MFM tips, particularly given that it is very difficult to attach a single nanomagnet to a cantilever tip and thus oxidation is likely to occur in between the time of production and the time at which the cantilever is prepared and aligned in the system. However, the magnetometry technique is a useful one for characterizing magnetic materials with strong anisotropy.

The magnetic force microscope I constructed for this thesis has proven to be a powerful tool for studying vortices in superconductors. I successfully imaged vortices in both a Nb and a YBCO thin film, at a variety of fields, temperatures, and scan heights. I also demonstrated the ability to manipulate individual vortices, first by constructing an "S" with vortices in a Nb film, and a second time by arranging vortices in the form of an "SU". This work shows tremendous potential for magnetic force microscopy as a technique for manipulating individual vortices and for characterizing pinning at an individual vortex level, and could open up a range of new experimental possibilities, such as studies of vortex entanglement. As part of this thesis, I used this manipulation capability and developed a method for using MFM to characterize pinning strengths. I demonstrated the technique by examining vortex pinning in both Nb and YBCO. The probability of a vortex depinning was found to increase exponentially with increasing temperature, although it is not clear what this temperature dependence is due to. As a function of scan height, the probability increases as the height is decreased, since the force the MFM tip exerts on a vortex is greater at lower scan heights. The radial force is responsible for depinning vortices, but it is the vertical force gradient that I actually measure using the frequency modulation method. I have estimated the vertical force on a vortex in Nb by integrating the peak frequency shift (i.e. force gradient) over a vortex, and found that the force is on the order of 10 pN. The radial force is in theory related to the vertical force by geometrical factors, however these factors are not known for the tip I used.

For future depinning measurements, it would be advantageous to measure the force gradient at larger scan heights than I used. This would improve the force measurement by eliminating or at least reducing the need to estimate the contribution of the long-range force gradient to the overall force. Also, I would recommend measuring the force both at the start of a run of depinning measurements, and at the end. This would provide a useful check to ensure that the tip was not damaged during the course of measuring the depinning, since the forces would be equal if the tip had not changed. The depinning measurement technique could be advanced even further by using vertical cantilevers to directly measure the pinning force, or by using calibrated MFM tips to obtain more quantitative results through more accurate modeling. Regardless, the technique has the potential to be a powerful new tool for characterizing superconductors intended for applications.

This page intentionally left blank.

Appendix A: MFM Setup and Imaging Procedures

This section outlines the operating procedures for the magnetic force microscope constructed for this thesis. The procedures are by no means suggested to be the only or even the best ways for doing things, but are the methods used with the microscope to date. Undoubtedly improvements can and will be made to the instrument and the operation techniques, but I am hopeful that this section will provide some useful tips to new users. In the interest of keeping the length of this appendix manageable, the level of detail and description is kept to a reasonable level. As such, this appendix may not be particularly readable for someone who is completely unfamiliar with the microscope setup. However, it should help in getting started. Please note however that this section has not been rigorously edited, so use some caution when following the directions and do what makes sense. Also, note that changes to the instrumentation and programming are likely to have been made since the time of this writing. Recommended values for parameters such as pressures and temperatures (for example, the pressure to pump down to before cooling down) are suggestions only, the user should feel free to adjust them as feels comfortable and as is found to lead to successful runs. I would like to thank Jenny Hoffman for her help in developing an MFM user manual. A more complete and recent set of instructions that she has put together can likely be found in the lab, but in the event it is not available this appendix will serve as a more permanent, easily located record.

Like all cryogenic scanning microscopes, the magnetic force microscope is a complicated instrument to operate. It is inevitable that mistakes will be made, even with an experienced operator. A new user should not be afraid to run the microscope however. A few particularly costly mistakes are listed in the proceeding section, otherwise most of the common and foreseeable mistakes that can be made will result in the end of a particular cooldown but not the end of the microscope itself. Try not to do anything too stupid, but otherwise don’t be afraid to give things a try and learn as you go.

A.1 Serious Mistakes

There are a few mistakes that one could conceivably make that would result in a need for significant repairs to the microscope and accordingly a significant loss of time. These mistakes should be avoided.

Most mistakes will result in damage to the cantilever and/or the sample, both of which are generally easily replaced upon warming up the microscope (although in the future it is likely that rare samples will be examined). Damage to the piezotube and the optical fiber is more serious, because of the time involved in repairing or replacing these items. Destruction of the piezotube would be particularly costly, since a separate cooldown would be necessary to calibrate the scan range. The proceeding list covers the mistakes which have a reasonably likely chance of occurring and would damage either of these items.

a. Take care when handling the optical fiber. The end can be easily damaged when inserting the fiber rod into the various slots for holding it. Make sure to insert it straight, and with steady hands.
b. After inserting the fiber rod in a slot, make sure to secure it well with the designated screws so that it doesn't drop out.
c. Don't vent the MFM or add exchange gas when the high voltages are on. Arcing will likely occur, and the piezotube and/or interferometer adjustment piezo could be damaged or destroyed. Correspondingly, don't turn the high voltages on when there is exchange gas in the instrument.
d. Don't turn the coarse approach screw too far. Doing so will certainly destroy the cantilever, and could also break the piezotube. This can be an easy mistake to make when using the stepper motor. As a safety feature, the *stepdeg.m* program will ask you to confirm a large step decreasing the tip-sample separation. There is a large red Stop button on the stepper motor controller which can be used in the event of an emergency.
e. Following on point d, use the coarse approach program (*coarseapp.m*) if you are not yet sure what the distance is between the cantilever and sample. Be careful though that the programmed voltage level for detecting a touchdown is appropriate. The Nanosurf FM Detector should be set to "Tip Guard" so that if the cantilever signal is

lost (e.g. during a touchdown/snap-in event), the Output will rail at 10V (check that the polarity is set properly for this condition). If an SR560 (or similar) preamplifier is used to filter and amplify the Output signal, the maximum voltage out of the preamp will be around 3V if the gain is 1. If the programmed voltage level is set to 5V, the program will continue to turn the screw even after the cantilever has been broken. Be sure that the programmed voltage level and the maximum voltage into the DAQ are compatible.

A.2 Timing

The MFM is not a fast turnaround instrument. Once a user has some experience with the microscope though, the turnaround time can be minimized with good planning and some luck. Nitrogen gas should be flowed through the vacuum space when it is open to air to prevent water from accumulating on the surfaces in the microscope. Also, cantilevers should be prepared ahead of time (tips coated, and cantilevers epoxied to the triangular mounts). The following schedule can then be followed:

a. Align the optical fiber to a cantilever, and the cantilever to a sample, in the morning. This takes about 1-2 hours for an experienced user, if all goes well.
b. Start pumping on the microscope before lunch.
c. After about 2-3 hours, the pressure should be close to 10^{-5} Torr. Calibrate the interferometer and characterize the cantilever properties.
d. Fill the dewar with liquid nitrogen to the desired level. Avoid overfilling the dewar to minimize the time needed to blow out the nitrogen. Use exchange gas for faster cooling if a particularly fast cooldown is desired.
e. In the late evening (or earlier if exchange gas was used), measure the interferometer and cantilever properties again, and then blow out the nitrogen.
f. Fill the dewar with liquid helium to a level of 40-50%. The microscope can then cool overnight.
g. In the morning, characterize the interferometer and cantilever at 4K.
h. Begin the experiment.
i. If the experiment is not successful (e.g. if the cantilever breaks or is not functioning as needed), blow out the liquid helium.

j. Follow the warmup procedure in Section 3.1.2.
k. Make the necessary changes and return to step a.

A.3 Initial Setup and Alignment

A.3.1 Cleanliness

Always use gloves when handling components that will be inside the vacuum. Also, use only clean tools designated specifically for use with the MFM, and work on cleanroom wipers or aluminum foil. All components should be kept clean, and new components and tools should be cleaned thoroughly before use. I typically use the following procedure to clean new parts:

a. Wash the part by hand with soap and rinse well with distilled water. This is particularly helpful with parts from the machine shop which have oil on them.
b. Ultrasound the part in soapy distilled water for 5 minutes.
c. Ultrasound in acetone for 5 minutes.
d. Ultrasound in methanol for 5 minutes.
e. Rinse in methanol or isopropanol from a squeeze bottle.
f. Dry the part using the nitrogen gun.

Steps c-f should be done in a fume hood. Samples can also be cleaned using the above procedure, beginning at step c.

A.3.2 Mounting a Sample

a. The sample holder can accommodate a sample with a size up to about 5mm x 5mm. If the sample is too large, a small piece should be cleaved for use with the MFM.
b. If necessary, clean the sample. A suggested procedure is listed above in Section A.3.1.
c. Attach to the sample holder using silver paint. The silver paint should cover an edge of the sample to make electrical contact between the sample surface and the electrode on top of the sample holder.

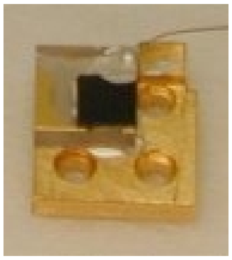

Figure A-1: The sample can be attached to the sample holder using silver paint.

d. Once the silver paint is dry, the sample holder can be attached to the piezotube using three 0-80 socket head cap screws. Stainless steel screws are used here for better thermal expansion matching with the copper sample holder.

Figure A-2: Copper braid is used for heat sinking the sample and the cantilever.

e. A copper braid for heat sinking can then be attached to the sample holder and the heater block.
f. Finally, the wire from the sample holder surface should be connected to the appropriate SMB connector to allow for the application of voltages to the sample holder and sample surface

A.3.3 Mounting a Cantilever

a. Epoxy the cantilever to one of the triangular titanium mounts using EpoTek H20E. Ensure that the position of the cantilever on the mount will allow for alignment of the interferometer optical fiber within the limits of the alignment setup. Cure on a hotplate at 80ºC for about 2-3 hours.
b. Remove the fiber bender holder from the cantilever holder by unscrewing the three 6-32 screws from the back of the assembly.

c. Mount the cantilever on the fiber alignment assembly using three titanium 0-80 socket head cap screws. The setup illustrated in Figure A-3 can be used to facilitate mounting, and is helpful for reducing the risk of mishandling and breaking the cantilever.

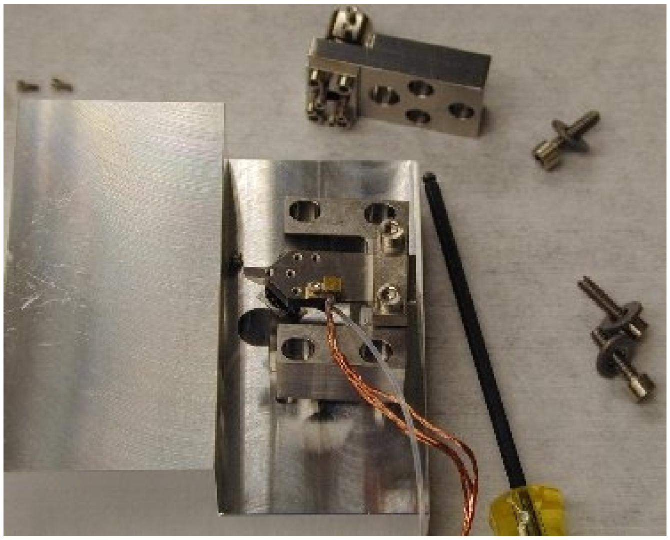

Figure A-3: The setup for mounting a cantilever.

d. Attach the copper braid used for heat sinking the cantilever.
e. Magnetize the cantilever using a strong magnet, such as one of the NdFeB rare earth magnets available in the Moler lab.
f. Reassemble the cantilever-fiber aligner with the three 6-32 screws and washers.
g. Mount the assembly vertically on the bottom of the MFM head using two long 6-32 screws, as shown in Figure A-4.

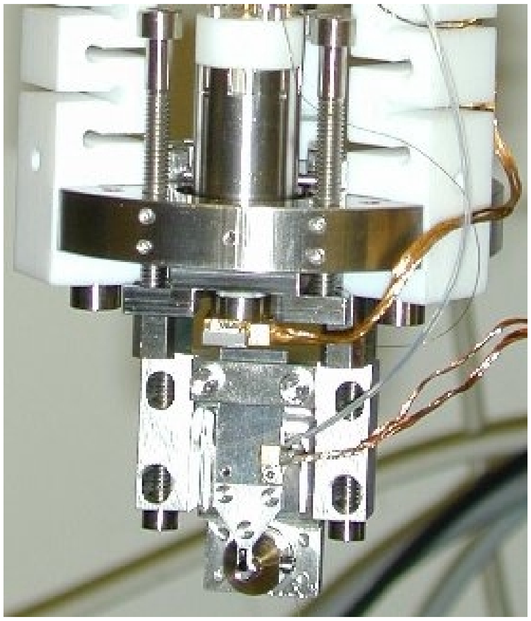

Figure A-4: The cantilever holder-fiber aligner assembly should be mounted vertically at the bottom of the MFM head for the alignment procedure.

h. Connect the piezo wire to the SMA connector.
i. Insert the optical fiber rod into the alignment bender, taking care not to damage the end of the fiber. The fiber end should be close to the cantilever, but not so far as to risk damaging it during the following coarse adjustment step. Tighten one of the 0-80 screws to hold the fiber rod in place.

A.3.4 Interferometer Fiber Alignment

a. Push the cantilever slightly away from the optical fiber using the 8-80 fine pitch screw. This is to give room for fine approach of the cantilever to the fiber later.
b. Use the CCD camera with the zoom lens to view the cantilever and optical fiber from the front. Hold the alignment assembly with one hand, and loosen the three 6-32 screws in the back using the other hand and a ball driver. Position the fiber within about 100µm of the cantilever end, and tighten the screws.
c. Viewing the side of the setup with the CCD camera. Move the fiber closer to the cantilever by pushing the fiber rod, and tighten both 0-80 screws when it is in its final position.

d. The gain on the high voltage amplifier should be set to 60. If the piezo stack setup is used, the offset should be 0V, and if the piezo disk setup is used, it should be 400V.

e. Replace the batteries in the New Focus 2011 photodetector if needed. They should last about one month under constant use.

f. Set the gain on the photodetector to $3x10^3$.

g. Unshort the laser, and turn the current on the laser diode current source up to the desired level. For the PD-LD Fabry-Perot laser diode, the typical operating current is around 30mA. This should be adjusted slightly to give the lowest noise floor, and will occasionally need adjustment during operation.

h. Look at the cantilever and fiber from the front again with the camera. Use the four 0-80 fine adjustment screws at the back of the bender to align the fiber to the end of the cantilever.

i. Set the frequency of the function generator to 50Hz, and increase the amplitude until the interferometer signal has completely doubled over. The amplitude of the interferometer signal will then be independent of the fringe centering.

j. Maximize the amplitude of the interferometer signal by adjusting the fiber alignment with the 0-80 screws. Adjust the photodetector gain as needed.

k. Adjust the 8-80 screw at the back of the alignment assembly to bring the cantilever closer to the end of the optical fiber.

l. Repeat steps j and k until satisfied. The final fiber-cantilever separation is typically between 50 and 200μm.

m. Use a Po-210 alpha particle source to eliminate any static charge on the fiber and cantilever.

A.3.5 Sample Approach

a. Turn down the high voltage for safety.

b. Move the alignment assembly to the horizontal orientation as shown in Figure A-5. Loosely secure the assembly with four 6-32 screws. Position the tip over the sample area to be studied, and tighten the screws.

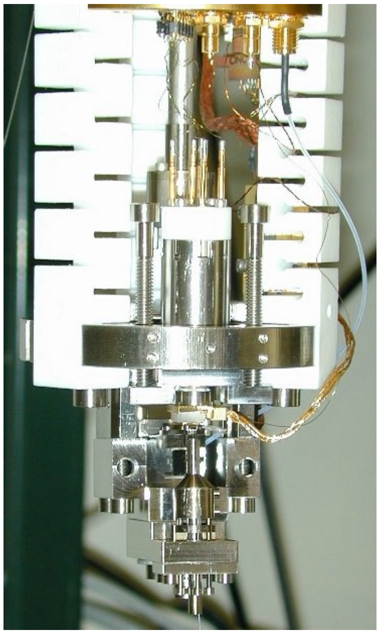

Figure A-5: The MFM head.

c. Attach the free end of the copper heat sinking braid to the temperature control block.
d. View the cantilever and sample from the side with the CCD camera.
e. The piezotube is attached to a kinematic mount, which rest on two 8-32 screws and one fine-pitch ¼-80 screw. Turn the 8-32 screws using a ball driver, and the ¼-80 screw using the stepper motor. Iterate between the three screws to bring the sample close to the cantilever. The sample surface should be parallel to the axis of bending of the cantilever, and the cantilever should be at roughly a 10º angle to the sample surface in the perpendicular direction.
f. When the tip-sample separation becomes small, angle the CCD camera so that the cantilever and its reflection in the sample surface are both visible. Continue adjusting the screws as needed, using the reflection to gauge the distance. The final steps should be done using the fine pitch screw and the stepper motor. Be careful to avoid crashing the tip into the sample surface.
g. If desired, a voltage can be applied to the z electrode of the scan piezotube to extend the tube and check for a cantilever touchdown on the sample surface. However, it is generally sufficient to bring the cantilever close to the surface, and then move on to the next steps.

h. Back off the fine pitch screw by at least 720º using the stepper motor to prevent the cantilever from contacting the sample during the process of moving the MFM into the dewar and cooling down.
i. Tighten the four 2-56 set screws to stabilize the 8-32 coarse approach screws and prevent vibrations and motion of the kinematic mount.

A.4 Pumping Down, Cooling Down, and Cantilever Characterization

A.4.1 Pumping Down

a. Scrape off any excess indium from the copper flanges on the MFM using a double-bevel wooden stick.
b. Attach the bottom vacuum can to the microscope using indium wire for the vacuum seal.
c. Remove the stepper motor from the top of the microscope, and replace it with the hoist bracket.
d. While floating the optical table on the air legs, use the hoist to move the MFM and lower it into the dewar. Once the MFM is in place, the air legs can be deflated.
e. Check the interferometer signal to ensure that the cantilever was not damaged while moving the MFM. Also, check that the heater and temperature sensor connections are all functional.
f. Connect the turbopump, and begin pumping down. With the main valve closed, start the roughing pump. Then, start the program *pumpdown.m* to track the pressure during the pumpdown. Slowly open the main valve, then start the turbopump. The pressure vs time curve should be compared to the typical pumpdown curves to determine if there is a leak. A dry-pump based leak detector could be used before moving the MFM to the dewar, but at the time of this writing there has never been a leak in the system so it is probably not necessary.
g. Remove the hoist bracket, and mount the stepper motor.
h. The pressure should reach the 10^{-5} Torr range before continuing. If nitrogen gas was flowed through the microscope while it was open to air, this takes approximately 2-3 hours. If the vacuum space was completely open to air (no nitrogen flow), pumping overnight is recommended before continuing.

A.4.2 Cooling Down

a. Turn down the high voltages. Put a 50Ω terminator on the BNC connection for the fringe piezo high voltage. “Short” the scan piezotube electrodes through 2MΩ resistors by flipping the switches on the breakout box. This is to prevent the generation of large voltages on the piezos as they contract during the cooldown.
b. Connect the cables for the temperature sensor(s) and heater.
c. Fill the dewar with liquid nitrogen. To completely fill the MFM dewar, roughly one full 160L dewar of liquid nitrogen is needed. However, when using the nitrogen to precool the instrument, less nitrogen may be used. Also, open the valves on the three flow meters (shown in) on the MFM dewar at the start of the transfer in order to clear any air out of the tubes.

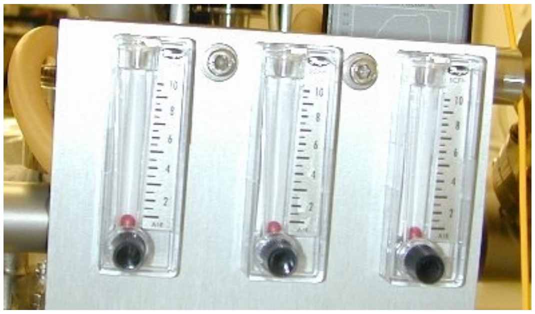

Figure A-6: The flow meters for the vapor-shielded magnet leads and for the dewar neck vent.

d. Exchange gas can be added to the vacuum space if faster cooling is desired. Close the main valve between the pumps and the vacuum space, and then add a controlled amount of helium gas using the double valve arrangement shown in Figure A-7. Generally exchange gas has not been used however and the microscope is allowed to cool slowly. This may help keep the cantilever cleaner.

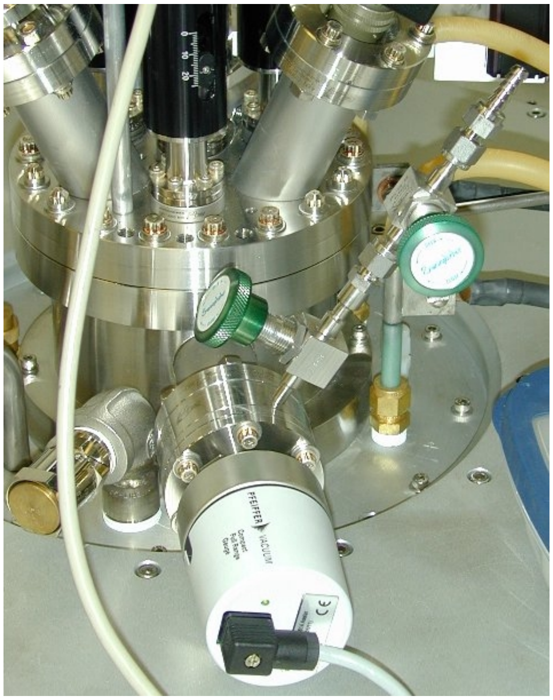

Figure A-7: The pressure gauge and the valves for flowing gas into/through the vacuum space.

e. Pump out any exchange gas.
f. Blow out the liquid nitrogen using nitrogen gas. The relief valve on the dewar bath should be held closed in some way.
g. Fill the dewar with liquid helium. For the initial cooldown, the dewar is typically filled to a level of 40-50%. This gives approximately one day of operating time in which to assess the state of the experiment. If things are working, more helium can be filled, and if not, the amount of helium that is wasted is minimized. Exchange gas may be used if faster cooling is desired.
h. The minimum helium level is 34%, at the top of the superconducting magnet. The helium boils off at about 10% per day above the 34% level, depending on the usage of the magnet. When the magnet is not in use, the break-away magnet leads should be disconnected to reduce the heat leak into the helium bath. If the magnet is not in use and the magnet leads are disconnected, it is possible to go one week between transfers.
i. Pump out any exchange gas.

j. When the microscope is cold, the pumps can be turned off to minimize vibrations if desired. Close the main valve, and turn off the pumps. Vent the pump lines with nitrogen gas. To pump on the microscope again, turn the pumps on and wait about 20 minutes (to reduce the pressure in the lines to the level of the microscope) before opening the main valve.

A.4.3 Coarse Approach

a. Center the interferometer signal on the fringe.
b. Set the cantilever frequency on the easyPLL software. Set the frequency offset to 0 and the output gain to 0.1. Turn the low pass filter on. Make sure that the “Tip Guard” feature is turned on.
c. Make sure that the manual offset on the scan piezo voltage is set to 0. The potentiometer is labeled such that 10 equals +10V (fully retracted), 5 equals 0V, and 0 equals –10V (fully extended).
d. Turn on the stepper motor controller axis. The indicator LED should be green.
e. Turn the scan voltage gain up to 1 for x, y, and z.
f. Set the gain on the Perkin Elmer 5113 preamplifier to at least 5. Set the low pass filter cutoff as desired (typically 100 or 300Hz).
g. Run the *coarseapproach.m* program.
h. After coarseapproach.m has completed running, it may be necessary to step another degree or two closer to the sample. Ideally the touchdown occurs with between –2V and –5V output from the z channel of the DAQ board. The touchdown should always occur at a voltage below 0 such that in the event of a power failure the cantilever tip does not crash into the sample.

A.5 Constant Frequency Scanning

a. Note the touchdown voltage from the *coarseapp.m* program, or measure it using *dFzcurve.m*.
b. Set the Output Gain to 1 in the easyPLL software.
c. Set the voltage on the sample. It is typically 0.5-2V.
d. Increase the frequency offset so that the z-feedback PI controller outputs +10V.

e. Turn down the z voltage pot. Turn the z voltage pot up again.
f. Adjust the gains and cutoff frequencies on the Perkin Elmer 5113 preamp and the PI controller as needed. Typical values for the gains are 100 on the 5113, a P-gain of 10, and an I-gain of 100.
g. Approach the sample surface by reducing the frequency offset until the PI controller output is close to the touchdown voltage (according to the desired scan height).
h. Readjust the gains as needed.
i. Perform a constant frequency scan using *MFMcfscan.m*.

A.6 Constant Height Scanning

a. Following Section A.5, decrease the frequency shift until the cantilever is very close to the sample, such that topography dominates the signal. Run *MFMcfscan.m* as needed to optimize the gains and scan height. Determine the coefficients of the sample plane using *getcoeffs.m*. Save the coefficients to a file. This step only needs to done before the first constant height scan.
b. Set the constant term in the plane coefficients (*coeffs(5,:)*) by finding the touchdown voltage using *dFzcurve.m*.
c. Perform a constant height scan using *MFMdfscan.m*.

A.7 Ending an Experiment

A.7.1 Warming Up

a. Turn the fine approach screw +720º using the stepper motor.
b. Turn off all of the high voltages, and “short” the piezos.
c. Blow out any remaining cryogens from the dewar. If there is a minimal amount left and a fast turnaround is not required, the cryogens can boil off and the microscope can be allowed to warm up in the dewar. Proceed to Section A.7.2. If a fast turnaround is desired, continue with the steps in this section.
d. Allow the microscope temperature to rise to at least 80K.
e. Close the main valve and shut down the pumps. Vent the pump lines with nitrogen gas.

f. Flow a large amount of nitrogen gas through the dewar to prevent water vapor from collecting and condensing/freezing in the dewar.
g. Use the hoist to rapidly raise the microscope out of the dewar. Immediately cover the mouth of the dewar with the designated aluminum plate.
h. Set the microscope on the working shelf. Allow it to warm up while keeping it under vacuum to limit the rate of temperature rise.
i. Once the temperature has reached 250K or greater, vent the microscope with nitrogen gas.

A.7.2 Disassembling the Setup

Generally, the microscope should not be opened to air until needed (the cantilever or sample is needed for further examination, repairs are needed, or the next experiment is beginning). This is to prevent water from collecting on the walls of the vacuum space. The future pumpdown time will be dramatically reduced if nitrogen gas is constantly flowed through the microscope once it has been opened.

a. Remove the 4 gold-plated semi-cones from the bottom microscope vacuum flange.
b. Remove the vacuum can. There are four threaded holes which may be used with screws to push the flanges apart.
c. Loosen the 2-56 set screws stabilizing the 8-32 kinematic mount screws.
d. Unscrew the ¼-80 fine pitch screw and the 8-32 screws to move the sample away from the cantilever.
e. Screw in the 8-80 screw to push the cantilever away from the fiber. Loosen all four 0-80 screws at the back of the bender. Remove the fiber rod carefully, and insert it in the temporary holding slot. Hold it in place by tightening the 0-80 screw.
f. Disconnect the heat sink braids and the electrical wires.
g. Remove the alignment assembly and place it in a clean container for temporary storage.
h. Remove the sample and store it in a clean container.

This page intentionally left blank.

References

Albrecht, T., P. Grütter, et al. (1991). "Frequency modulation detection using high-Q cantilevers for enhanced force microscope sensitivity." Journal of Applied Physics **69**(2): 668-73.

Albrecht, T. R., P. Grütter, et al. (1992). "Low-temperature force microscope with all-fiber interferometer." Ultramicroscopy **42/44**: 1638-46.

Arie, T. A., H. A. Nishijima, et al. (2000). "Carbon-nanotube probe equipped magnetic force microscope." Journal of Vacuum Science & Technology B (Microelectronics and Nanometer Structures) **18**(1): 104-6.

Baur, C., A. Bugacov, et al. (1998). "Nanoparticle manipulation by mechanical pushing: underlying phenomena and real-time monitoring." Nanotechnology **9**(4): 360-4.

Behler, S., S. H. Pan, et al. (1994). "Vortex pinning in ion-irradiated $NbSe_2$ studied by scanning tunneling microscopy." Physical Review Letters **72**(11): 1750-3.

Besocke, K. (1987). "An easily operable scanning tunneling microscope." Surface Science **181**(1-2): 145-53.

Bevington, P. R. and D. K. Robinson (1992). Data Reduction and Error Analysis for the Physical Sciences. Boston, MA, WCB/McGraw-Hill.

Binnig, G., C. F. Quate, et al. (1986). "Atomic force microscope." Physical Review Letters **56**(9): 930-3.

Chiaverini, J., K. Yasumura, et al. (2001). "Microcantilever studies of angular field dependence of vortex dynamics in $Bi_2Sr_2CaCu_2O_{8-x}$." Physical Review B **64**: 014516-5.

Cullity, B. D. (1972). Introduction to Magnetic Materials. Reading, MA, Addison-Wesley Pub. Co.

Deng, Z., E. Yenilmez, et al. Unpublished work.

Diaz, A., L. Mechin, et al. (1998). "Evidence for vortex pinning by dislocations in $YBa_2Cu_3O_{7-\delta}$ low-angle grain boundaries." Physical Review Letters **80**(17): 3855-8.

Dinega, D. (2001). Synthesis and characterization of cobalt nanocrystals. Department of Chemistry. Cambridge, Massachusetts Institute of Technology.

Dürig, U., H. R. Steinauer, et al. (1997). "Dynamic force microscopy by means of the phase-controlled oscillator method." Journal of Applied Physics **82**(8): 3641-51.

Eigler, D. M. and E. K. Schweizer (1990). "Positioning single atoms with a scanning tunnelling microscope." Nature **344**(6266): 524-26.

Elmers, H. J. and U. Gradmann (1990). "Magnetic Anisotropies in Fe(110) Films on W(110)." Applied Physics A **51**: 255-63.

Folks, L., M. E. Best, et al. (2000). "Perforated tips for high-resolution in-plane magnetic force microscopy." Applied Physics Letters **76**(7): 909-11.

Gradmann, U., K. Werner, et al. (1976). "High Sensitivity Torsion Magnetometers for Oligatomic Films." Applied Physics **10**: 219-225.

Grütter, P., H. J. Mamin, et al. (1995). Magnetic Force Microscopy (MFM). Scanning Tunneling Microscopy II. H.-J. G. R. Wiesendanger. Berlin, Springer.

Guikema, J. W. (2004). Scanning Hall Probe Microscopy of Magnetic Vortices in Very Underdoped Yttrium-Barium-Copper-Oxide. Department of Physics. Stanford, CA, Stanford University.

Harris, J. G. E. (2000). High Sensitivity Magnetization Studies of Semiconductor Heterostructures. Department of Physics. Santa Barbara, University of California at Santa Barbara.

Harris, J. G. E., D. D. Awschalom, et al. (1999). "Integrated micromechanical cantilever magnetometry of $Ga_{1-x}Mn_xAs$." Applied Physics Letters **75**(8): 1140-2.

Harris, J. G. E., D. D. Awschalom, et al. (2000). "Magnetization and dissipation measurements in the quantum Hall regime using an integrated micromechanical magnetometer." Journal of Applied Physics **87**(9 pt.1): 5102-4.

Harris, J. G. E., R. Knobel, et al. (2001). "Magnetization measurements of magnetic two-dimensional electron gases." Physical Review Letters **86**(20): 4644-7.

Hug, H., B. Stiefel, et al. (1998). "Quantitative magnetic force microscopy on perpendicularly magnetized samples." Journal of Applied Physics **83**(11): 5609-20.

Hug, H., B. Stiefel, et al. (1999). "A low temperature ultrahigh vacuum scanning force microscope." Review of Scientific Instruments **70**(9): 3625-40.

Hug, H. J., A. Moser, et al. (1993). "Low temperature magnetic force microscopy." Review of Scientific Instruments **64**(10): 2920-5.

Jooss, C., R. Warthmann, et al. (1999). "Vortex pinning due to strong quasiparticle scattering at antiphase boundaries in $YBa_2Cu_3O_{7-\delta}$." Physical Review Letters **82**(3): 632-5.

Lairson, B. M., S. K. Streiffer, et al. (1990). "Vortex pinning and twin boundaries in $YBa_2Cu_2O_{7-\delta}$ thin films." Physical Review B **42**(16, pt. A): 10067-74.

Liu, Y. (1997). Magnetic Dissipation Microscopy. Department of Physics. Montreal, McGill University.

Lohau, J., S. Kirsch, et al. (1999). "Quantitative determination of effective dipole and monopole moments of magnetic force microscopy tips." Journal of Applied Physics **86**(6): 3410-7.

Loomba, D., V. Halyo, et al. (2000). "A new method for searching for free fractional charge particles in bulk matter." Review of Scientific Instruments **71**(9): 3409-14.

Lu, Q., K. Mochizuki, et al. (2002). "Localized measurement of penetration depth for a high T_c superconductor single crystal using a magnetic force microscope." Physica C **371**(2): 146-50.

Lupien, C., B. Ellman, et al. (1999). "Piezoresistive torque magnetometry below 1 K." Applied Physics Letters **74**(3): 451-3.

Mamin, H. and D. Rugar (2001). "Sub-attonewton force detection at millikelvin temperatures." Applied Physics Letters **79**(20): 3358-60.

Martin, J. I., M. Velez, et al. (1999). "Artificially induced reconfiguration of the vortex lattice by arrays of magnetic dots." Physical Review Letters **83**(5): 1022-5.

Martin, Y. and H. Wickramasinghe (1987). "Magnetic imaging by 'force microscopy' with 1000 Å resolution." Applied Physics Letters **50**(20): 1455-7.

Martin, Y., C. C. Williams, et al. (1987). "Atomic force microscope-force mapping and profiling on a sub 100-Å scale." Journal of Applied Physics **61**(10): 4723-9.

McConnell, A. W., R. A. Hughes, et al. (1994). "Evaluation of $LaSrGaO_4$ as a substrate for $YBa_2Cu_3O_{7-\delta}$." Physica C **225**(1-2): 7-12.

Moser, A., H. Hug, et al. (1995). "Observation of single vortices condensed into a vortex-glass phase by magnetic force microscopy." Physical Review Letters **74**(10): 1847-50.

Moser, A., H. Hug, et al. (1998). "Low temperature magnetic force microscopy on $YBa_2Cu_3O_{7-\delta}$ thin films." Journal of Magnetism and Magnetic Materials **190**(1/2): 114-23.

Mulhern, P., T. Hubbard, et al. (1991). "A scanning force microscope with a fiber-optic-interferometer displacement sensor." Review of Scientific Instruments **62**(5): 1280-4.

Olson Reichhardt, C. J. and M. B. Hastings (2004). "Do Vortices Entangle?" Physical Review Letters **92**: 157002-4.

Pan, S. H., E. W. Hudson, et al. (1999). "^{3}He refrigerator based very low temperature scanning tunneling microscope." Review of Scientific Instruments **70**(2): 1459-63.

Paulius, L. M., J. A. Fendrich, et al. (1997). "Effects of 1-GeV uranium ion irradiation on vortex pinning in single crystals of the high-temperature superconductor $YBa_2Cu_3O_{7-\delta}$." Physical Review B **56**(2): 913-24.

Pearl, J. (1966). "Structure of superconductive vortices near a metal-air interface." Journal of Applied Physics **37**: 4139-41.

Philips, G. N., M. Siekman, et al. (2002). "High resolution magnetic force microscopy using focused ion beam modified tips." Applied Physics Letters **81**(5): 865-7.

Pi, U., D. Kim, et al. (2003). "Vortex dynamics in $Bi_2Sr_2CaCu_2O_2$ single crystal with low density columnar defects studied by magnetic force microscope." Journal of Low Temperature Physics **131**(5/6): 993-1002.

Roseman, M. and P. Grütter (2000). "Cryogenic magnetic force microscope." Review of Scientific Instruments **71**(10): 3782-7.

Roseman, M. and P. Grütter (2001). "Estimating the magnetic penetration depth using constant-height magnetic force microscopy images of vortices." New Journal of Physics **3**: 241-48.

Roseman, M. and P. Grütter (2002). "Magnetic imaging and dissipation force microscopy of vortices on superconducting Nb films." Applied Surface Science **188**(3/4): 416-20.

Roseman, M., P. Grütter, et al. (2001). "Flux lattice imaging of a patterned niobium thin film." Journal of Applied Physics **89**(11): 6787-2.

Rugar, D., H. Mamin, et al. (1989). "Improved fiber-optic interferometer for atomic force microscopy." Applied Physics Letters **55**(25): 2588-90.

Rugar, D., B. C. Stipe, et al. (2001). "Adventures in attonewton force detection." Applied Physics A: Materials Science & Processing **72**(7): S3-S10.

Ruhrig, M., S. Porthun, et al. (1996). "Electron beam fabrication and characterization of high-resolution magnetic force microscopy tips." Journal of Applied Physics **79**(6): 2913-9.

Sarid, D. (1991). Scanning Force Microscopy. New York, Oxford University Press.

Skidmore, G. D. and E. D. Dahlberg (1997). "Improved spatial resolution in magnetic force microscopy." Applied Physics Letters **71**(22): 3293-5.

Stipe, B., H. Mamin, et al. (2001). "Magnetic dissipation and fluctuations in individual nanomagnets measured by ultrasensitive cantilever magnetometry." Physical Review Letters **86**(13): 2874-7.

Stipe, B. C., H. J. Mamin, et al. (2001). "Magnetic Dissipation and Fluctutations in Individual Nanomagnets Measured by Ultrasensitive Cantilever Magnetometry." Physical Review Letters **86**: 2874.

Stowe, T. (2000). Extending the Lower Limits of Force Detection Using Micromachined Silicon Cantilevers. Department of Applied Physics. Stanford, CA, Stanford University.

Stowe, T., K. Yasumura, et al. (1997). "Attonewton force detection using ultrathin silicon cantilevers." Applied Physics Letters **71**(2): 288-90.

Stowe, T. D., T. W. Kenny, et al. (1999). "Silicon dopant imaging by dissipation force microscopy." Applied Physics Letters **75**(18): 2785-7.

Sun, S. and C. B. Murray (1999). "Synthesis of monodisperse cobalt nanocrystals and their assembly into magnetic superlattices." Journal of Applied Physics **85**(8): 4325-30.

Sun, S., C. B. Murray, et al. (2000). "Monodisperse FePt Nanoparticles and Ferromagnetic FePt Nanocrystal Superlattices." Science **287**: 1989-92.

Todorovic, M. and S. Schultz (1998). "Miniature high-sensitivity quartz tuning fork alternating gradient magnetometry." Applied Physics Letters **73**(24): 3595-7.

Topinka, M. (2002). Imaging Coherent Electron Wave Flow Through 2-D Electron Gas Nanostructures. Department of Physics. Cambridge, MA, Harvard University.

Tortonese, M. (1993). "Atomic resolution with an atomic force microscope using piezoresistive detection." Applied Physics Letters **62**(8): 834-6.

van den Bos, A., I. Heskamp, et al. (2002). "The CantiClever: a dedicated probe for magnetic force microscopy." IEEE Transactions on Magnetics **38**(5, pt.1): 2441-3.

van Schendel, P., H. Hug, et al. (2000). "A method for the calibration of magnetic force microscopy tips." Journal of Applied Physics **88**(1): 435-45.

Volodin, A., K. Temst, et al. (2002). "Magnetic force microscopy of vortex pinning at grain boundaries in superconducting thin films." Physica C **369**(1/4): 165-70.

Volodin, A., K. Temst, et al. (2000). "Magnetic force microscopy on superconducting $NbSe_2$ and Nb surfaces." Physica B **284/288**: 815-16.

Volodin, A., K. Temst, et al. (1998). "Observation of the Abrikosov vortex lattice in $NbSe_2$ with magnetic force microscopy." Applied Physics Letters **73**(8): 1134-6.

Volodin, A., K. Temst, et al. (2000). "Low temperature magnetic force microscopy with enhanced sensitivity based on piezoresistive detection." Review of Scientific Instruments **71**(12): 4468-73.

Volodin, A., K. Temst, et al. (2002). "Magnetic-force microscopy of vortices in thin niobium films: correlation between the vortex distribution and the thickness-dependent film morphology." Europhysics Letters **58**(4): 582-8.

Yasumura, K. (2000). Energy Dissipation Mechanisms in Microcantilever Oscillators with Applications to the Detection of Small Forces. Department of Applied Physics. Stanford, CA, Stanford University.

Yuan, C., E. Batalla, et al. (1994). "Low temperature magnetic force microscope utilizing a piezoresistive cantilever." Applied Physics Letters **65**(10): 1308-10.

Yuan, C. W., Z. Zheng, et al. (1996). "Vortex images in thin films of $YBa_2Cu_3O_{7-x}$ and $Bi_2Sr_2Ca_1Cu_2O_{8+x}$ obtained by low-temperature magnetic force microscopy." Journal of Vacuum Science & Technology B (Microelectronics and Nanometer Structures) **14**(2): 1210-13.

Zijlstra, H. (1961). "Device for the Rapid Measurement of Magnetic Anisotropy at Elevated Temperatures." Review of Scientific Instruments **32**(6): 634-8.